University of Alberta

Nanostructured Materials for Organic Photovoltaic Devices

by

Jaron Glenn van Dijken

A thesis submitted to the Faculty of Graduate Studies and Research
in partial fulfillment of the requirements for the degree of

Doctor of Philosophy

in

Microsystems and Nanodevices

Department of Electrical and Computer Engineering

Fall 2012

Edmonton, Alberta

To my family

ABSTRACT

This thesis outlines several new approaches to fabricating improved organic solar cell (OSC) designs. Glancing angle deposition (GLAD) was used to grow thin films of metal phthalocyanine (MPc) materials with columnar morphologies suitable for use in OSCs. Advanced substrate motion techniques were used to constrain column broadening during growth, in order to approach diameters comparable to the short exciton diffusion lengths in these materials. Substrate patterning was used to predefine growth sites for these columnar films, and thereby regulate column spacing and improve film uniformity. Increased column densities and decreased column diameters were achieved as a result.

Integration of columnar films into OSCs was challenged by the sensitivity of MPc materials to the solvents used to cast the adjacent layer. Significant recrystallization of the films occurred when directly contacted by these solvents. Varying degrees of material mixing between layers were observed as a result of the solvents when casting the adjacent layer. This result provides an alternative approach to building a mixed active layer structure, which has so far only been possible via codeposition of vapors or polymer blending. Material mixing was shown to improve device performance, which led to photoconversion efficiencies of up to 3.0% when

used in combination with a GLAD-structured MPc layer. This result stands among the best results achieved in the literature for these devices. Optimized devices were enabled by a careful evaluation of the degradation behavior and thickness effects of the various device layers.

Argon plasma etching was used to structure planar MPc films and commercial indium tin oxide (ITO). Nanopillar features emerged in both cases, which are very attractive from an OSC perspective. The surface composition of these films was altered by the etching process, resulting in damaged film properties. The damage to MPc films was irreversible, preventing their ideal morphologies from improving OSC performance. For ITO, however, optical and electrical properties were recovered using a two-stage annealing process, leaving the films fully functional for use in a variety of optoelectronic devices.

ACKNOWLEDGEMENTS

Over the course of my doctoral program, I have received invaluable input from many individuals to whom I owe my sincerest gratitude. I would like to thank my supervisor, Dr. Michael Brett, for providing an outstanding research environment that both demands and enables excellence. Your energy and enthusiasm inspire us all. I would like to thank my many colleagues for providing direction and assistance to various aspects of my work: Dr. Michael Fleischauer, Dr. Michael Taschuk, Dr. Jeremy Sit, Dr. Jillian Buriak, Nathanael Wu, Brian Worfolk, Tate Hauger, Al Lalany, Mark Summers, Josh LaForge, Ryan Tucker, Jon Kwan, and Steven Jim. In particular, I would like to thank my partner in commercializable crime, Michael Thomas, for your inspiring companionship and hard after-hours work on our many business aspirations. I await any future ventures with great anticipation.

I am very grateful to the following funding agencies for their gracious financial support during my graduate program: the Natural Sciences and Engineering Research Council of Canada (NSERC), Alberta Innovates – Technology Futures (AITF), the International Society for Optics and Photonics (SPIE), the Informatics Circle of Research Excellence (iCORE), the Golden Key International Honour Society, The Association of Professional Engineers and Geoscientists of Alberta (APEGA), the Alberta Heritage Scholarship Fund, and the University of Alberta. I hope to be able to give back to the next generation even more than what I have received.

I am fortunate to have so many great friends and family members; I thank you all for your support and encouragement over the years. Your sincere interest in my work is greatly appreciated. To my parents, Glenn and Barb, thank you for teaching me to avoid complacency and instilling in me so many timeless virtues. Your selflessness, integrity, ambition, perseverance, and pursuit of truth deserve the utmost admiration. I hope to continue to learn by your example. And finally, to my wife Diana, you amaze me every day with your kind and tender heart, your pure and genuine joy, your unfailing optimism, and your unconditional love. Thank you for always bringing out the best in me. Time flies by when we're together and I look forward to being with you every step of the way.

CONTENTS

LIST OF TABLES

LIST OF FIGURES

LIST OF SYMBOLS AND ABBREVIATIONS

α	Deposition angle
A	Electron acceptor semiconductor
AM 1.5 G	Air mass 1.5 global solar spectrum
Ag	Silver
Al	Aluminum
BCP	Bathocuproine (or block copolymer, depending on context)
BHJ	Bulk heterojunction
CB	Chlorobenzene
CuPc	Copper phthalocyanine
D	Electron donor semiconductor
D/A	The interface between the donor and acceptor semiconductors
DCB	Dichlorobenzene
EBL	Electron blocking layer
ETL	Electron transport layer
ϕ	Substrate rotation angle
Φ	Work function
FF	Fill factor
FTIR	Fourier transform infrared spectroscopy
γ	ϕ-sweep offset angle

GLAD	Glancing angle deposition
HOMO	Highest occupied molecular orbital
HTL	Hole transport layer
In	Indium
ITO	Indium tin oxide
J_{sc}	Short circuit current density
L_D	Exciton diffusion length
LUMO	Lowest unoccupied molecular orbital
μ_n	Electron mobility
μ_P	Hole mobility
MHJ	Mixed heterojunction
MPc	Metal phthalocyanine
η_P (or η)	Photoconversion efficiency
η_{IQE} (IQE)	Internal quantum efficiency
η_{EQE} (EQE)	External quantum efficiency
η_A	Efficiency of light absorption
η_{ED}	Efficiency of exciton diffusion to the D/A interface
η_{CT}	Efficiency of charge transfer (dissociation) at the D/A interface
η_{CC}	Efficiency of charge collection after dissociation
OAD	Oblique angle deposition

OLED	Organic light emitting diode
OPV	Organic photovoltaic
OSC	Organic solar cell
OTFT	Organic thin film transistor
P_{inc}	Incident solar power
PCBM	[6,6]-phenyl-C_{61} butyric acid methyl ester
PEDOT:PSS	Poly(3,4-ethylenedioxythiophene) poly(styrenesulfonate)
PTCBI	Perylenetetracarboxylic bis-benzimidazole
PV	Photovoltaic
QE	Quantum efficiency
R_s	Series resistance
RIE	Reactive ion etching
SBD	Serial bideposition
SEM	Scanning electron microscopy
SIMS	Secondary ion mass spectrometry
Sn	Tin
SP	Slanted post
UHV	Ultra-high vacuum
UPS	Ultraviolet photoelectron spectroscopy
UV/Vis	Ultraviolet/visible wavelength region spectroscopy

V_{bi}	Built-in voltage
V_{oc}	Open circuit voltage
VP	Vertical post
XPS	X-ray photoelectron spectroscopy
XRD	X-ray diffraction
ZnPc	Zinc phthalocyanine

1. INTRODUCTION

> "I'd put my money on the sun and solar energy. What a source of power! I hope we don't have to wait until oil and coal run out before we tackle that."
>
> - Thomas Edison, March 1931 [1]

1.1. Motivation

In an ever-growing energy economy, whose ubiquitous dependence on fossil fuels gives rise to various environmental concerns, demands for renewable energy are stronger than ever. Solar power is expected to play an increasingly important role in meeting these energy needs, and various approaches to harvesting solar energy are being pursued. At the forefront of these efforts are photovoltaic (PV) devices, which convert solar radiation directly into electrical power via the photovoltaic effect.

Crystalline silicon PV products dominate the solar market with their highly competitive cost per watt and photoconversion efficiencies of nearly 20%. The retail price of these panels has decreased dramatically over the past two decades due to refinements in processing, improvements in photoconversion efficiency, and economies of scale [2,3]. Consequently, the global PV market has grown during this time by an annual rate of over 30% [2–7]. However, the high temperature processing and material purity requirements for conventional PV technology render them almost irreducibly expensive. Large scale power generation from PV remains uncompetitive with fossil fuels in most areas of the world [8]. Elaborate designs for concentrator systems and multi-junction PV devices have pushed efficiency records beyond 40%, but at a much higher cost [9,10]. Thin film PV technologies take an alternative approach of sacrificing module performance for reductions in cost and energy inputs by using amorphous semiconductor layers [11]. The leading thin film company, First Solar, is currently the largest

and most profitable PV module manufacturer in the world [12]. They claim a 30% cost advantage over crystalline silicon PV manufacturers, as well as the best energy payback time of any manufacturer in the industry [13]. From this trend, it appears that sacrificing panel efficiency to accomplish lower per-watt costs is acceptable, which suggests that area is not a major constraint for most PV installations. This warrants further development of photovoltaic devices based on inexpensive and abundant materials that can be processed at high throughput using low-cost mass manufacturing methods [8].

Organic photovoltaic (OPV) devices utilize small molecule or polymer materials to absorb light and generate electrical power. Emerging nearly three decades ago [14], OPV devices have made great strides in recent years to become a promising new platform for achieving ultra-low-cost solar energy conversion [3,4,10,15–22]. The usage of inexpensive materials and substrates, combined with the ability to manufacture at great speed using roll-to-roll coating techniques, provides great advantages over conventional technology [23]. Furthermore, the possibilities for new materials with improved and tunable properties are immense. Semitransparency and color tunability are unique advantages of OPV technology, which could provide aesthetic appeal and enable application-specific panel designs. From a consumer perspective, the lightweight, flexible, and portable nature of these products would make them even more attractive [24–28]. Integration into portable electronic devices, such as the back of mobile phones and tablet computers, could liberate users from grid-tied battery charging [7]. The potential for OPV technology is well-recognized, as indicated by the rapid rise in recent publications [4,29] and commercialization efforts [18].

Commercial success of OPV technology has been limited by poor module efficiency and lifetime. A commonly cited efficiency milestone for commercial relevance of OPV technology is 10% [30]. This target has been seriously approached only within the last two years, and only on very small area cells. As with any PV technology, module performance is limited by the individual cells with the lowest current. The best OPV module efficiencies are 4.2% [31], but values of 2 ~ 3% are more common [32,33]. Module lifetimes are

another important issue plaguing the advancement of OPV technology. Performance often drops within hours of exposure to air [34–36], and even encapsulated modules typically last little more than a year at best [29,37]. One recent study reports projected lifetimes of up to 7 years for a new polymer device [38], which may be sufficient for initial niche applications, but lifetimes of over 20 years will be necessary to compete with other PV products. Encapsulated small molecule OPV devices exhibit the strongest lifetimes [39–41], with some projections of beyond 30 years [42]. Heliatek, a leading OPV company, claims the highest device lifetimes and efficiencies in the industry [43,44]. Remarkably, this is accomplished without precise control over the nanoscale film morphology of materials in the active layer. Improvements in this area were recently stated as a critical means of further increasing their device performance [45], which could suddenly result in a product capable of competing with other PV technologies.

The rapid progress seen in the OPV field in recent years is compelling. Still, it is well recognized that any significant market impact relies heavily on improved photoconversion performance. This thesis describes several nanostructuring techniques that may be used towards these ends.

1.2. Organic Photovoltaic Devices

1.2.1. History

The OPV field falls under the broader umbrella of organic electronics, a field which also includes organic light-emitting diodes (OLEDs) and organic thin film transistors (OTFTs). It began with the discovery in 1977 by Alan Heeger's group that the conductivity of polyacetylene could be increased by 10 orders of magnitude by doping with iodine [46]. This meant that the properties of conjugated polymers could be tailored to act as electrical conductors and semiconductors, and the discovery was awarded the Nobel Prize in Chemistry in the year 2000. It took a while, however, before this discovery translated into the first organic optoelectronic devices.

The first organic solar cell was devised in 1986 by Ching Tang at Eastman Kodak [14]. His design was a bilayer of 2 small molecule organic semiconductors, which achieved a photoconversion efficiency of 1%. A year later, he used a similar device layout with different materials to make the first OLED [47]. Polymeric devices came a bit later, with the first polymer OLED being demonstrated in 1990 [48] and the first demonstration of photovoltaic charge generation from polymer semiconductors occurring in 1992 [49], again by Heeger's group. Following further improvements in the technology, Heeger co-founded the first commercial OPV venture in 2001, Konarka. By 2005, efficiencies of 5% were within reach [50], but it wasn't until 2009 that OPV products were available. Until about that time, Konarka remained the only significant OPV company, though the intellectual property was broadly distributed [18]. Meanwhile, progress on OLED technology has outpaced OPV, with commercialization well underway. The great success of the OLED industry remains a source of optimism for the OPV community.

Recently, OPV commercialization has become more competitive, with companies such as Mitsubishi, and BASF-sponsored Heliatek, making aggressive strides. Mitsubishi recently achieved the 10% efficiency target with a single junction device [10,51], while Konarka, Solarmer, and Heliatek have all exceeded 8% [22]. Heliatek currently holds the efficiency record for a tandem device, with 10.7% [43].

1.2.2. Energy conversion process

Organic conductors and semiconductors operate on fundamentally different physics than their inorganic counterparts, and therefore OPV devices face several new limitations and challenges. Inorganic PV devices are able to immediately generate free charge carriers upon light absorption, which can be gathered by the built-in electric field in the p-n junction and contribute to current. However, OPV devices are excitonic, which means that incoming light generates a tightly bound electron-hole pair, referred to as an exciton [52]. Exciton binding energies in organic semiconductors are typically 0.5 ~ 1.0 eV [53–55]. In order for this exciton to generate free charge

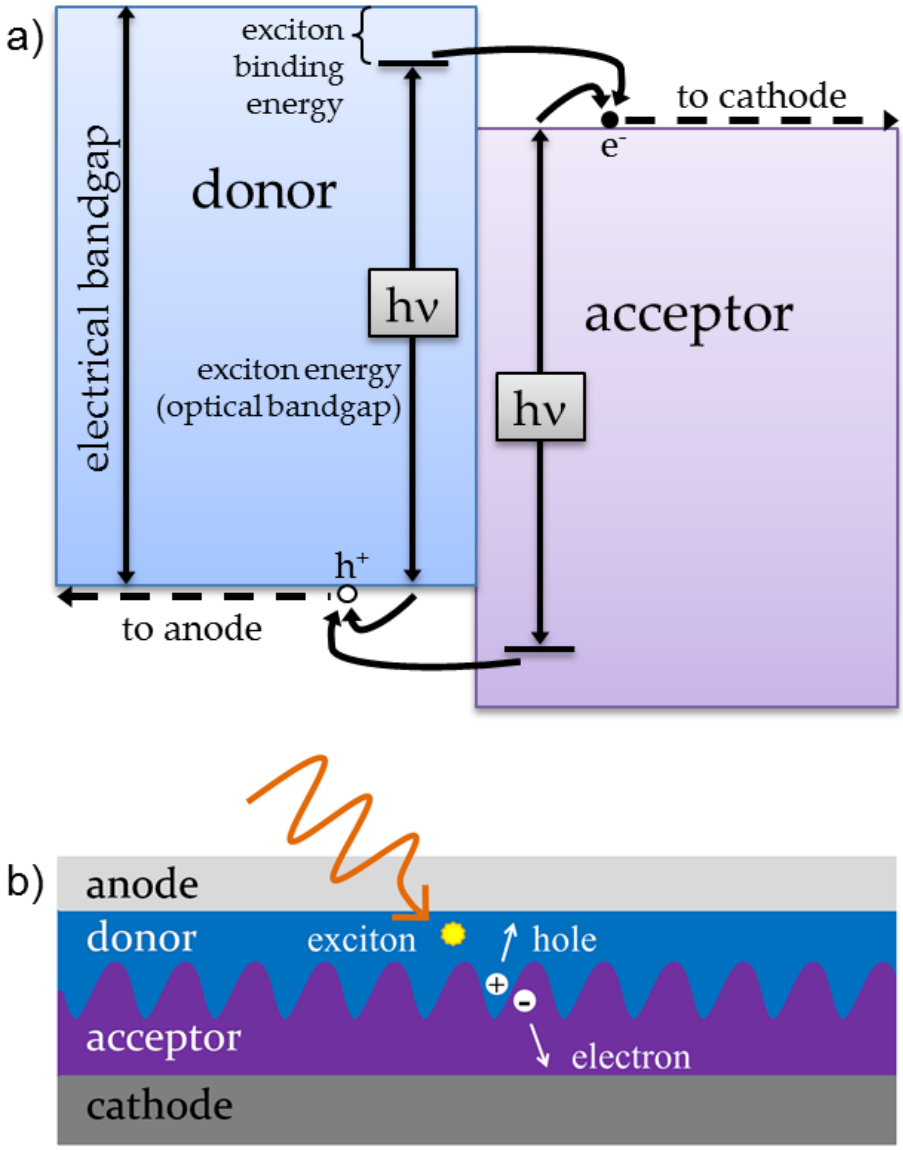

Figure 1.1 Charge generation process in an excitonic solar cell illustrated by (a) energy band diagram, and (b) cross-sectional device layout. Panel (b) is adapted with permission from [56], © (2008) IEEE.

carriers that contribute to current, it must first dissociate into a free electron and hole. This is accomplished by encountering an interface with another material, if the energy difference between the LUMO bands is greater than the exciton binding energy (see Figure 1.1a). Once dissociation is complete, the electron is swept through the "electron acceptor" material (A) for

collection at the cathode, while the hole is swept through the "electron donor" material (D), for collection at the anode (see Figure 1.1b). Thus, in its most basic form, an OPV device consists of an active layer (containing the organic semiconductors and the D/A interface) sandwiched between two electrodes, one of which must be transparent to allow light into the cell. Because this process relies so heavily on successful exciton dissociation, much of the engineering in OPV devices is focused on the D/A interface.

If the exciton does not encounter the appropriate interface, it will continue to diffuse through the donor material and recombine in a thermally dissipative process. What makes OPV device design so challenging is that the exciton diffusion length, L_D, is typically very short in organic materials, on the order of 5 ~ 20 nm [57]. Thus, the donor layer must be extremely thin to promote strong exciton dissociation efficiency, which limits absorption. This is compounded by the fact that most light absorbing organic semiconductors used in OPV devices have a rather narrow absorption spectrum. Furthermore, the low charge carrier mobilities in organic semiconductors make charge extraction difficult, which further constrains the absorber layer thickness. The following section discusses the limits to OPV device efficiency further.

1.2.3. Photoconversion efficiencies and limiting factors

The practical definition of a solar cell's photoconversion efficiency, η_P, is given by:

$$\eta_P = V_{oc} J_{sc} FF / P_{inc} \quad (1)$$

Here V_{oc} is the open circuit voltage, J_{sc} is the short circuit current density, FF is the fill factor, and P_{inc} is the incident solar power. Generally, device testing is done under AM 1.5 G simulated irradiation (P_{inc} = 100 mW/cm^2), and the device parameters mentioned in equation 1 can be calculated from the current-voltage curve of a cell under illumination (see Figure 1.2).

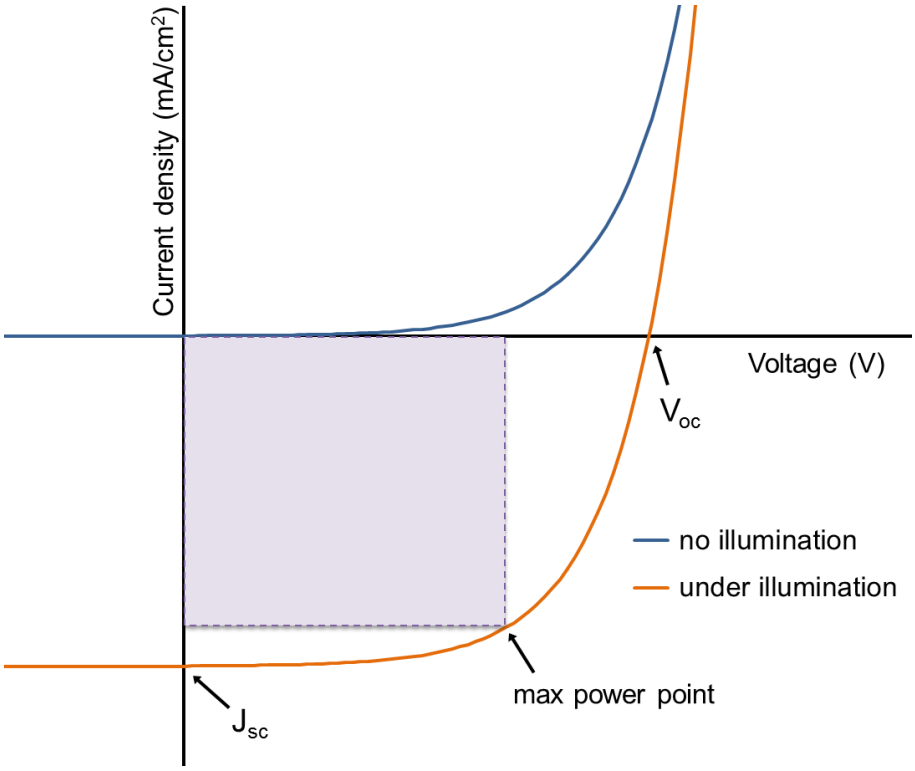

Figure 1.2 Current voltage behavior of a photovoltaic device.

Each step in the photoconversion process can be attributed with its own efficiency (denoted by η). Quantum efficiency (QE) is defined as the number of electrons generated per number of incident photons. Ideally QE = 1 = 100%, where each photon generates an electron for current flow. The internal quantum efficiency, η_{IQE}, is the product of the efficiencies of four separate steps in the charge generation process [57]:

$$\eta_{IQE} = \eta_A \, \eta_{ED} \, \eta_{CT} \, \eta_{CC}, \tag{2}$$

where

η_A = efficiency of light absorption within the active layer of the cell,
η_{ED} = efficiency of exciton diffusion to the active layer interface,
η_{CT} = efficiency of charge transfer (exciton dissociation efficiency), and
η_{CC} = efficiency of charge collection once the exciton is dissociated.

The external quantum efficiency, η_{EQE}, is then defined by taking into account reflective losses that limit the energy available for absorption in the active layer:

$$\eta_{EQE} = (1 - R)\ \eta_{IQE}, \quad (3)$$

where R = the reflectivity of the substrate/air interface.

In most cases, charge transfer and collection proceed with nearly 100% efficiency in molecular OPV cells, meaning that the light absorption and exciton diffusion processes account for the majority of losses. Therefore, the internal quantum efficiency is primarily determined by the product of $\eta_A\eta_{ED}$. This efficiency product presents the previously-mentioned trade-off between light absorption and exciton diffusion. For an organic layer of thickness d, the absorption efficiency is determined by:

$$\eta_A = (1 - e^{-\alpha d}), \quad (4)$$

where α = absorption coefficient,
and the exciton diffusion efficiency is:

$$\eta_{ED} = e^{-d/L_D}, \quad (5)$$

where L_D = exciton diffusion length.

For almost all absorber materials used in OPV cells, $L_D << 1/\alpha$ (L_D ~ 5 nm, $1/\alpha$ ~ 50 nm [58]). This leads to the "exciton diffusion bottleneck" illustrated in Figure 1.3, where an increasing absorber layer thickness lowers the efficiency product by reducing the percentage of excitons that reach the D/A interface. The challenge, then, is to capture as much incoming light as possible while ensuring that the majority of excitons are created within acceptable range of the D/A interface. New materials with improved absorption and exciton lifetime properties, as well as innovation in structuring materials at the nanoscale, are therefore the most important means of improving OPV device efficiency. This thesis focuses on optimizing the nanostructure of the donor layer. This approach is further discussed in section 1.3.4.

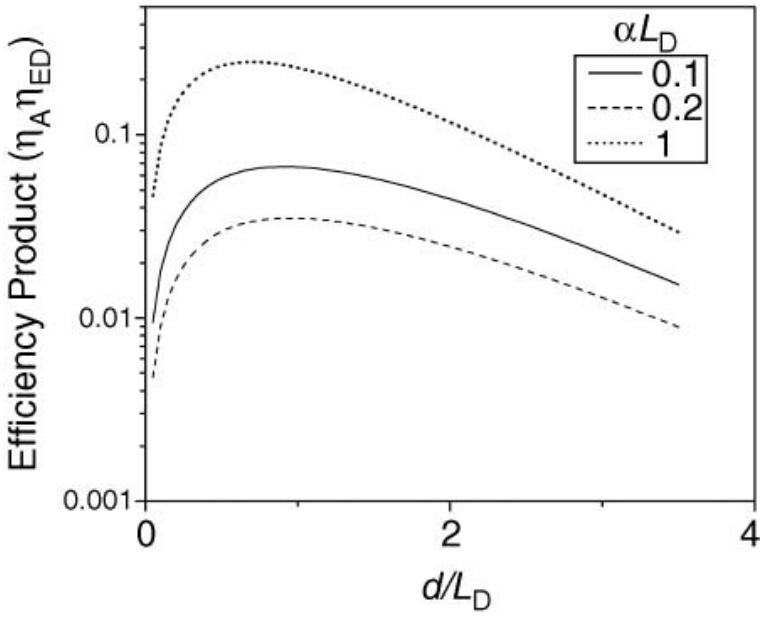

Figure 1.3 Exciton diffusion bottleneck: device efficiency drops as the thickness of the absorber layer grows beyond the exciton diffusion length. Reproduced with permission from [57].

1.2.4. Tandem device architectures

Many organic semiconductors used in OPV devices have a narrow absorption window. Their inability to collect an appreciable amount of the solar spectrum has led to the development of tandem architectures. In some cases, this is as simple as using two donor materials in one active layer [59,60]. However, in most cases an additional active layer is stacked on top of the device, which uses materials that capture the portion of the spectrum that is missed by the first one. Early demonstrations of this strategy yielded photoconversion efficiencies of 5.7% for small molecules [61] and 6.5% for polymers [15]. More recently, the records have climbed to 10.6% for polymers [20] and 10.7% for small molecules [43].

For tandem device concepts to be useful, the performance enhancement must outweigh the cost of additional processing. A recent study determined that the most market-relevant performance metrics for OPV modules are a combined 7% module efficiency and 5 year lifetime [62]. Applications with spatial constraints would benefit most from tandem cells, but otherwise the

lowest cost per watt module that achieves these metrics will be used. Whether single junction or tandem cells are best suited to these goals is yet to be seen.

1.3. Metal Phthalocyanine OPV Device Considerations

1.3.1. Active layer material properties

The materials used in the active layer of an OPV device hold the critical properties that determine device performance. The optical bandgap determines the absorption spectrum. The exciton diffusion length determines the upper bound on nanoscale film feature dimensions required for charge generation. The charge carrier mobilities determine the upper limit on the active layer thickness that will enable sufficient charge collection. And finally, the relative alignment of HOMO and LUMO levels determine the voltage, the losses associated with charge transfer, and the ease with which charges can be transferred to the electrodes. The properties of organic thin films are mostly determined by molecular structure and composition, but are also affected by the film deposition conditions and the properties of adjacent layers.

As mentioned previously, the active layer is composed of electron donating (D) and electron accepting (A) domains, which are analogous to the p-type and n-type materials that make up a conventional p-n junction. Unlike a conventional p-n junction, however, there is no depletion region in the active layer of an OPV device. Instead, a local field is present at the D/A interface, which is responsible for charge transfer [49,63–65]. Consequently, the photocurrent is voltage-dependent – another substantial difference from conventional p-n junctions – which is ultimately responsible for the low fill factors seen in OPV devices [64]. Following the analogy to conventional semiconductors, the valence and conductance energy bands in organic semiconductors are referred to as the highest occupied molecular orbital (HOMO) and lowest unoccupied molecular orbital (LUMO), respectively. Technically, both the D and A materials can contribute to absorption and exciton generation, and thereby contribute to photocurrent. In most cases, however, absorption and exciton creation occurs primarily in the donor layer.

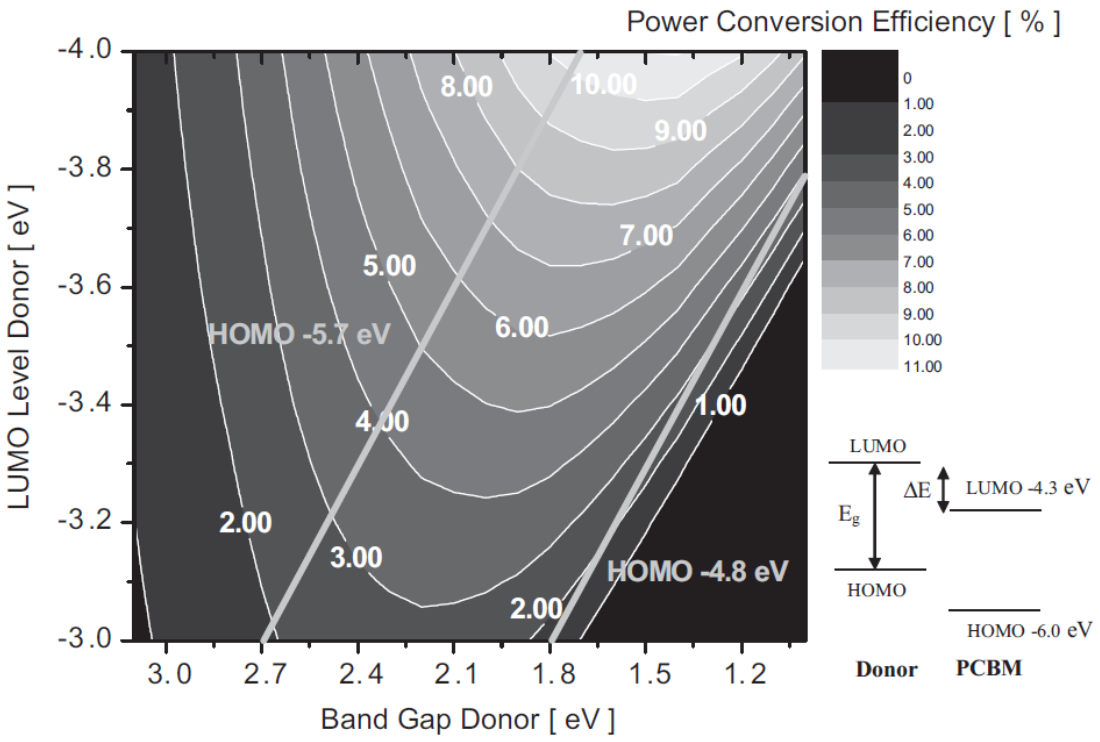

Figure 1.4 Dependence of the maximum power conversion efficiency of an OPV device on the LUMO level and band gap of the donor material. Reproduced with permission from [66], © 2006 WILEY-VCH Verlag GmbH & Co. KGaA, Weinheim.

Much work has been done on identifying the ideal properties of donor materials [66–68]. An optimal bandgap is necessary for maximum absorption, but must be achieved with energy bands that coincide appropriately with those of the acceptor material in order to enable exciton dissociation. In the vast majority of cases, the acceptor is a fullerene molecule, such as C_{60}, C_{70}, or their solubilized counterparts, $PC_{61}BM$ and $PC_{71}BM$. Thus, the analysis for ideal donor properties usually assumes a PCBM acceptor, with a HOMO of 6.0 eV and a LUMO of 4.3 eV. A local electric field of at least 10^6 V/cm is needed at the D/A interface to accomplish exciton dissociation, which requires that the LUMO of the donor be at least 0.3 eV higher than that of the acceptor [63–65]. Exceeding the minimum offset results in losses, so the optimal LUMO of the donor is relatively fixed, at around 4.0 eV. The V_{oc} is determined by the difference between the HOMO of the donor and LUMO of

the acceptor [69], and generally follows the following relation [66]:

$$V_{oc} = (1/e)(|E^{Donor}HOMO| - |E^{PCBM}LUMO|) - 0.3\ V \quad (6)$$

A high V_{oc} is desired to maximize device performance, which implies a deep HOMO level in the donor. With a fixed LUMO level, deepening the HOMO level implies a widening bandgap, which reduces the number of photons available for absorption. This compromise between cell voltage and absorption follows the traditional Shockley-Queisser analysis for a general p-n junction PV device [70,71]. Similar to those results, a bandgap of about 1.5 eV is found to be optimal for absorbers in OPV devices as well, as outlined in Figure 1.4.

Following light absorption, the next donor material property under consideration is the exciton lifetime, which is often quantified as the diffusion length, L_D. If the exciton does not reach the D/A interface in time, it recombines in a thermally dissipative process, which is often a significant source of loss. The longer the exciton diffusion length the better, but unfortunately it is less than 20 nm for most organic semiconductors [72–78]. The exciton diffusion length can be improved by increasing the film crystallinity [79,80], though not nearly enough to enable the use of much thicker films. As a result, nanoscale film structuring is necessary to achieve higher efficiencies, which is discussed further in section 1.3.4. Nevertheless, a high exciton diffusion length is highly regarded when evaluating the effectiveness of organic semiconductors for use in OPV devices.

The final important property of an active layer semiconductor is its charge carrier mobility, which determines how easily the dissociated electrons and holes can reach the electrodes. Specifically, the hole mobility of the donor (μ_p) and the electron mobility of the acceptor (μ_n) are important. In general, mobilities of organic semiconductors compare poorly to their inorganic counterparts, but are sufficient and improving. Ideally, μ_p would be comparable μ_n to prevent the build-up of space charge [73,81], but this is rarely the case. The electron mobility of fullerene films is very good (8.5×10^{-3} $cm^2/V{\cdot}s$ [82]), so the primary concern is the hole mobility of the donor.

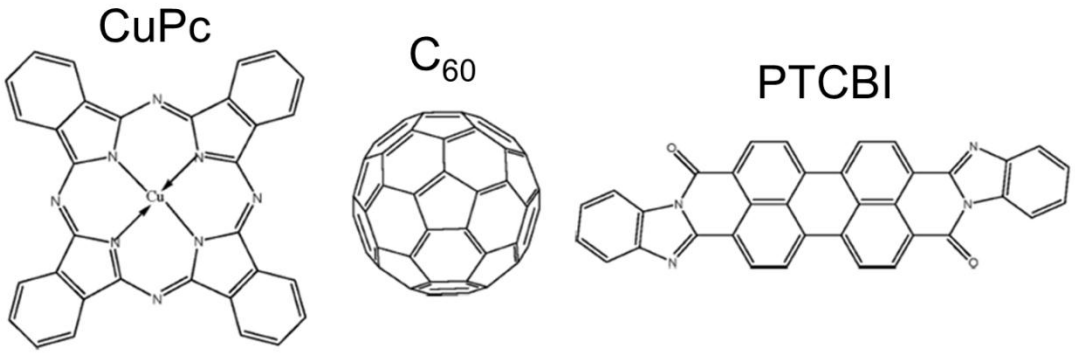

Figure 1.5 Small molecules commonly used in OPV devices.

Similar to exciton diffusion, charge carrier mobilities are also related to film crystallinity [81,83]. As such, annealing is often used to improve the hole mobility in the donor layer, which has been shown to increase the photoconversion efficiency by up to ten times [81]. Small molecule films generally have higher mobilities than polymer films, owing to their strong crystalline nature [73,81,82,84]. The purity of the donor material also plays a significant role here, with higher purity layers having higher mobilities due to fewer defect states [83,85]. The μ_p of the donor is usually within one or two orders of magnitude of the μ_n of the acceptor, which is sufficient to prevent the build-up of space charge from seriously hindering charge collection.

The majority of work in this thesis is aimed at nanostructuring vapor-deposited organic thin films. Therefore, only those materials that require vacuum evaporation are of interest, which draws our attention away from polymers, and towards small molecules. Metal phthalocyanine (MPc) materials have been used extensively in OPV devices, due to their superb exciton and charge transport properties, their suitable absorption spectrum, and their appropriate energy band alignment relative to C_{60}.

The most popular MPc material used in OPV devices is copper phthalocyanine (CuPc), shown in Figure 1.5, which has been used to achieve photoconversion efficiencies upwards of 5% [86]. Its absorption spectrum (see Figure 1.6) contains two absorption bands in the visible region, known as the Q band and the Soret band [87]. The Q band exhibits a two-peak profile in the

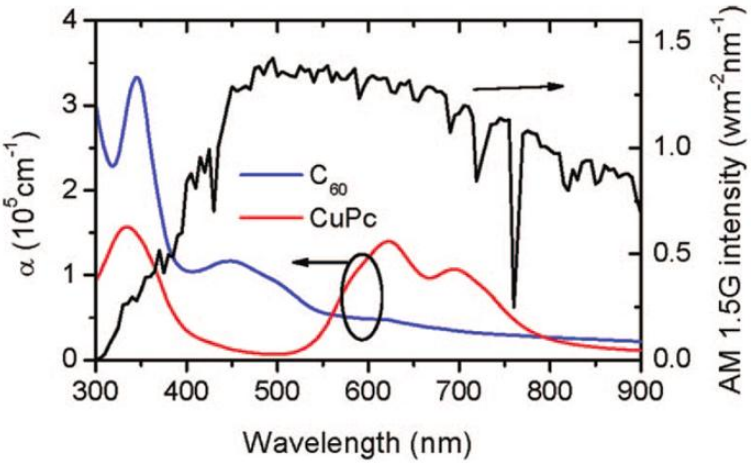

Figure 1.6 Absorption coefficient of CuPc and fullerene films plotted against the solar spectrum. Reprinted with permission from [73]. Copyright (2008) American Chemical Society.

500 ~ 800 nm wavelength range due to Davydov splitting [88,89], which originates from the π-π^* transition and is responsible for most of the photoconversion. The Soret band has a narrow absorption window between 300 ~ 400 nm, which also contributes to photocurrent. The lack of absorption in the 400 ~ 500 nm wavelength range is the greatest weakness of CuPc as an OPV donor material. The exciton diffusion length of CuPc is commonly cited at around 15 nm [72–75], though an upper limit has been estimated at 50 nm [90], or even 68 ± 20 nm [91]. The hole mobility is often measured to be in the range of 7×10^{-4} ~ 8.5×10^{-3} cm^2/V·s [82,84,92], but values of up to 0.01 cm^2/V·s have been observed as well [93–95]. Both the exciton diffusion length and hole mobility can be improved by using high purity materials, and by annealing the films after deposition to improve their crystallinity.

More recently, zinc phthalocyanine (ZnPc) has been the MPc molecule of choice, due to its superior L_D while otherwise having similar properties to CuPc [96]. A bilayer ZnPc device commonly yields a photoconversion efficiency of 1.4 ~ 1.8% [96,97], but substrate heating can increase it to 3.0% [97] and active layer mixing has yielded up to 3.9% [98]. Other MPc molecules have also been studied recently – such as SubPc, ClAlPc, ClInPc, and TiOPc – primarily to increase V_{oc} [99–104]. However, the extensive work performed on

CuPc and ZnPc OPV devices provides the best platform for which to evaluate the effects of nanoscale material structuring. These two molecules were therefore used for the majority of work in this thesis.

As mentioned previously, the most common acceptor molecule used in MPc-based OPV devices is the C_{60} fullerene (shown in Figure 1.5), or its solubilized version, [6,6]-phenyl-C_{61} butyric acid methyl ester ($PC_{61}BM$). The popularity of this molecule is primarily based on its strong electron mobility. More recently, C_{70} (or $PC_{71}BM$) has been used to boost efficiencies of OPV devices due to its superior absorption and ability to contribute to photocurrent [16,105–108]. Another noteworthy acceptor molecule used in combination with CuPc is perylenetetracarboxylic bis-benzimidazole (PTCBI), which was used in the original bilayer OPV device [14] and other early milestone devices [90,109,110], but is no longer being used due to its poor L_D and μ_p. This molecule is also shown in Figure 1.5. Solution processing of the acceptor layer is required for effective filling of nanostructured donor layers. The devices in this thesis utilize $PC_{61}BM$, hereafter referred to as PCBM, which is the most commercially available and studied soluble acceptor.

On a final note, one of the major criticisms of small molecule OPV devices is their dependence on vacuum deposition techniques. Solution-processable small molecules are being actively pursued as a result [111–113]. Heliatek, however, appears unfazed by this and has pioneered a roll-to-roll manufacturing line for small molecule OPV panels that incorporates vacuum processing. Presumably, this follows from the fact that small molecule OLED devices currently outperform their polymer competitors by a wide margin. Therefore, the prospects for vacuum-deposited small molecule OPV devices remain bright.

1.3.2. Interface materials

Charge extraction from the active layer requires conductance across organic/inorganic and molecular/polymer interfaces, each of which present their own challenges [114–118]. Not only must these interfaces conduct the appropriate charge carriers, ideally they would also help to confine excitons

to within the active layer by preventing quenching. Difficulties in charge transfer between layers are revealed by a characteristic s-shape, or "kink", in the current-voltage behavior [119–122], resulting in a poor fill factor. Interface layers, also known as buffer layers, are often used to facilitate charge transport across interfaces, which are broadly categorized as either an electron transport layer (ETL) or a hole transport layer (HTL). The ETL refers to the interface material between the acceptor material and the cathode, whereas the HTL refers to that between the donor and the anode.

In small molecule OPV devices, a HTL is not often used. Careful preparation of the anode surface can set the work function appropriately [123–128], which is usually done by a series of solvent and plasma cleaning procedures. A conducting polymer, poly(3,4-ethylenedioxythiophene) poly(styrenesulfonate) (PEDOT:PSS), is sometimes used to planarize the anode and reduce the extensive cleaning efforts required [119]. This layer is used extensively in polymer OPV devices, but its ability to etch indium out of the anode and facilitate degradation [29,34,129,130] have motivated the development of alternatives [131–136]. The devices presented in this thesis utilize PEDOT:PSS due to its commercial availability, ease of processing, and strong performance.

Though an HTL is not always necessary, an ETL is almost always required. In small molecule devices, ETLs are often referred to as exciton blocking layers (EBL), because they perform a dual function of conducting electrons and preventing exciton quenching at the cathode. The most widely used EBL is bathocuproine (BCP) [58,119,137], whose large bandgap is responsible for preventing exciton quenching. Perhaps the more important function, however, is to prevent damage to the active layer during deposition of the metal cathode [137,138]. As a result, the BCP layer fronts the damage, which results in defect states that enable electron transport out of the active layer. The disadvantages of using BCP are its rapid degradation and the high sensitivity of device performance to its thickness. Alternatives have been developed [131,139–144], but in most cases it is more than sufficient. As such, the only EBL used in this thesis is BCP.

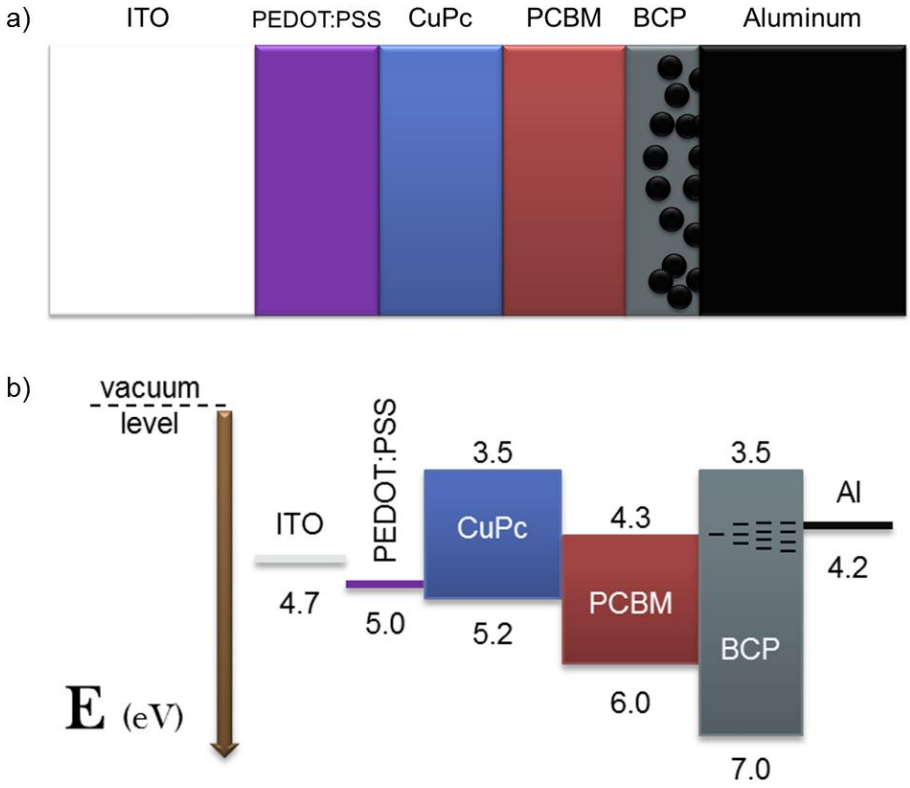

Figure 1.7 (a) Layout of material layers commonly used in small molecule OPV devices and (b) the corresponding energy band diagram. The physical penetration of Al into BCP shown in (a) creates the defect states that enable electron transport from the LUMO of PCBM to the Al, shown in (b). Panel (b) was adapted with permission from SPIE [145].

1.3.3. Electrodes

Typical OPV devices contain one transparent electrode (to let light into the cell, usually the anode) and one opaque one (usually the cathode). The only critical properties of the electrodes are strong lateral conductivity and a suitable work function. The difference between the work functions of the electrodes is responsible for setting up the built-in voltage, V_{bi}, which plays no role in exciton dissociation but is necessary for the collection of separated charge carriers [122]. Indium tin oxide (ITO) [146] is almost universally used as the transparent electrode in OPV devices, as it transmits over 80% of incident light over the entire visible spectrum. However, concerns over its long-term availability [8] encourage the development of alternatives [147].

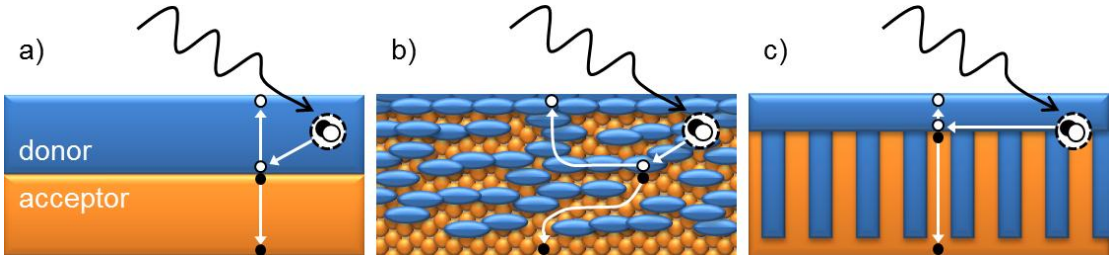

Figure 1.8 Active layer heterojunctions used in OPV devices: (a) bilayer, (b) mixed, and (c) ideal. Reprinted with permission from SPIE [145].

Some noteworthy examples are fluorine-doped tin oxide [148], metal nanofiber webs [149], ultrathin metal layers [150], metal grids [151,152], carbon nanotube films [153], and PEDOT:PSS-only electrodes [154].

The design of the opaque electrode is far less challenging because most conductors are opaque, leaving a wide range of possible choices. A high work function metal is required, so aluminum and silver are commonly used. Meanwhile, printable electrodes are being developed for commercial purposes to enable complete roll-to-roll processing [152,155–157].

Because the work in this thesis is focused on optimizing the active layer, the most conventional electrodes are used: ITO and aluminum. This completes the material selection for the platform small molecule OPV device used in this thesis. The corresponding physical device layout is shown in Figure 1.7a, and the energy band diagram is shown in Figure 1.7b. Energy band values were taken from [66,158].

1.3.4. Structural optimization of the active layer

The first OPV devices [14,58,110] contained a planar interface structure, termed the bilayer (Figure 1.8a), which remains a common platform for evaluating new materials today. As mentioned previously, however, light absorption in this layout is limited due to its trade-off with exciton diffusion. The optimal donor layer thickness for bilayer devices is around 20 nm [73,96,103], which is insufficient to capture the majority of incident light. Nanoscale material structuring can be used to circumvent this bottleneck, by increasing the D/A interface area and thereby enabling the use of thicker

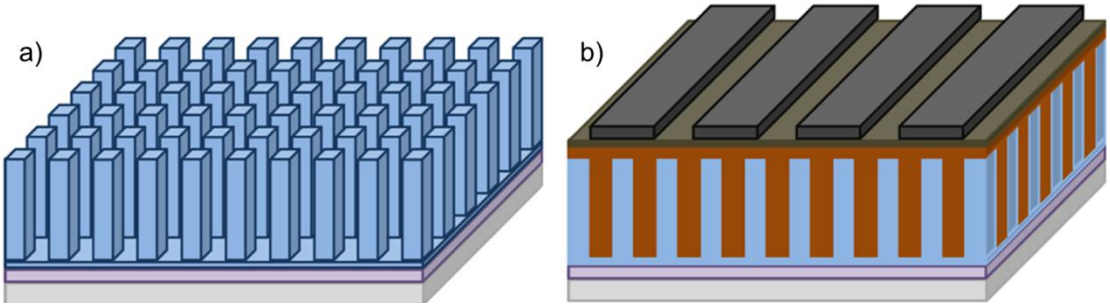

Figure 1.9 (a) ideal donor layer morphology and (b) complete OPV device [159]. Reproduced by permission of The Royal Society of Chemistry (RSC).

donor layers [73,104].

One of the most common active layer structures is the mixed heterojunction (MHJ), shown in Figure 1.8b, which provides significant interface area enhancement through co-deposition of donor and acceptor materials [82,86,100,101,160–162]. Mixed layers are usually homogenous, but concentration gradients have been used recently to further improve performance [101,163]. Similar to bulk heterojunction (BHJ) polymer blends, mixed small molecule heterojunctions can be accomplished via solution processing [111–113,164–166]. Regardless of the deposition technique, η_{ED} in a MHJ is close to 100% due to the close proximity of the D/A interface to wherever light is absorbed. However, due to reduced crystallinity and increased charge recombination, the mixed layer has considerably higher series resistance. This makes charge collection much more difficult, and η_{CC} is reduced to around 30 ~ 40% [73]. As a result, optimal performance is still found with only very thin active layers, usually 60 nm or less [86,100]. Nevertheless the MHJ remains the most successful way to achieve high efficiencies in small molecule OPV devices, with photoconversion efficiencies reaching 6.4% [162] (or 5.0% using CuPc [86]). The pursuit of a better heterojunction structure that removes the trade-off between exciton diffusion and charge collection remains.

Highly ordered interpenetrating networks of donor and acceptor materials that maintain clear conducting pathways to electrodes are characteristic of the ideal heterojunction, depicted in Figure 1.8c. Ideally,

these networks would resemble a chessboard arrangement, as illustrated in Figure 1.9, with column diameters that closely match the exciton diffusion length, and an overall active layer thickness of around 200 nm [73].

The fabrication of an ideal OPV device is challenging because the critical feature dimensions of the donor layer are so small (~ 20 nm). Various methods are being used to structure MPc's in this manner, such as organic vapor phase deposition [90,167], surface treatments prior to deposition [168,169], substrate heating during deposition [97,170], and recrystallization of films after deposition via solvent exposure [103,171–174]. So far, the optimal active layers achieved using these methods are still limited to thicknesses well below 100 nm, and therefore have poor overall absorption and mediocre performance. A noteworthy exception is a recent discovery by Nakamura's group whereby columnar donor films are achieved via thermal treatment of a spun-coat solution layer. These films achieve sub-30 nm column diameters, which is very close to the exciton diffusion length, resulting in efficiencies of up to 5.2% [175]. The recent 10% efficiency result by Mitsubishi was apparently achieved using Nakamura's techniques, though it has not yet been published and appears to be troubled by large area uniformity concerns [51].

This thesis describes new approaches to fabricating nanostructured donor films for OPV devices, by using glancing angle deposition (GLAD) [56,145,159,176,177], block copolymer (BCP) surface patterning [145,159,176], solvent recrystallization [177], argon plasma etching [178], nanostructured electrodes [179], and combinations thereof.

2. GLAD MPc THIN FILMS[1]

This chapter describes methods to create columnar MPc films suitable for use in OPV devices, as illustrated in Figure 2.1.

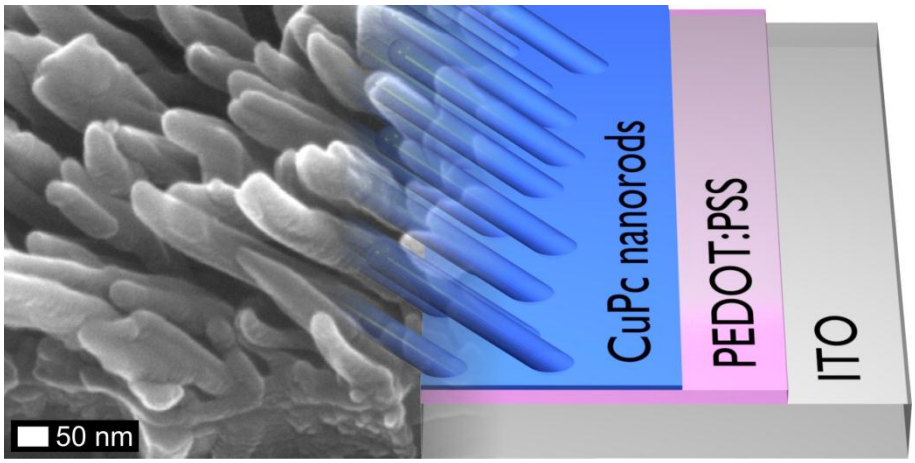

Figure 2.1 Illustration of how columnar MPc layers may form the foundation of an interdigitated OPV device.

2.1. Introduction

2.1.1. Glancing Angle Deposition

Glancing angle deposition (GLAD) is a physical vapor deposition technique that employs oblique deposition angles and substrate rotation to fabricate columnar thin films with high surface area [180–183]. A typical GLAD setup is shown in Figure 2.2. A high vacuum environment ensures that a collimated vapor flux arrives at the substrate at a consistent angle. In this way, the angle between the substrate normal and the vapor flux, α, can be manipulated to control nucleation density and the degree of self-shadowing during film growth (Figure 2.3). Limited surface diffusion of incident adatoms ensures that this self-shadowing causes growth of detached,

[1]Portions of this chapter were reproduced from [159] by permission of The Royal Society of Chemistry (RSC), and from [177], Copyright (2011), with permission from Elsevier.

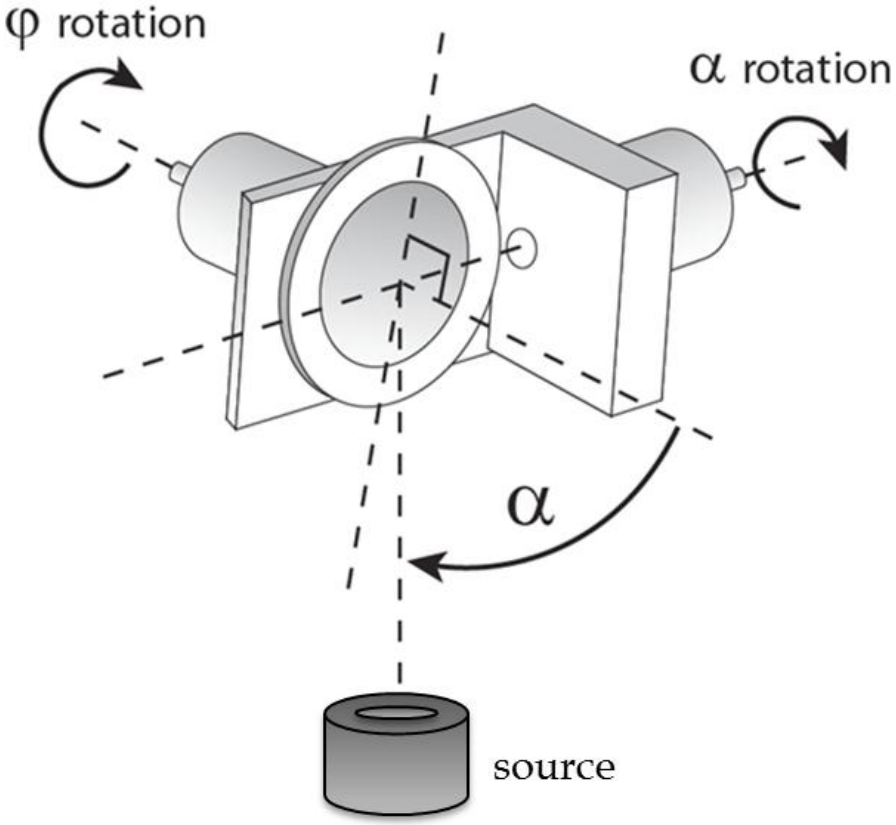

Figure 2.2 Illustration of the GLAD process: deposition angle α is the angle between the substrate normal relative to the incident vapor flux, and rotation angle ϕ is used to denote substrate rotation [184].

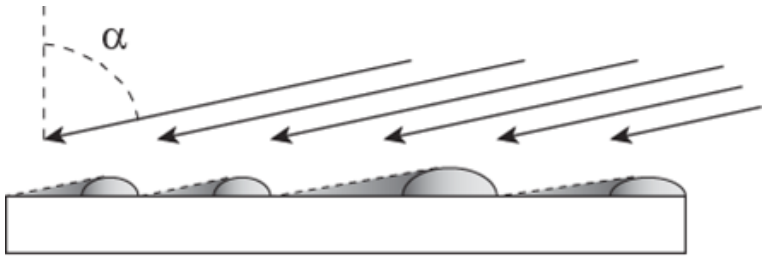

Figure 2.3 Self-shadowing of film nucleation sites enables the growth of columnar film morphology [184].

columnar structures. If the substrate is held fixed during deposition, the resulting film will exhibit slanted post morphology. However, the substrate can also be rotated during deposition (described by the angle variable ϕ), enabling many other morphologies, such as vertical posts, helices, chevrons,

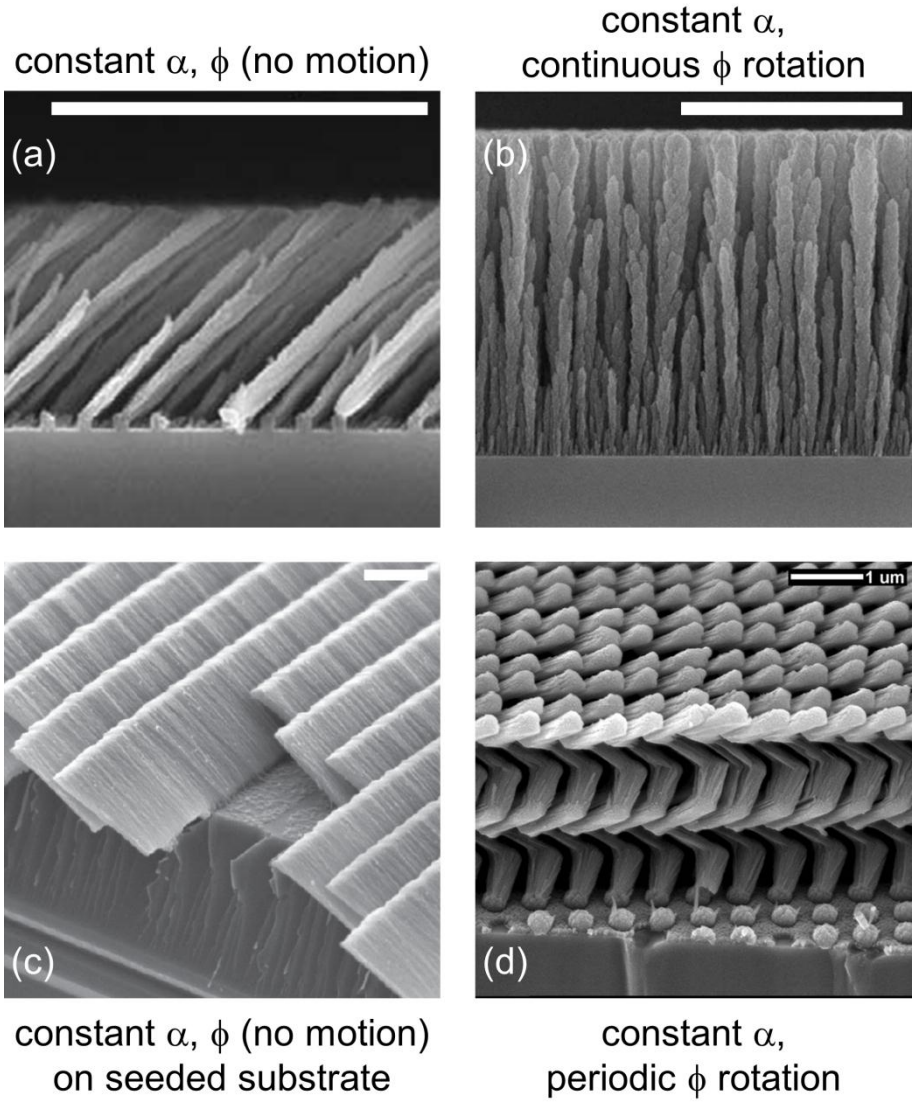

Figure 2.4 Archetypal GLAD films: (a) slanted posts, reprinted from [185], Copyright (2006), with permission from Elsevier, (b) vertical posts, reprinted with permission from [186], Copyright (2009), American Vacuum Society, (c) micro ribbons, reprinted with permission from [187], Copyright (2005), SPIE, and (d) square spirals, reprinted with persmission from [188], Copyright (2005), IEEE. Scale bars are 1μm.

and square spirals. Some examples are shown in Figure 2.4 [185–188].

Column broadening is commonly seen in GLAD thin films [186]. Minimizing this broadening can often be accomplished with a substrate motion technique known as ϕ-sweep [185,188,189]. As opposed to the

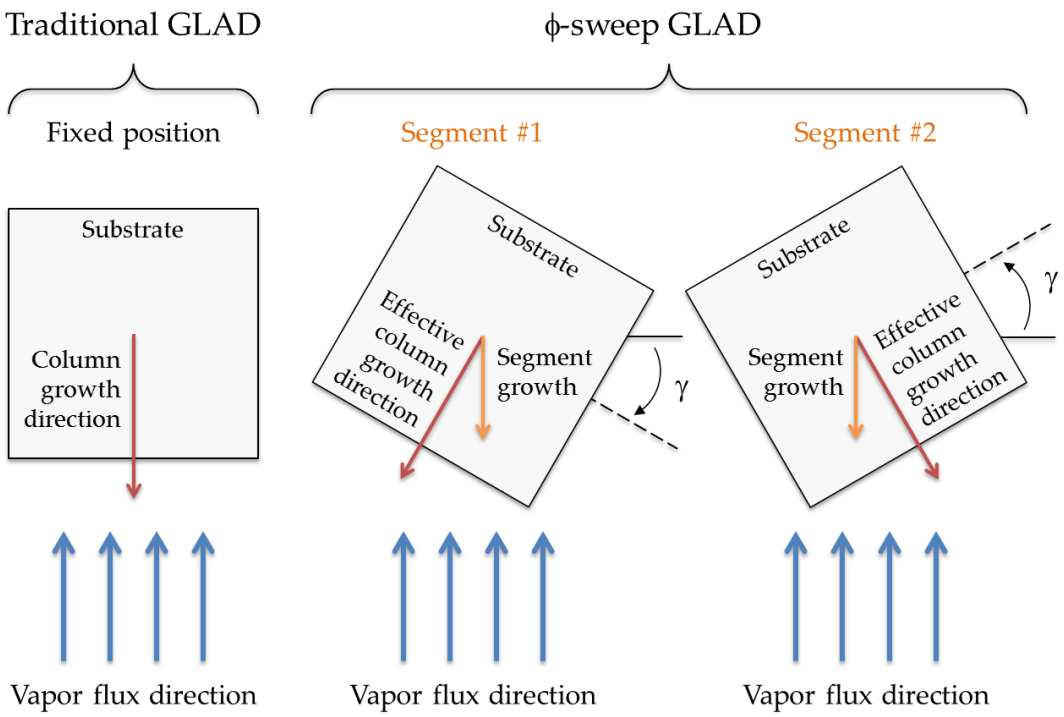

Figure 2.5 Illustration of the ϕ-sweep substrate motion technique.

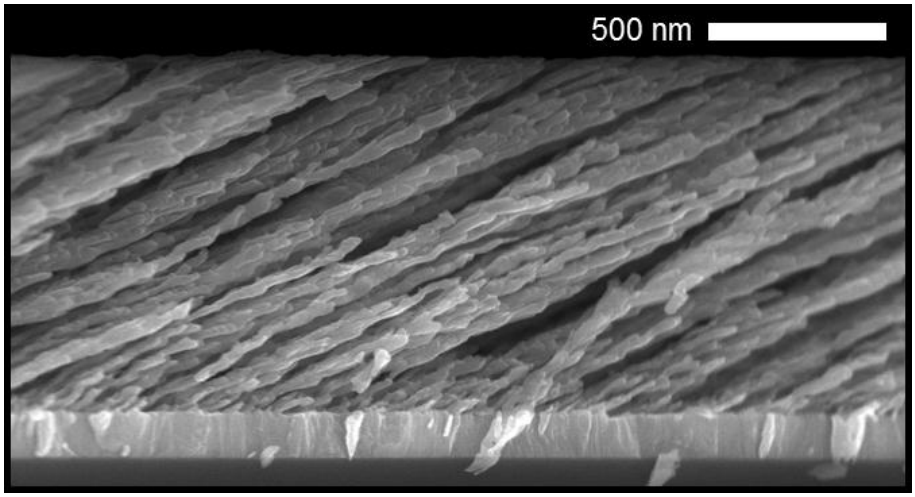

Figure 2.6 An aluminum film grown on ITO with ϕ-sweep, showing minimal column broadening.

continuous rotation in ϕ used to create vertical post films, the ϕ-sweep technique involves periodically and discretely rotating the substrate back and forth about the substrate normal as the film grows. Periodic shifts in ϕ by an

angle of ± γ break the anisotropy of shadowing, which discourages column broadening and results in a more uniform film with more surviving posts. This process is illustrated in Figure 2.5, and a ϕ-sweep aluminum film is shown in Figure 2.6 which clearly shows the ripple effect created from the alternating growth segments.

2.1.2. GLAD for OPV devices

Nanostructured CuPc via GLAD was first introduced for OPV devices in 2008 [56]. Since then, the use of GLAD for structuring materials in OPV devices has continued [159,176,177,190–195]. The technique has also been used to structure TiO_x in dye-sensitized [196,197] and hybrid organic-inorganic [198,199] solar cells.

Metal phthalocyanines are not the first organic small molecules to be structured with GLAD; reports on Alq_3, C_{60}, and pentacene date back to 2006 [200–202]. However, accomplishing columnar films with dimensions relevant for OPV devices is rather challenging. Column broadening, a common effect observed in GLAD films [186], makes it difficult to reach the ideal active layer thickness of 200 nm while maintaining small column diameters. This chapter outlines methods that can be used to constrain column broadening, resulting in films that are well-suited to ideal OPV architectures.

2.2. Experimental Details

2.2.1. Substrates

To mimic OPV device fabrication conditions, many of the films shown here were grown on an indium tin oxide (ITO)/glass substrate, coated with a thin layer of PEDOT:PSS (Clevios P VP Al 4083) via spin casting. ITO substrates received a 1 minute oxygen plasma cleaning treatment prior to PEDOT:PSS application. Bare Si substrates were used in parallel with the ITO substrates primarily for the purposes of obtaining XRD data, and some of the morphologies reported here are shown on Si. Microscope slides were also included in each deposition for the purpose of acquiring absorbance data.

2.2.2. MPc film deposition and characterization

CuPc and ZnPc material was acquired from Sigma-Aldrich and was subsequently purified via a one-step vacuum thermal gradient process at 400°C. Films were grown in a two-motor GLAD apparatus, as shown in Figure 2.2, at a throw distance of 34 cm. Film deposition was performed at high vacuum (2×10^{-7} Torr) with a source temperature of 390°C, resulting in a deposition rate of 0.7 Å/s at normal incidence. In all cases, a 10 nm planar layer of CuPc was deposited prior to GLAD growth. The images of CuPc films in Figure 2.7 were taken with a JEOL 6301F field emission SEM, while all other images were acquired via a Hitachi S-4800 field emission SEM. Absorbance data was acquired as the negative logarithm (base 10) of the transmittance spectrum from a Perkin Elmer Lambda 900 UV/VIS/NIR spectrophotometer. XRD spectra were collected by Michael Fleischauer using a Bruker D8 diffractometer equipped with a Cu source and area detector. Diffractometer instrument resolution was determined by collecting patterns from macroscale crystals of purified CuPc.

2.3. Results and Discussion

2.3.1. Basic GLAD CuPc films

Examples of CuPc thermally deposited at normal incidence ($\alpha = 0°$) on PEDOT:PSS coated ITO/glass substrates after 50 and 100 nm of growth are provided in Figure 2.7a and 2.7b, respectively. In both cases substrate rotation was employed at a rate of one rotation per 10 nm of growth to ensure uniformity across substrates. At both thicknesses the surface morphology is characterized by a slight roughness but overall is quite smooth. Basic GLAD structures grown at $\alpha = 85°$ using continuous rotation are shown in Figure 2.7c and 2.7d, respectively. In each case the substrate completed 10 rotations during deposition, at a constant rotation rate. The resulting structures exhibit a significant increase in surface area over the planar films of comparable thickness. As the GLAD films grow, random variations in column height lead

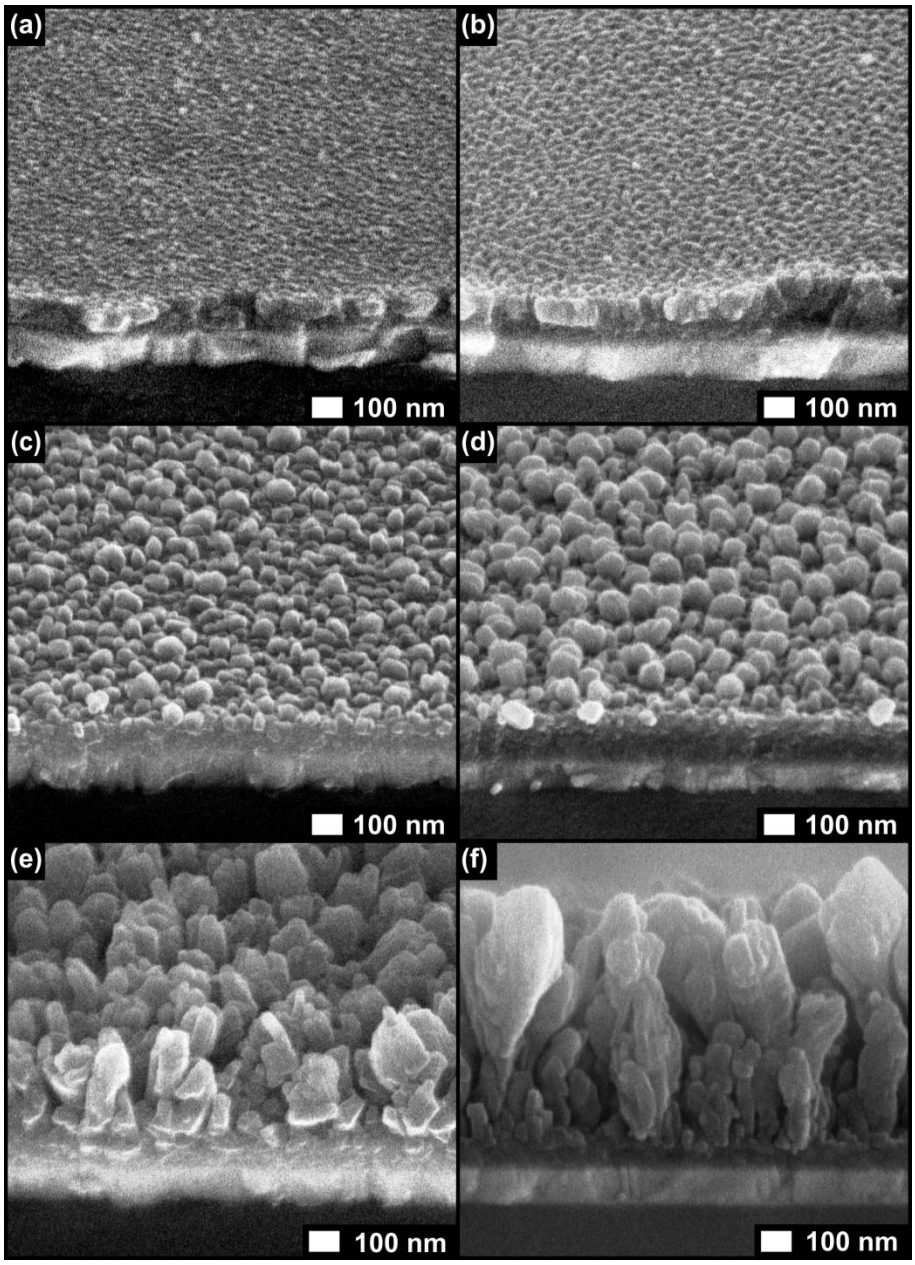

Figure 2.7 Planar and GLAD CuPc thin films grown on PEDOT:PSS coated ITO. (a,b) planar films grown to 50 and 100 nm. (c-f) GLAD films grown with a vertical post substrate motion algorithm at $\alpha = 85°$ (c,d) and $\alpha = 75°$ (e,f). Film thicknesses of (c-f) are 40, 100, 300, and 1000 nm.

to some columns being blocked from the incident flux while others tend to widen, leading to larger features. Hence, the difference in feature size

between the films shown in Figure 2.7c and 2.7d can be attributed to the difference in thickness (40 versus 100 nm). This broadening effect is amplified significantly as the films grow thicker, as shown in Figure 2.7e and 2.7f.

CuPc films grown at $\alpha = 75°$ to thicknesses of 300 and 1000 nm are shown as Figure 2.7e and 2.7f, respectively. In both cases the substrate was continuously rotated with one rotation per 100 nm of growth. At a film thickness of 300 nm the CuPc features already reach diameters of up to 200 nm (much larger than that desired for use in OPV devices). The 1 μm thick film exhibits even further column broadening; here the surviving post structures grew to hundreds of nanometers in diameter. This effect is undesirable from an OPV device perspective, but is included to provide a more complete picture of how CuPc behaves within the GLAD regime, and also to illustrate the power of the technique used to constrain this broadening (described in the following section).

Thin film deposition without substrate motion, also known as oblique angle deposition (OAD), is convenient from a manufacturing perspective and was therefore used to fabricate a variety of slanted post (SP) CuPc film morphologies. Some key results are shown in Figure 2.8 which explicitly highlights the effect of α on film porosity. The film grown at $\alpha = 60°$ is very dense and leaves little opportunity for the penetration of a filling material that would complete a photovoltaic device. Interestingly, films grown in this manner but at only a 20 nm thickness have been used to significantly improve photovoltaic device performance compared to a planar device architecture [190]. Thus, further device improvement may be possible if the improvements due to structuring are maintained while moving to thicker films with greater light absorption. A more porous and columnar film is achieved when $\alpha = 75°$, as seen in Figure 2.8b and 2.8d. Interestingly, here the surviving features branch out into multiple threads approximately 30 nm in diameter, indicating that CuPc has a natural tendency to form thin nanorods. Thus, the challenge is to fabricate uniform films of these nanorods that are equally spaced and a few hundred nanometres in length. Slanted post films were grown from $\alpha = 75°$ to 85°; higher angles resulted in greater porosity with more severe column

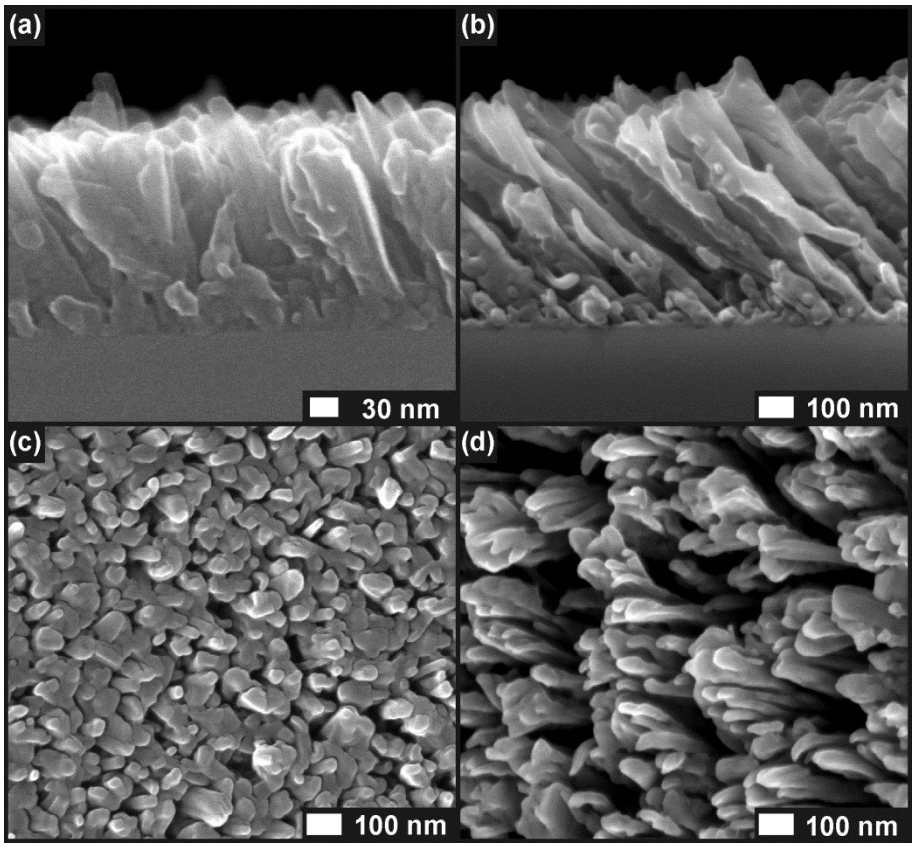

Figure 2.8 Side and top views of CuPc slanted posts grown on Si to (a,c) 240 nm thickness at $\alpha = 60°$ and (b,d) 700 nm thickness at $\alpha = 75°$.

broadening. The films grown at $\alpha = 75°$ exhibited the best balance between increased porosity and limited broadening, and were therefore used as the starting point for the improvements described in the following section.

2.3.2. Controlling broadening: ϕ-sweep

Slanted post morphologies were grown at $\alpha = 75°$ to thicknesses of 160 nm and 280 nm, as shown in Figure 2.9a and 2.9b, respectively. In both cases there is a large variance in post shape and diameter. Some surviving posts maintain the minimum post diameter of 30 nm throughout their growth while others exhibit significant broadening. In an effort to control this broadening and achieve greater uniformity throughout the film, the ϕ-sweep technique is used. As seen in Figure 2.9c, this technique yields a remarkably

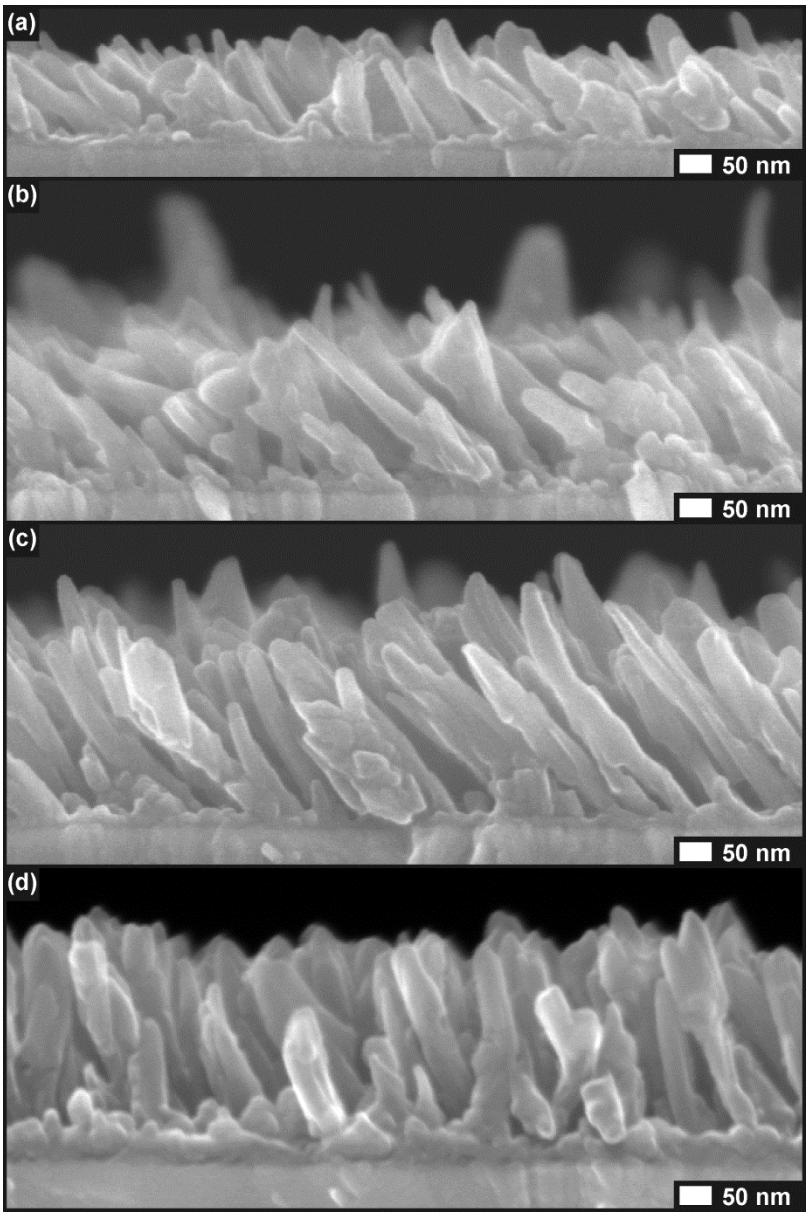

Figure 2.9 CuPc thin films grown on PEDOT:PSS coated ITO at $\alpha = 75°$ with and without ϕ-sweep algorithms. (a,b) Slanted posts grown with no substrate motion to thicknesses of 160 nm and 280 nm. (c) 370 nm thick film of slanted posts grown using ϕ-sweep with $\gamma = 30°$. Note that the films in (b) and (c) were grown to the same thickness as seen by the crystal thickness monitor in the deposition chamber. (d) 340 nm film of vertical posts grown via serial bideposition ($\gamma = 90°$). Both (c) and (d) were grown with a ϕ-sweep frequency of one cycle per 6 nm of growth.

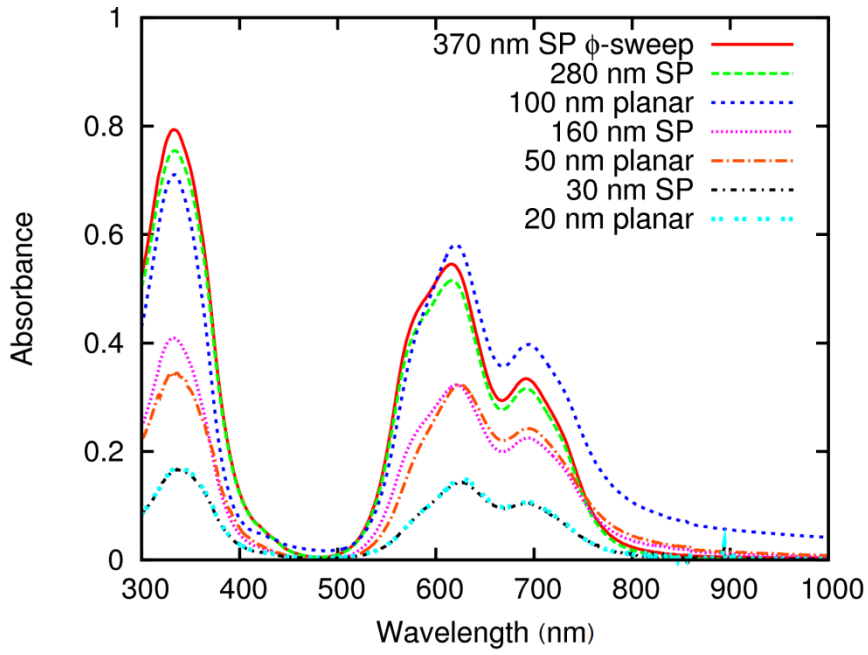

Figure 2.10 Absorption data for various planar and slanted post CuPc films.

improved CuPc film structure with reduced average column diameters and greater overall film uniformity. This film was grown with $\gamma = 30°$ and a frequency of one full sweep cycle per 6 nm of film growth.

Depending on the amplitude of the shift in ϕ, denoted by γ, the tilt observed in the posts will also be affected. As γ is increased the posts become less slanted until at $\gamma = 90°$ the posts are completely vertical – a case known as serial bideposition (SBD) [203]. At a low sweep frequency the result will be zigzag structures, while at a sufficiently high sweep frequency vertical posts will form. Therefore, this technique offers the ability to construct vertical post films without continuous rotation, which may be advantageous from a manufacturing perspective. An example result of this technique is shown in Figure 2.9d.

The optical absorption characteristics of these films provide further insight into the porosity enhancements achieved by structuring. The absorption data from various slanted post and planar CuPc films are compared in Figure 2.10. There are 3 groups of curves present. The 100 nm planar film exhibits comparable absorption to the 280 nm slanted post film

Table 2.1 Optical packing fractions and grain sizes for various CuPc films.

Film thickness (nm)	α	γ	Optical packing fraction	Grain size (nm)
20	0°	0°	1.00	18 ± 1
100	0°	0°	1.00	50 ± 10
240	60°	0°	0.83 ± 0.05	34 ± 4
30	75°	0°	0.65 ± 0.08	14 ± 1
160	75°	0°	0.32 ± 0.02	24 ± 2
280	75°	0°	0.31 ± 0.03	24 ± 2
370	75°	30°	0.25 ± 0.02	29 ± 2

and the 370 nm slanted post ϕ-sweep film, which suggests that these films contain approximately the same amount of CuPc material. Scattering effects of the GLAD films were neglected, as they typically become significant only for thicker films at higher deposition angles (near 85°) [204–206]. Furthermore, the GLAD films appeared clear and pristine, with no indication of cloudiness due to scattering. Therefore, the 370 nm slanted post ϕ-sweep film (Figure 2.9c) can be thought of as a rearrangement of the 100 nm planar film occupying nearly 4 times the volume, yielding an effective density (or packing fraction) of 0.25. This density is comparable to that expected from theory [207] and observed previously in inorganic GLAD films [206]. In addition, the ϕ-sweep technique succeeded not only in improving the uniformity of the 280 nm slanted post film, but increasing the porosity as well, as indicated by the increase in thickness. Similarly, the 50 nm planar and 160 nm slanted post films have comparable absorption, as do the 20 nm planar and 30 nm slanted post films, as expected. Evidently, even for very thin films the absorption data identifies a significant difference between planar and structured CuPc films. An understanding of the degree of porosity enhancement achieved in these GLAD films can be gathered from the films' packing fractions, as summarized in Table 2.1. The packing fraction of each film is calculated as the ratio of the optical density of the GLAD film to that of a planar film with comparable absorption (which is defined to have a packing

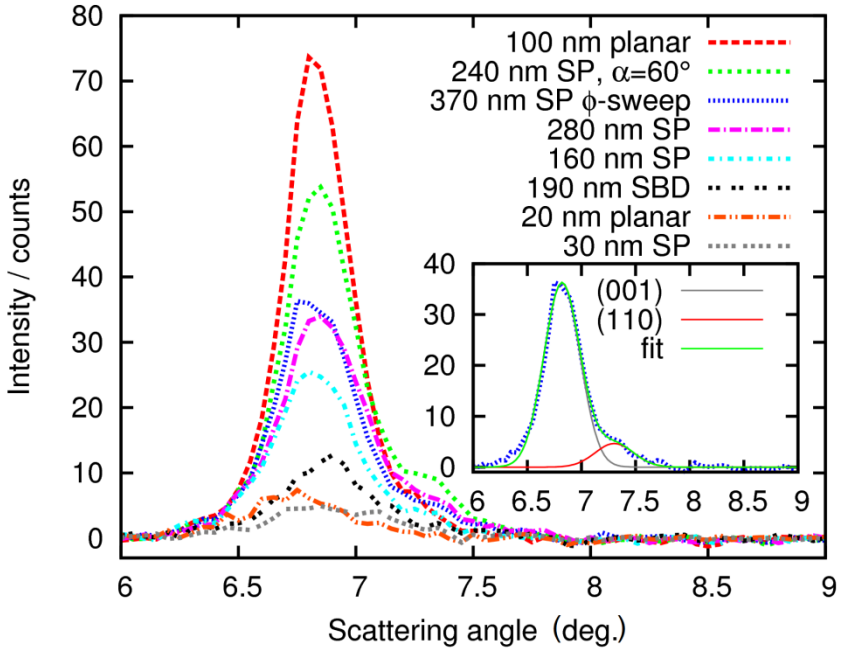

Figure 2.11 XRD data for various planar and GLAD CuPc films. All non-planar films were grown at α = 75° unless otherwise specified. Inset: an example of the curve fitting model used to calculate grain size. Calculated grain sizes are listed in Table 2.1.

fraction of 1). The optical density is calculated as the integration of the absorption curve divided by the film thickness. As such, a low packing fraction represents a higher porosity GLAD film and a high packing fraction represents a denser film.

As expected, the film grown at α = 60° exhibits the highest packing fraction due to its low porosity, as seen in Figure 2.8c. The 30 nm film grown at α = 75° has increased surface roughness compared to a planar film, but a high packing fraction is observed in this case as well because columnar structures are not yet fully formed. Films with more developed columnar morphologies (the 160 nm and 280 nm thick films) exhibit a lower packing fraction that is more characteristic of GLAD films. When ϕ-sweep is introduced (the 370 nm film), an even lower packing fraction is achieved. This is likely due to more uniform growth of individual columns with less column broadening, which results in a higher column survival rate and an increased

final film thickness.

XRD spectra from various planar and GLAD CuPc films are shown in Figure 2.11. Each pattern was fit using a two peak model based on Gaussian peak shapes corresponding to the (001) and (110) α-CuPc peaks at ca. 6.8 and 7.2° scattering angles, respectively [96,208,209]. An example fit is provided as the inset to Figure 2.11. Grain sizes listed in Table 2.1 were calculated using the Scherrer equation assuming spherical crystallites; grain size uncertainty is the result of measured peak widths for the sample and instrument resolution. Listed grain sizes of GLAD films are likely underestimates since the films exhibited strong texturing normal to the substrate and are columnar in nature, but the overall trends are valid.

In general, the grain sizes are limited by the smallest film feature dimension. For planar films the grain size is limited by the thickness, whereas for GLAD films it is limited by the column diameter. Distinct columns (found in the thicker films when $\alpha > 70°$) lead to grain sizes in the range of 25 nm, a significant fraction of the column diameter. This implies that each column is composed of relatively few grains, which will encourage efficient exciton diffusion and charge transport [79]. Of particular interest is the 370 nm ϕ-sweep film, which exhibited a slight increase in grain size relative to other GLAD films of comparable thickness. Therefore, the ϕ-sweep technique succeeded in improving both film uniformity (as discussed above) and film crystallinity, providing strong merit for the utilization of this technique.

Evidently, GLAD and the ϕ-sweep technique are very effective at tailoring the morphology and resulting porosity of CuPc films while maintaining comparable crystallinity to planar morphologies. All film morphologies discussed in this section were grown on PEDOT:PSS coated ITO substrates, making them amenable to OPV device fabrication.

2.3.3. Nanostructured ZnPc films via GLAD

Thin films of ZnPc were also grown under several sets of conditions by varying α and the film thickness, and using ϕ-sweep. In Figure 2.12, a planar ZnPc film is compared to various slanted post GLAD films grown at different

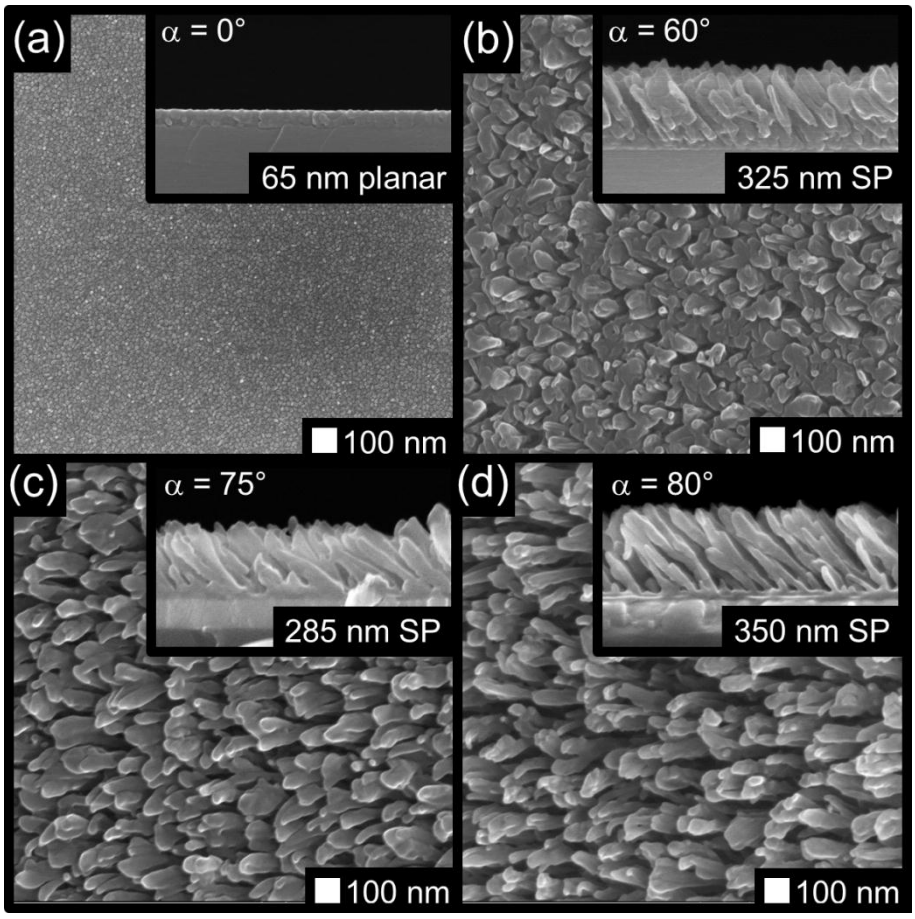

Figure 2.12 Aerial and cross-sectional views of various planar and slanted post (SP) ZnPc thin films. The angle of incidence (α) is shown in each case. The substrates in each case are (a,b) Si and (c,d) PEDOT:PSS coated ITO.

α values, which illustrates the effect of α on morphology. The film porosity increases with α, as expected due to increased shadowing. With the exception of the film in Figure 2.12b, which was grown with no substrate motion, a ϕ-sweep substrate motion program was used to grow each GLAD film, with γ = 30° and one full sweep cycle per 4-5 nm of growth.

Ideally, the donor layer morphology would have columns with diameter close to that of its exciton diffusion length (15nm for ZnPc [72]), with a thickness or length of around 200 nm [73]. The films shown in Figure 2.12c and 2.12d begin to mimic this arrangement and are grown to even

greater thicknesses while maintaining relatively uniform average column diameters. Unsurprisingly, GLAD-structured ZnPc and CuPc appear to be very similar.

2.4. Summary

An optimization of nanostructured CuPc and ZnPc thin films suitable for use in OPV devices was performed, utilizing the various techniques available within the glancing angle deposition process. Columnar structures were formed from tens to hundreds of nanometers in length with strong control over column diameter and spacing. Column broadening was shown to be a significant challenge for films beyond 100 nm in thickness, but was mitigated by use of the ϕ-sweep technique. This technique enables the formation of nanostructured MPc films that are engineered for the short exciton diffusion lengths inherent to these materials. The methods described in this chapter illustrate the strong potential that the GLAD technique holds for direct and controllable fabrication of ideal geometry OPV devices. To add additional control over nanostructured MPc film morphologies, surface patterning techniques are used to pre-define column diameters and spacing, as discussed in the following chapter.

3. SEEDED GLAD MPc FILMS[1]

3.1. Introduction

As mentioned in Chapter 1, the ideal OPV active layer heterojunction is an interpenetrating network of donor and acceptor materials that maintains clear conducting pathways to the electrodes. Columnar films of donor or acceptor materials are needed to build this heterojunction, with column diameters that closely match the exciton diffusion length [73]. Chapter 2 showed how the GLAD technique can be used to create columnar films of MPc materials to form the donor layer of an ideal heterojunction. However, a columnar morphology is only part of the challenge; ideally, the columnar array would exhibit periodicity as well, with tightly packed and equally spaced nanocolumns [73]. This chapter describes how surface patterning can be used to introduce order and periodicity into columnar GLAD MPc films, to further approach the ideal morphology.

Nucleation sites for GLAD film growth are randomly distributed when grown on a planar substrate, and shadowing determines which features

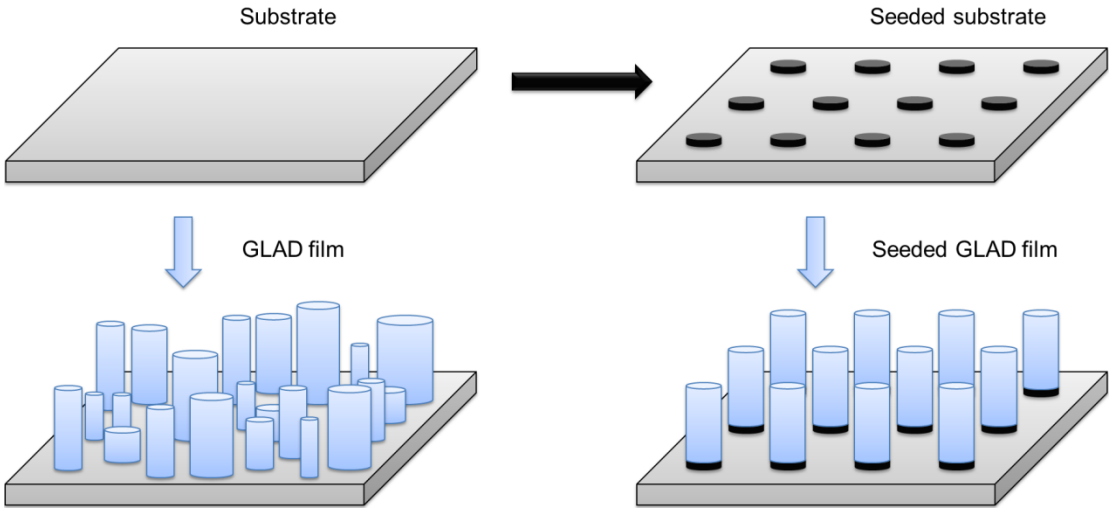

Figure 3.1 GLAD film growth on seeded vs. unseeded substrates.

[1]Portions of this chapter were reproduced from [145] with permission from SPIE, and from [159] by permission of The Royal Society of Chemistry (RSC).

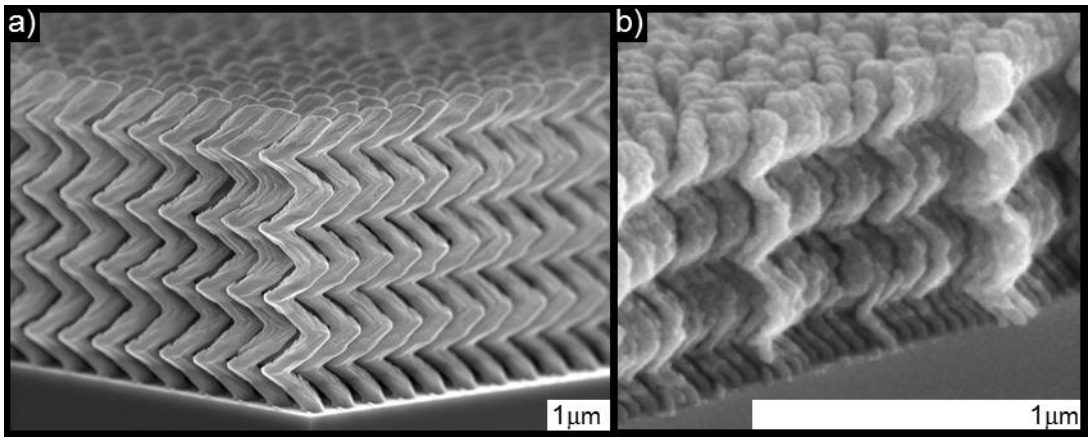

Figure 3.2 Seeded GLAD films: (a) archetypal square spiral photonic crystal accomplished using electron beam lithography substrate seeding, and (b) a pseudo-ordered chiral TiO_x film accomplished using block copolymer substrate seeding. Panel (b) adapted with permission from [210], © 2009 WILEY-VCH Verlag GmbH & Co. KGaA, Weinheim.

continue to grow as the film thickens. By seeding the substrate prior to deposition, the growth sites can be predefined in order to encourage a particular morphology. The spacing and pattern of the seeds can be manipulated to tailor the characteristics of the resulting GLAD film, such as post diameter, spacing, and periodicity. Periodic seed patterns lead to periodic films, with improved uniformity, as illustrated in Figure 3.1. This concept has been demonstrated previously (see Figure 3.2), primarily for optical purposes [185,188,189,210,211]. Even without GLAD, donor layer films grown on a patterned surface can lead to higher active layer interface area, as illustrated in the right hand column of Figure 3.3. With GLAD, this technique could yield a truly ordered, ideal heterojunction, as illustrated in the left hand column of Figure 3.3.

This chapter investigates the ability of surface patterns to control the columnar dimensions of metal phthalocyanine (MPc) films deposited with GLAD. Conventional surface patterns from electron beam lithography [185,188,189] are used as a starting point, but emphasis is placed on the block copolymer (BCP) patterning method [212–219] due to its superior potential for low-cost manufacturing and the suitability of its patterns for OPV. In this

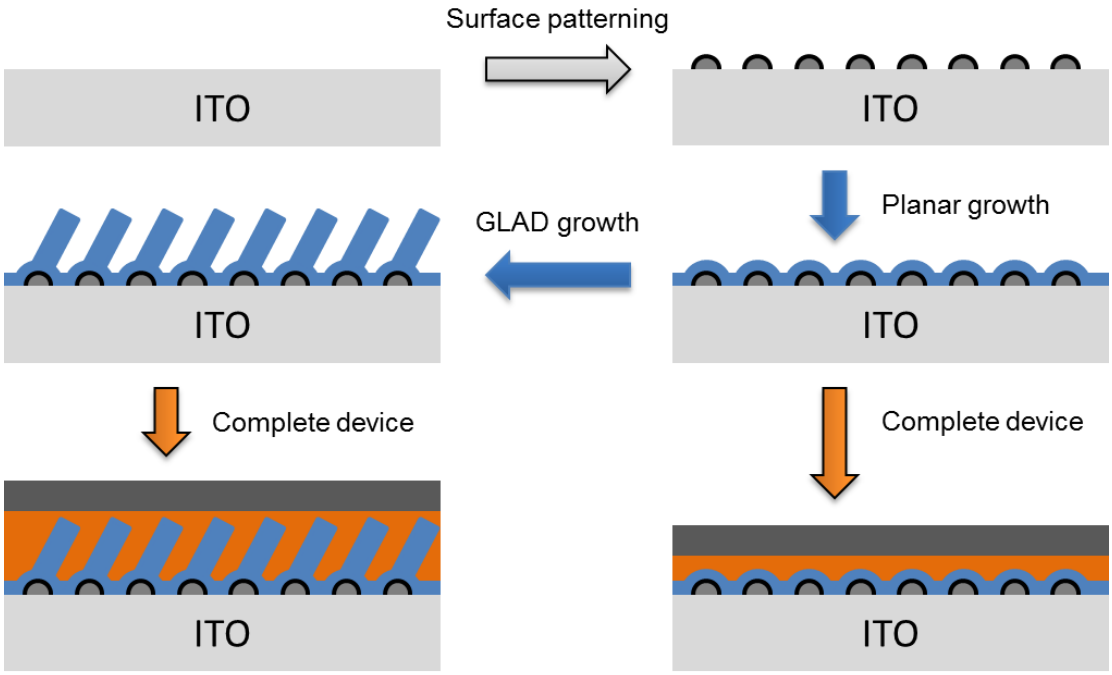

Figure 3.3 OPV device concepts using seeded donor layers. The blue layer is an MPc film, the orange layer is the acceptor layer (PCBM) and the dark grey layer is the cathode. An ordered activer layer structure with high interface area can be achieved with both planar and GLAD films.

process, a BCP film is applied to a surface via spin coating, after which the film polymerizes and the two polymers segregate naturally (see Figure 3.4). One of the polymers will often assume a distinct pattern, and solvent annealing can be used to encourage the formation of different patterns. After polymerization, the patterned polymer is metallized by bathing the film in an acidic solution containing metal ions. The polymers are then both removed by oxygen plasma, leaving a metallic pattern on the surface. The fingerprint and dot patterns seen in Figure 3.4c and 3.4d are the most common patterns made with the block copolymer technique. Dot patterns are particularly useful for seeding GLAD films. The spacing between dots (also referred to as "seeds") can be controlled by varying the weight ratio of the two blocks in the block copolymer. Variations in film thickness and seed spacing are used in this chapter to identify the geometrical limits of ordered MPc film morphologies. Efforts towards patterning ITO and developing a patterning process

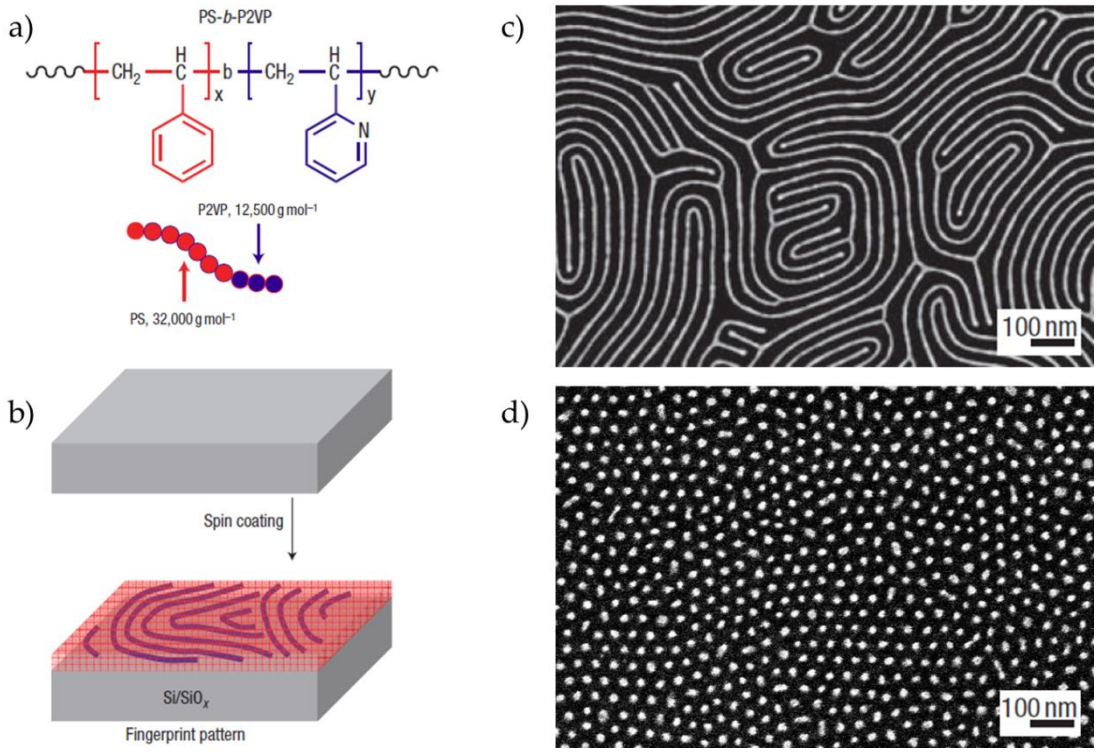

Figure 3.4 Illustration of the block copolymer patterning process: (a) block copolymer structure, (b) spin coating and polymerization process, (c) example of a fingerprint pattern, and (d) example of a dot pattern. Panels (a-c) were adapted by permission from Macmillan Publishers Ltd: (Nature Nanotechnology) [215], copyright (2007).

compatible with OPV device fabrication are also shown.

3.2. Experimental Details

3.2.1. Substrates

Electron beam lithography seed patterns were fabricated by Mark Summers by spin-coating Fox-12 Flowable Oxide (Dow Corning) onto a Si wafer at 2000 rpm and exposing at 5 kV in a RAITH 150 EBL instrument (RAITH GmbH). BCP patterns were provided by Nathanael Wu, and were also deposited primarily on Si substrates. Prior to the deposition of BCP, the substrates were cleaned in oxygen plasma at 300 mTorr for 3 minutes. The substrates were then spin coated with a 1.5% w/w solution of BCP in toluene

to create a BCP film of approximately 50 nm. To create different dot spacings, two different sizes of polystyrene-*block*-poly(2-vinylpyridine) (PS-*b*-P2VP) were obtained from Polymer Source and used for the BCP: M_n = 66.5 kg/mol and M_n = 183.5 kg/mol. The substrate was then placed in a sealed chamber in the presence of tetrahydrofuran solvent vapor to induce self-assembly into regular dot patterns. To fill the P2VP dots with platinum, the samples were then immersed in a solution with HCl (0.9%, aq) and Na_2PtCl_4 (10 mM, aq) for 3 h before being thoroughly rinsed with water and dried. An oxygen plasma was then applied to the samples at 50 mTorr and 30 W for 25 s to remove the BCP film and to reduce the metal salt into solid metal structures. Dot spacings that resulted from these two polymers were typically 40 nm and 60 nm. Films were deposited on ITO and PEDOT:PSS coated ITO substrates as well, for comparison to seeded films. ITO was cleaned with oxygen plasma, and PEDOT:PSS (Clevios P VP Al 4083) was spun for 30 seconds at 4000 rpm, and then baked at 80°C for 10 min.

3.2.2. Film deposition

Films were deposited with CuPc and ZnPc (Sigma-Aldrich) in a typical two-motor GLAD apparatus with a throw distance of 34 cm. Planar films (i.e. $\alpha = 0°$) and vertical post (VP) GLAD films were deposited with continuous substrate rotation. The ϕ-sweep technique described in Chapter 2 was used when depositing slanted post (SP) GLAD films. A shift angle of $\gamma = 30°$ was used in all cases except for the electron beam seeded sample, with a full sweep cycle occurring approximately once per every 5 nm of film growth. All GLAD films were deposited at $\alpha = 80°$ unless otherwise stated, and were preceded by a 5 nm planar layer deposited at $\alpha = 0°$.

3.3. Results and Discussion

3.3.1. Conventional seeding

Seeded GLAD films are most commonly accomplished using Si wafers patterned with electron beam lithography. As such, it was logical to follow

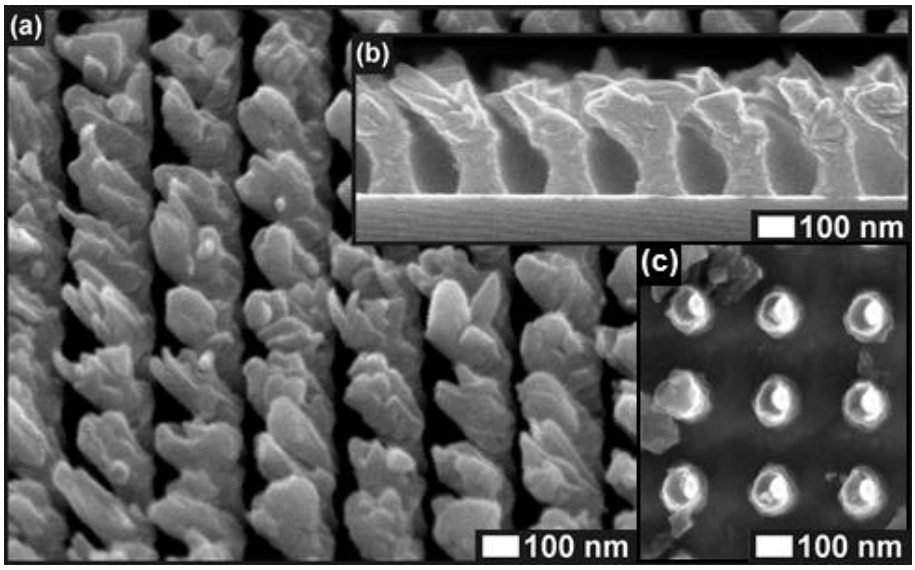

Figure 3.5 Oblique (a) and side (b) views of a GLAD CuPc film grown at $\alpha = 80°$ with ϕ-sweep (one sweep cycle per 4 nm of film growth, with $\gamma = 26.5°$) on a seeded Si substrate. The square seed pattern (c) was made with electron beam lithography and had a seed spacing of 250 nm.

the same procedure as a first demonstration for CuPc, which is shown in Figure 3.5. Here, seeds were arranged in a square lattice pattern with 250 nm center-to-center seed spacing, as seen in Figure 3.5c. The ϕ-sweep technique was used for the CuPc deposition, with $\gamma = 26.5°$ to provide the optimal shadowing geometry of the seeds during deposition [189]. The CuPc material conformed well to the periodic seeding pattern, yielding a very uniform array. However, though this seed spacing is relatively small compared to previous works [185,188,189], it is far too large to be relevant to OPV devices. In addition, electron beam seeding techniques are impractical from a manufacturing perspective, as they are expensive, slow, and cannot be applied over large areas. Nevertheless, this demonstration is enough to suggest that MPc films adhere well to surface patterns.

3.3.2. Block copolymer seeding

To accomplish seeded MPc films with a more ideal spacing, the block copolymer method is employed. Hexagonal patterns of platinum seeds on Si

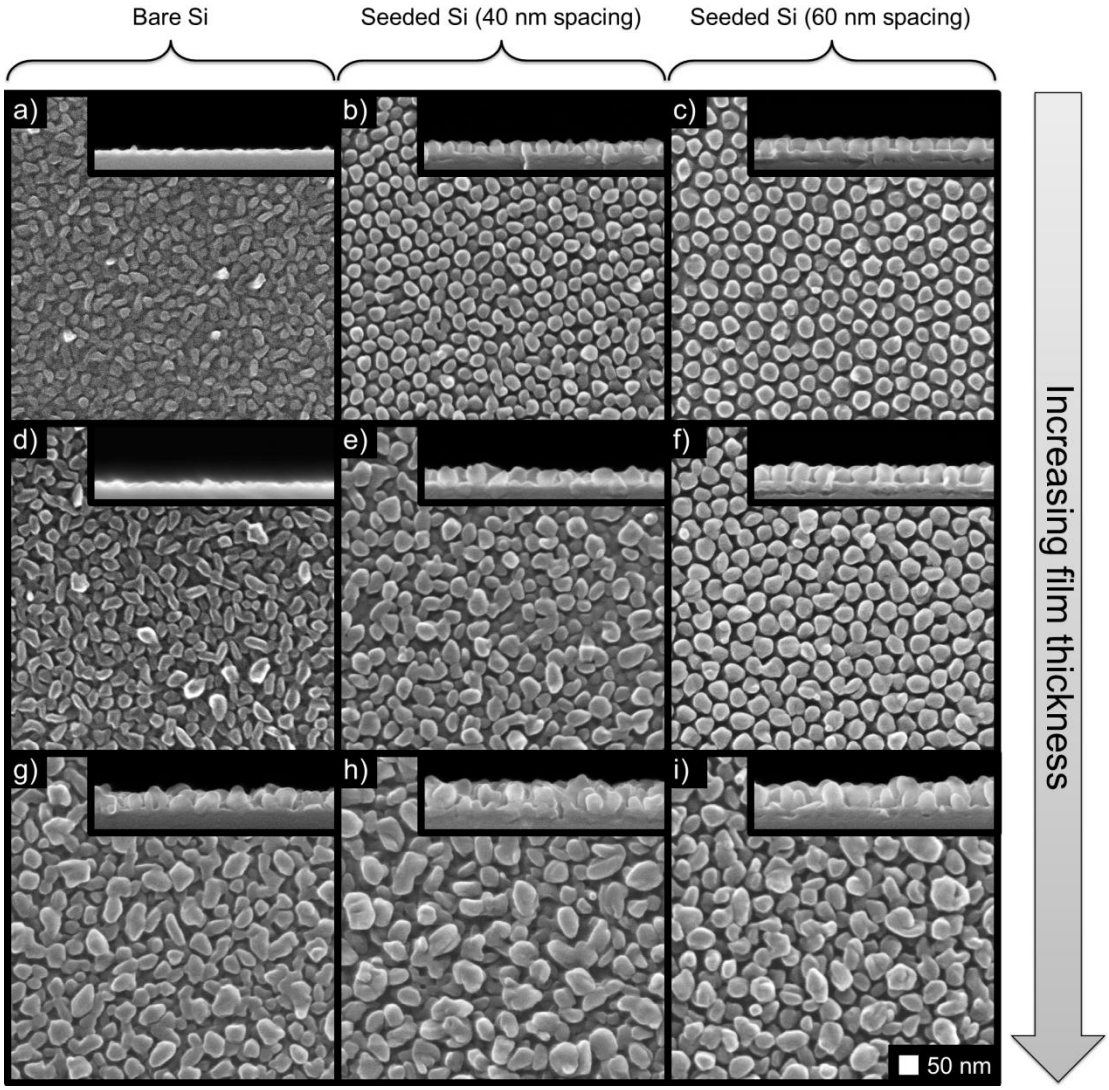

Figure 3.6 Vertical post (VP) ZnPc films of various thicknesses on seeded Si vs. bare Si. Seeded substrates were fabricated using block copolymer surface patterning techniques.

were made with approximately 40 and 60 nm spacing. Vertical post (VP) ZnPc GLAD films were grown on these seeded substrates, as well as on bare Si, which are shown in Figure 3.6. In all cases, a 5 nm planar layer was deposited prior to moving to higher deposition angles for the GLAD portion. Three different GLAD film thicknesses were grown, between approximately 10 nm and 70 nm, to observe the evolution of the films as they grow. The films adhere very well to the seed patterns in the initial stages. As the films

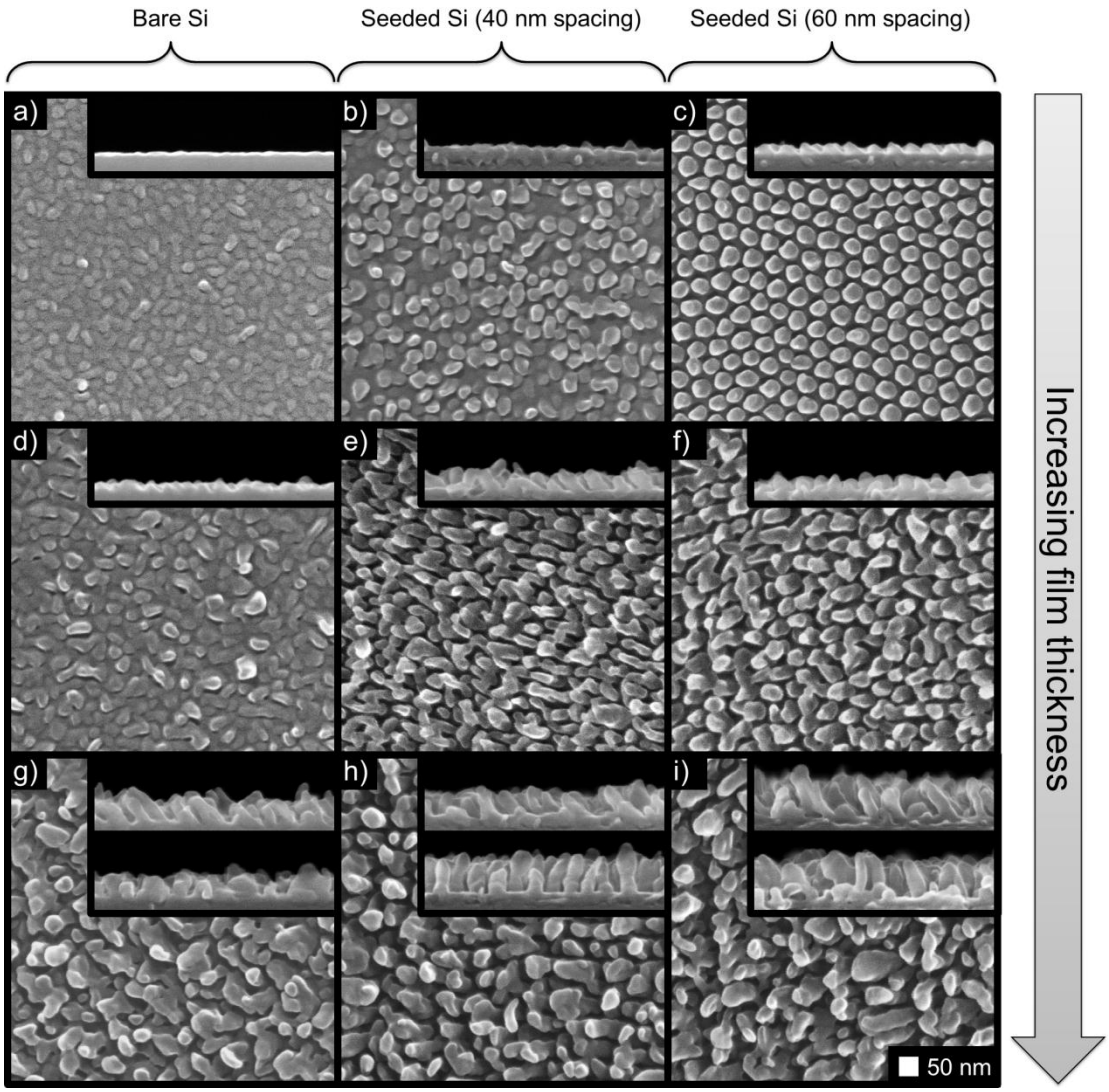

Figure 3.7 Slanted post (SP) ZnPc films on seeded Si vs. bare Si. The inset images in (g-i) are taken orthogonally to each other.

grow thicker, competition between features causes some of the film features to outgrow the others, and the morphology strays from the pattern. When the film grows thicker than the seed spacing, the morphology is virtually indistinguishable from the one grown on a bare Si substrate.

To mitigate the pattern loss, the same set of films were grown using the ϕ-sweep substrate motion technique, which are shown in Figure 3.7. These films were deposited at the same deposition angle, and received the same amount of incident vapor flux as the corresponding films in Figure 3.6;

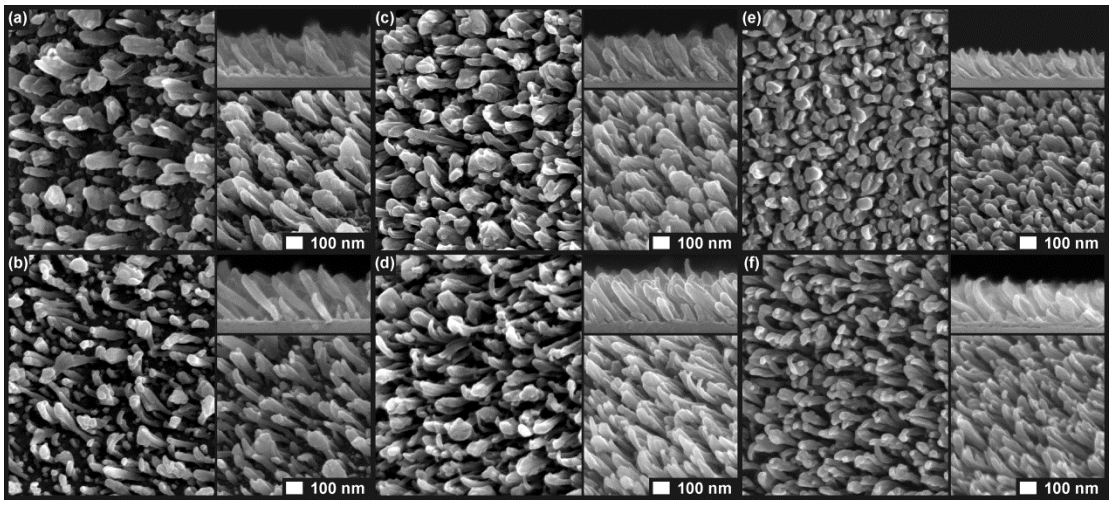

Figure 3.8 Top (large image), side, and oblique views of various CuPc (a-d) and ZnPc (e,f) films deposited at $\alpha = 85°$ (a,b) and $\alpha = 80°$ (c-f) onto bare Si (top row: a,c,e) and seeded Si (bottom row: b,d,f). All depositions utilized a ϕ-sweep substrate motion program with $\gamma = 30°$ and 60 full cycles (one cycle per 4~5 nm of growth). In addition, each film received an equal amount of incident vapor flux as seen by the CTM in the deposition chamber.

the only difference was the substrate motion during deposition. In these cases, although the pattern resemblance still fades as the films grow, the survival rate of individual columns and pattern fidelity in the thickest films (3.7h and 3.7i) are slightly better than in the corresponding films in Figure 3.6. Film uniformity improves and the overall film thickness increases as a result of a more uniform distribution of material. There is less bridging between individual columns and therefore a higher column density, making them highly attractive from an OPV device perspective. These effects are further investigated in the following section for much thicker films.

3.3.3. Extended growth of BCP-seeded GLAD MPc films

GLAD CuPc films were deposited on both bare and seeded Si substrates at $\alpha = 80°$ and 85°. In all cases the ϕ-sweep technique was also employed with $\gamma = 30°$ and a frequency of one full sweep cycle per 5 nm of film growth. One zinc phthalocyanine (ZnPc) film was also grown for

Table 3.1 Film thicknesses and column densities for seeded and unseeded MPc films under different growth conditions.

Substrate	Material	α	Film thickness (nm)	Column density (μm^{-2})
bare Si	CuPc	85°	265 ± 15	38 ± 1
seeded Si	CuPc	85°	320 ± 20	51 ± 3
bare Si	CuPc	80°	280 ± 18	58 ± 3
seeded Si	CuPc	80°	305 ± 10	74 ± 4
bare Si	ZnPc	80°	170 ± 12	88 ± 4
seeded Si	ZnPc	80°	260 ± 16	102 ± 3

comparison, with the same deposition conditions as the CuPc film at $\alpha = 80°$. These films are all displayed in Figure 3.8 and the film thicknesses and column densities are summarized in Table 3.1. In all cases, the seeded substrates encouraged a higher column density and thinner columns. Overall film thicknesses were increased with the seeded substrates, due to the limited broadening, improved column uniformity, and decreased intercolumn spurious growth. Keeping in mind that the films on both the seeded and unseeded substrates were fabricated in the same deposition (for each α value), this thickness increase may be interpreted as the result of material being distributed more uniformly throughout thinner, longer columns. The effect of α on film porosity is also evident when comparing these films: higher α results in a more porous film, as expected. In addition, Figure 3.8b clearly illustrates the competition between features that occurs during growth, as there are many small posts visible within the depth of the film. Interestingly, the seeded ZnPc film contained columns of even smaller diameter than the CuPc film grown under the same conditions (Figure 3.8d vs. 3.8f). Thus, it appears that having an array of seeds denser than the natural column spacing sets up competition between seeds that determines a unique structure for each material and deposition angle.

The morphologies of CuPc and ZnPc observed at $\alpha = 80°$ on the seeded Si substrate are certainly most ideal from an OPV device perspective, as they

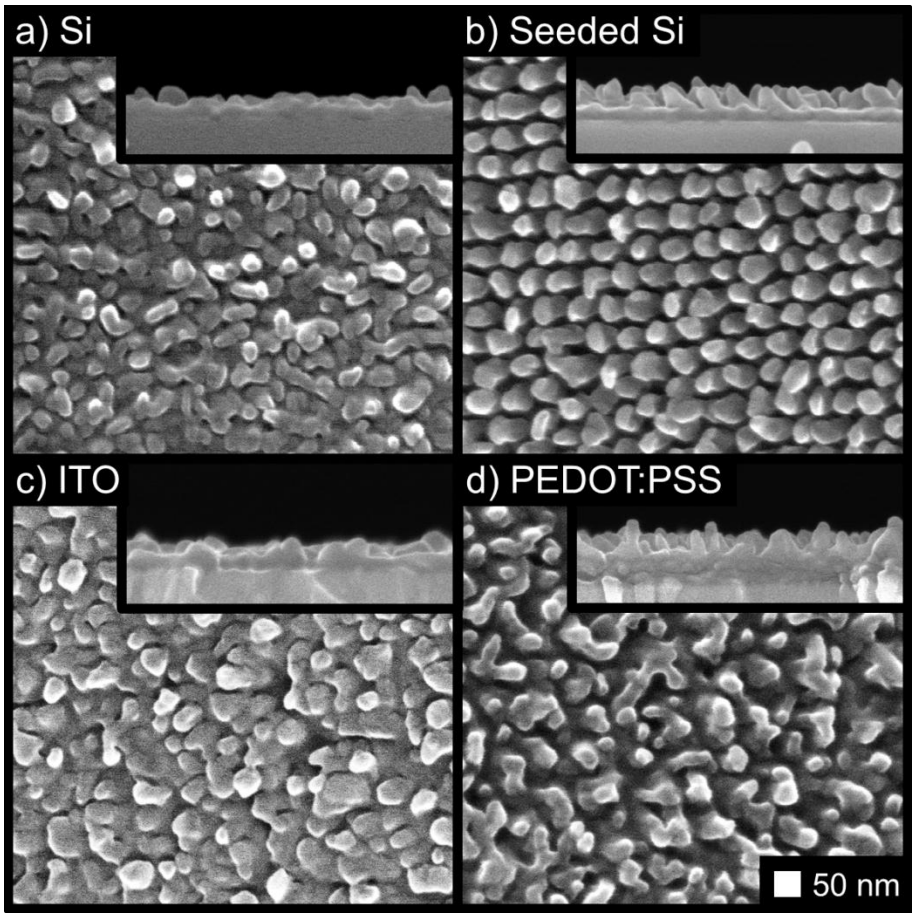

Figure 3.9 Thin GLAD ZnPc films on various substrates (denoted in the image).

contain dense arrays of uniform columns that are mostly restricted to diameters of 50 nm or less (this is comparable to the exciton diffusion length in these materials). Restricting the column diameters to these dimensions is critical for maintaining a low average distance between the point of exciton generation and the D/A interface (where dissociation occurs). It is significant to observe the degree to which the film morphology can be influenced – and therefore manipulated – through substrate seeding. This provides motivation for further exploration in this area and for adapting the technique to be compatible with OPV device fabrication.

3.3.4. Towards device compatibility

A morphology comparison between substrates that are more relevant

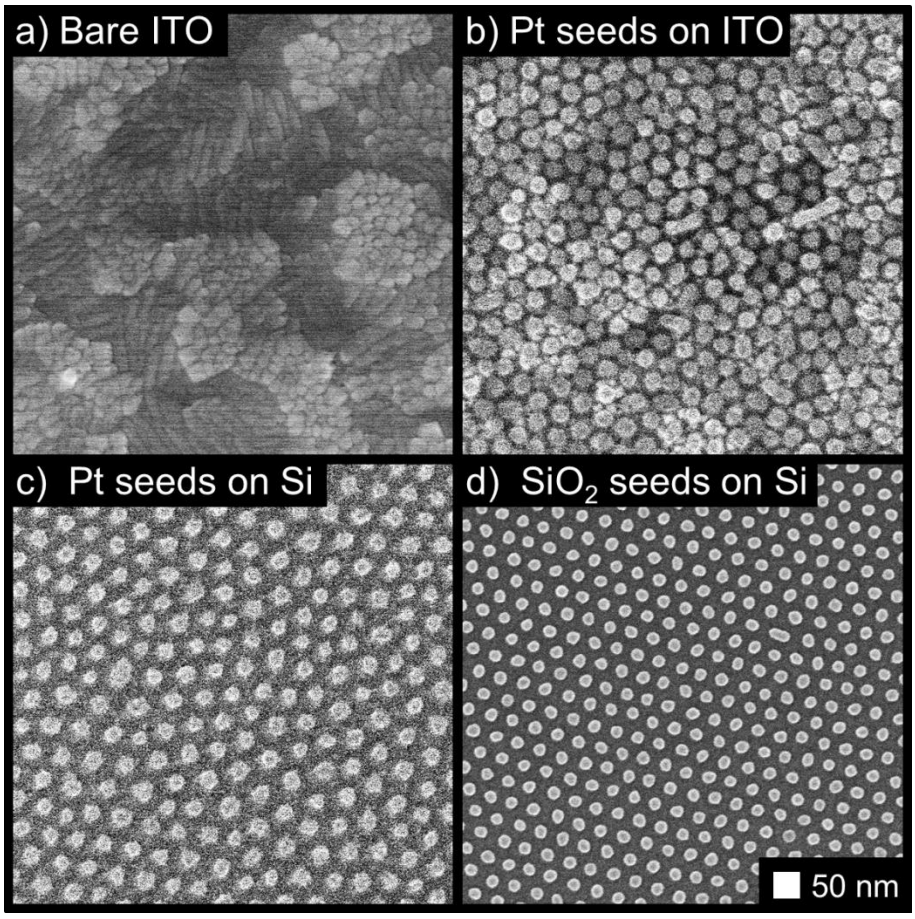

Figure 3.10 Pt seed patterns on ITO compared to Si, and Pt vs. SiO_2 seed patterns on Si.

to OPV device fabrication is shown in Figure 3.9. Here, a 50 nm thick GLAD ZnPc film was deposited on Si, seeded Si, ITO, and PEDOT:PSS. Again, a variety of morphologies are achieved, and the seeded substrate presents a perfectly ordered film in contrast with the disordered films on other substrates. This perfectly periodic columnar morphology is unlike any other achieved with these materials to date. The challenge, then, is to produce this ordered morphology in a way that is compatible with OPV device fabrication. So far, all the BCP-seeded MPc films have used Pt seeds on Si. For OPV device integration, a seeded anode material is required, for example ITO. In addition, an insulating seed material is desired to avoid interfering with the energy band structure of the device, shown in Figure 1.7. This way, charge

collection can occur as usual, with charges from the active layer flowing around the seeds to reach the anode.

The same seeding routine was performed on ITO as for Si, which is shown in Figure 3.10b. The pattern is similar to the one on Si, with slightly bigger seeds. In addition, a pattern of SiO_2 dots was created on Si, as seen in Figure 3.10d. Here, a polystyrene-*block*-polydimethylsiloxane (PS-*b*-PDMS) polymer was used instead of PS-*b*-P2VP. After the solvent vapor treatment, this film was immediately treated with a short CF_4 plasma at 100 mTorr and 50 W for 10 s followed by an oxygen plasma at 50 mTorr and 30 W for 30 s. Efforts towards achieving SiO_2 patterns on ITO and developing an ITO cleaning procedure that does not compromise the pattern are ongoing. These steps would enable integration into devices.

3.4. Summary

This chapter demonstrates the periodic arrangement of columnar small molecule thin films via glancing angle deposition on block copolymer seeded substrates. A variety of GLAD ZnPc films were grown on hexagonal seed patterns with 40 nm and 60 nm seed spacing, and the ϕ-sweep technique was used to maintain film uniformity and high column densities as the films grow. Control over the columnar dimensions and spacing enables an approach towards the ideal donor layer geometry for OPV devices. An SiO_2 seed pattern and a seeded ITO film were also shown to demonstrate the feasibility of device integration.

4. SOLVENT EFFECTS ON MPc FILMS[1]

4.1. Introduction

As mentioned in Chapter 1, various methods have been used to structure donor films for ideal OPV architectures [90,103,168,169,171–175]. In these cases, solution-based methods are often used to fill the donor film with an acceptor material. Understanding the solvent-film interactions during this processing is important. A certain degree of attraction between the donor film and the acceptor solution is necessary to enable filling the donor film at all, but a high solubility would wipe out the structural benefits being introduced. Solvent effects can even be exploited to encourage desirable donor layer morphologies, as shown in other studies that were done concurrently with those of this chapter [103,171–175].

The most common acceptor in small molecule devices is C_{60} – or the soluble form, PCBM – which is commonly dissolved in chlorobenzene (CB) or 1,2-dichlorobenzene (DCB) for film casting. Solvent choice and solution concentration have been shown to be critical factors for polymer OPV device performance [220–222] due to the variation in nanocrystalline domain sizes that occurs in each case. This warrants an investigation of the interaction between these organic solvents and MPc thin films used in small molecule OPV devices.

This chapter investigates the effects of CB, DCB, and other solvents on CuPc and ZnPc thin films. Most of the work involves direct application of the solvents to the films, in the absence of PCBM. This is done to identify the relative sensitivities of CuPc and ZnPc to these solvents, and to exaggerate the effects so that changes to the films' properties are detectable. Several factors related to solvent recrystallization of MPc films are evaluated, including solvent type, substrate type, exposure time, temperature during exposure, and the amount of material present in the original film. Various

[1]Portions of this chapter were reprinted from [177], Copyright (2011), with permission from Elsevier.

MPc film morphologies are used, many of which were GLAD films. For longer exposure times, films are recrystallized dramatically, with the final morphology bearing no resemblance to the original.

4.2. Experimental Details

Substrates used in this chapter were either (100) Si wafers (Evergreen Semiconductor Materials Inc.), ITO on glass (8-12 Ω/□, Delta Technologies), or ITO coated with a thin layer of PEDOT:PSS (Clevios P VP Al 4083). ITO was cleaned via sonication in IPA followed by exposure to oxygen plasma. PEDOT:PSS was applied undiluted, spun at 4000 rpm for 30 seconds, and baked at 80°C for 10 min in air.

CuPc and ZnPc were acquired from Sigma-Aldrich and were purified via thermal gradient sublimation at 400°C. All thin films were deposited at high vacuum ($< 2 \times 10^{-7}$ Torr) in a GLAD apparatus with a throw distance of 34 cm. Unless otherwise stated, films were grown by using a source temperature of 390 ~ 400°C resulting in a deposition rate of 0.7 Å/s at normal incidence. All GLAD films were preceded by a 10 nm planar layer grown at normal incidence immediately prior to GLAD deposition. All GLAD films described here are slanted post (SP) films made using the ϕ-sweep substrate motion technique described in Chapter 2. When using the ϕ-sweep technique, a substrate rotation angle of $\gamma = 30°$ was used, with one full sweep cycle per 4-5 nm of film growth, unless otherwise stated.

Solvent-treated films were achieved by either placing 4 drops (~ 200 μL) of solvent on the film surface from a glass pipet and either spinning the solvent off at 1000 rpm (spin treatment) or letting the solvent volatilize under ambient conditions (drop treatment), or by bathing the film sample in 5 mL of solvent in a glass petri dish for 10 minutes and then allowing the solvent to volatilize off the film under ambient conditions after removal from the bath (soak treatment). The drop and soak treatments resulted in very similar recrystallized film morphologies.

Images were acquired using a Hitachi S-4800 field emission SEM. Film

absorbance was calculated as the negative logarithm (base 10) of its transmittance spectrum, which was acquired using a Perkin Elmer Lambda 900 UV/VIS/NIR spectrophotometer.

XRD spectra were collected by Michael Fleischauer using a Bruker D8 diffractometer equipped with a Cu source and scintillometer using 1.0 mm antiscatter and 0.6 mm receiving slits. Diffractometer calibration and resolution was determined using a silver behenate reference standard. XRD peak fits were performed with gnuplot 4.4 using pseudo-Voight peak shapes and linear backgrounds between 5.5 and 8.1° scattering angle for patterns collected using theta / two theta geometry. Detector resolution was determined to be 0.21° FWHM; uncertainty in peak position was ± 0.04°.

For depth profiling, ZnPc films were coated with PCBM (American Dye Source). A 30 mg/ml solution in either CB or DCB (Sigma-Aldrich) was applied, and spun in air for 30 seconds at 1000 rpm. Depth profiling was performed via secondary ion mass spectrometry (SIMS), by alternating sputtering and analysis processes using a ToF SIMS IV instrument (ION-TOF GmbH). A chopped 25 keV Bi^+ ion beam with a current of 0.7 pA was used as the primary source to analyze an area of 40x40 μm^2, while O_2^+ was used as the sputtering source, operated at 1kV/55nA over a crater area of 200x200 μm^2.

4.3. Results and Discussion

4.3.1. Solvent effects on very thin MPc films

The most common MPc films used in OPV devices are very thin (~ 20 nm), with very little surface morphology. First experiments were therefore performed on these thin layers, which were grown on bare Si in order to isolate the solvent effects on MPc layers from effects on neighbouring layers (PEDOT:PSS for example). Spin treatments were performed, where the solvent was immediately spun off the substrate after application, to replicate device fabrication routines. A drop treatment was also done, which allows more time for film restructuring and is used to investigate the recrystallized film features that are possible through solvent exposure, similar to what has

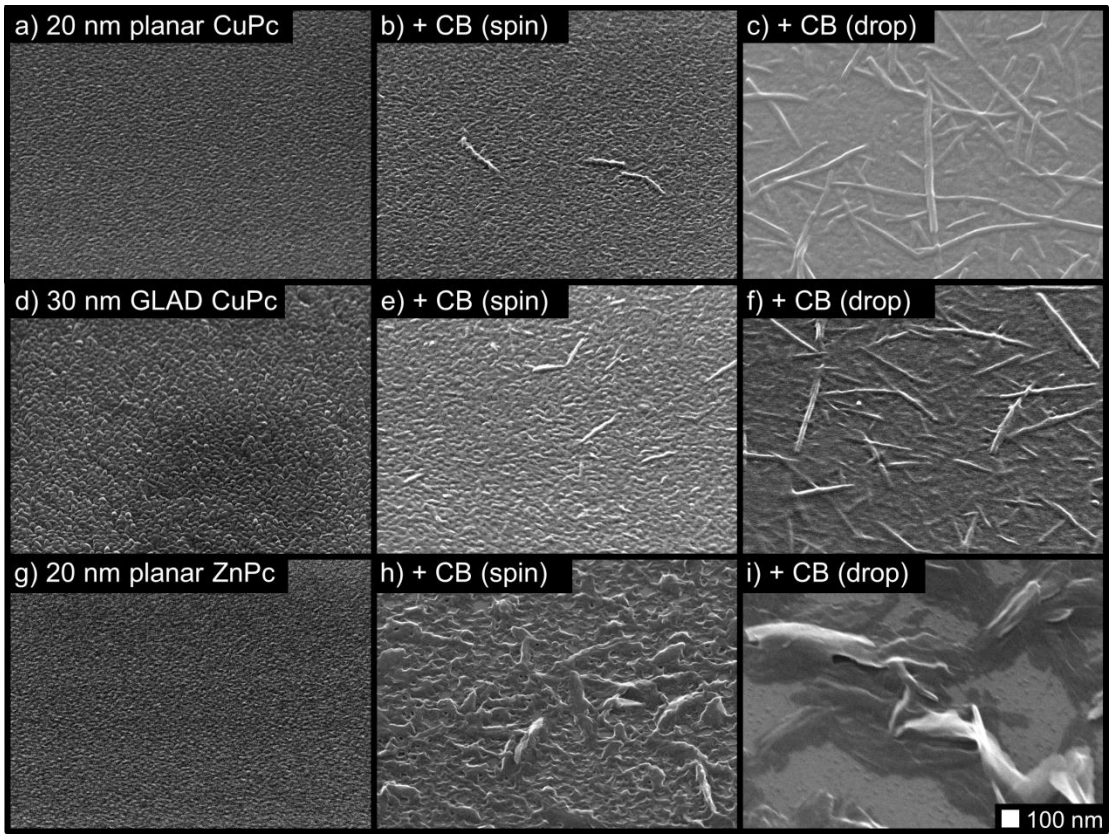

Figure 4.1 Effects of chlorobenzene exposure (short spin treatments, or long drop treatments) on thin planar and GLAD MPc films.

been done elsewhere [103,171–174]. Some examples of thin CuPc and ZnPc layers treated with chlorobenzene (CB) are shown in Figure 4.1. For CuPc, the brief spin treatments do very little, though a few small crystals were still able to form. During the extended exposure of the drop treatment, the crystals on the surface are able to grow much larger, and many more crystals are formed. The ZnPc film appeared much more sensitive to the solvent, with significant surface morphology changes occurring even with only the short spin treatment. For the drop treatment, the material is completely reorganized, with the bare Si surface being revealed in many areas and disordered residues lying elsewhere. Evidently, even the subtle change in the metal atom of the MPc molecule leads to substantial differences in the interaction between the film and the solvent. Interestingly, the CuPc material appears to form crystalline features as a result of solvent exposure, whereas the

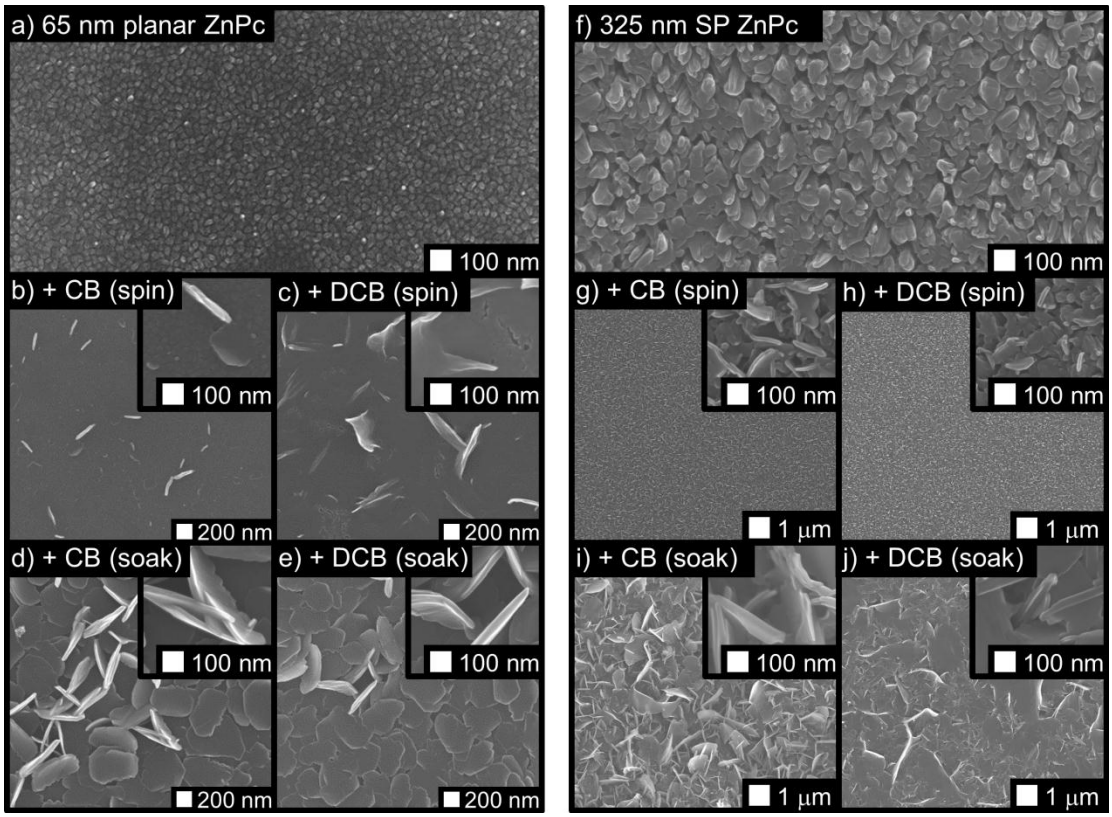

Figure 4.2 Effects of solvents (chlorobenzene and dichlorobenzene) on planar and GLAD ZnPc thin films. The "spin" and "soak" labels denoted short (seconds) and long (minutes) exposure times. Insets show a more magnified view of the recrystallized structures. All these film are on Si substrates.

restructured ZnPc material is quite irregular. It is significant to note that even with very brief exposure, the film structure can be modified substantially, particularly for ZnPc.

4.3.2. Changes to film properties as a result of solvent exposure

Though structural modifications are easy to identify in very thin films, changes to the film properties due to solvent treatments are hard to detect. Thicker films are used in this section to investigate changes to film crystallinity and absorbance. A 65 nm planar ZnPc film and a 325 nm slanted post (SP) GLAD ZnPc film, both grown on bare Si, are used here (see Figure

4.2). The GLAD film was grown at $\alpha = 60°$, without ϕ-sweep substrate motion. Spin and soak treatments using CB and DCB solvents were performed on these films; the resulting morphologies can be seen in Figure 4.2. The films exhibited a significant degree of recrystallization as a result of these solvent exposures, with each combination of solvent treatment and ZnPc film morphology yielding a unique recrystallized morphology. The planar film surface can be roughened even with very short solvent exposure times, as seen in Figure 4.2b and 4.2c. In this case, DCB appears to have a stronger effect, suggesting that solvent choice may be a critical factor under device fabrication conditions. A greater degree of recrystallization occurs for longer exposure times, which leads to platelet formations (Figure 4.2d and 4.2e). These were not apparent in the very thin films shown in the previous section, likely due to an insufficient amount of material in the original film. Interestingly, the platelet thicknesses closely match the exciton diffusion length of ZnPc (15nm [72]), which would provide strong exciton dissociation efficiency if the platelets were used in a donor-acceptor heterojunction. An ordered arrangement of such structures could be expected to perform well in photovoltaic devices. However, changes to the film properties were evident after the solvent exposure, from both a crystallinity and absorbance perspective, which makes their potential usefulness in an OPV device questionable. The solvent-treated GLAD films also showed substantial restructuring (see Figure 4.2g-j), and corresponding changes to the film crystallinity and absorbance were observed.

The XRD data in Figure 4.3 shows the ZnPc films' crystallinity changes due to the solvent treatment. In all cases, the most prominent observed peak was α (010), centered at ca. 6.82° scattering angle, consistent with what has been observed previously for MPc films [41]. The α (010) peak intensity is enhanced by the solvent treatment for the planar film, but decreases significantly for the SP film. In both cases, the DCB-treated film showed a higher α (010) peak than the CB-treated film. Interestingly, the α (001) peak, centered at ca. 7.37° scattering angle, became much stronger in the SP film upon solvent treatment with DCB.

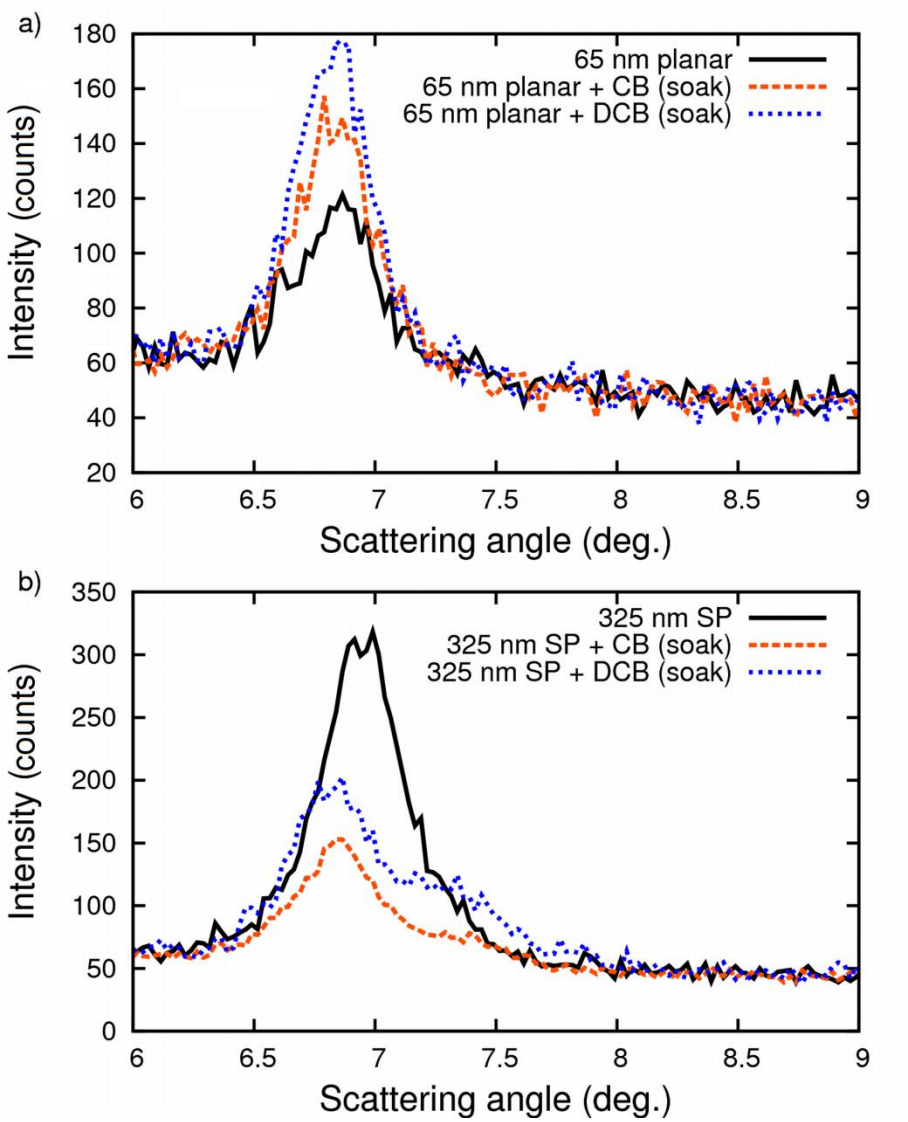

Figure 4.3 Effects of solvent exposure on the XRD spectra of ZnPc thin films.

The absorbance profiles shown in Figure 4.4 also reveal significant changes in the film as a result of solvent exposure. Spin treatments did not affect absorbance significantly, except for DCB on a planar film where a new peak is observed in the 850 nm region. For the soak treatments, significant changes to the Q band (500 ~ 800 nm) were seen, suggesting changes in film composition in addition to the morphological changes. The photovoltaic properties of some of these solvent textured films are investigated in Chapter 5. For now, it is significant enough to note that ZnPc films respond differently

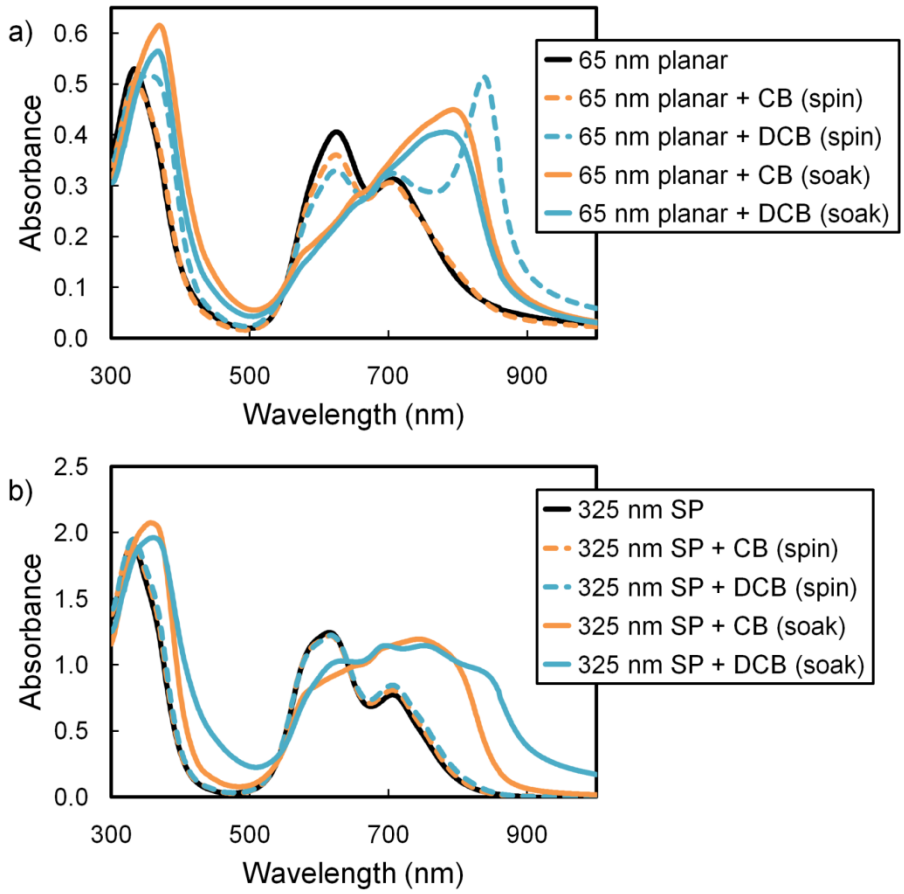

Figure 4.4 Effects of solvent exposure on the absorbance of ZnPc thin films.

to these two solvents, while being sensitive to both. To confirm that these solvent effects are due to dissolution, the residual solvent from the soak treatments were examined to identify dissolved material. Quantifying the solubility of ZnPc in CB and DCB is the topic of the next section.

4.3.3. Solubility studies on ZnPc

The solvents from the baths used to soak-treat ZnPc films were recovered and their absorbance was measured to identify dissolved material, as shown in Figure 4.5. The absorbance of pure CB and DCB was used as the reference in each case. Modest peaks in the 600 ~ 700 nm range are observed, which resemble those seen previously for ZnPc in other solvents [223,224] and for other MPc's in solution [225–227]. These profiles are characteristic of

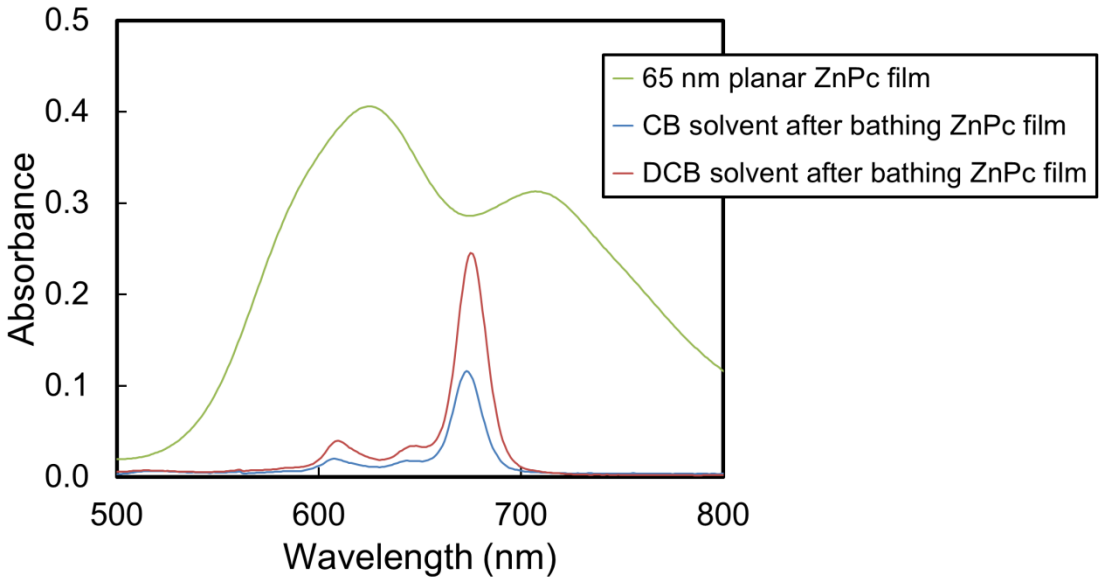

Figure 4.5 Absorbance of a ZnPc thin film compared to ZnPc dissolved in CB and DCB.

monomolecular phthalocyanine in solution [226]. Modest solubility of MPc molecules has also been documented elsewhere [173,228]. The absorbance profiles shown in Figure 4.5 were observed regardless of the original ZnPc film morphology or substrate used in the soak treatment. The data shown is from soak-treating a film on glass with an area of ~ 4.25 cm^2 and was obtained using a standard 1 cm cuvette. Whalley determined the extinction coefficient (ε) of ZnPc in pyridine to be $10^{5.45}$ $M^{-1}cm^{-1}$ at 672 nm [229]. Based on the peak heights of 0.12 and 0.25 for CB and DCB, respectively, this translates into concentrations of 0.2 and 0.5 μg/mL. Though not significant enough to enable solution casting of these materials, it certainly enables the recrystallization effects that these solvents have on ZnPc films.

4.3.4. Solvent effects on device-relevant films and substrates

So far, all MPc films exposed to solvent treatments were deposited on Si. Solvent effects on these films appear to be determined by the solvent type, exposure time, and amount of original material in the film. When considering MPc films deposited during device fabrication, the presence of other

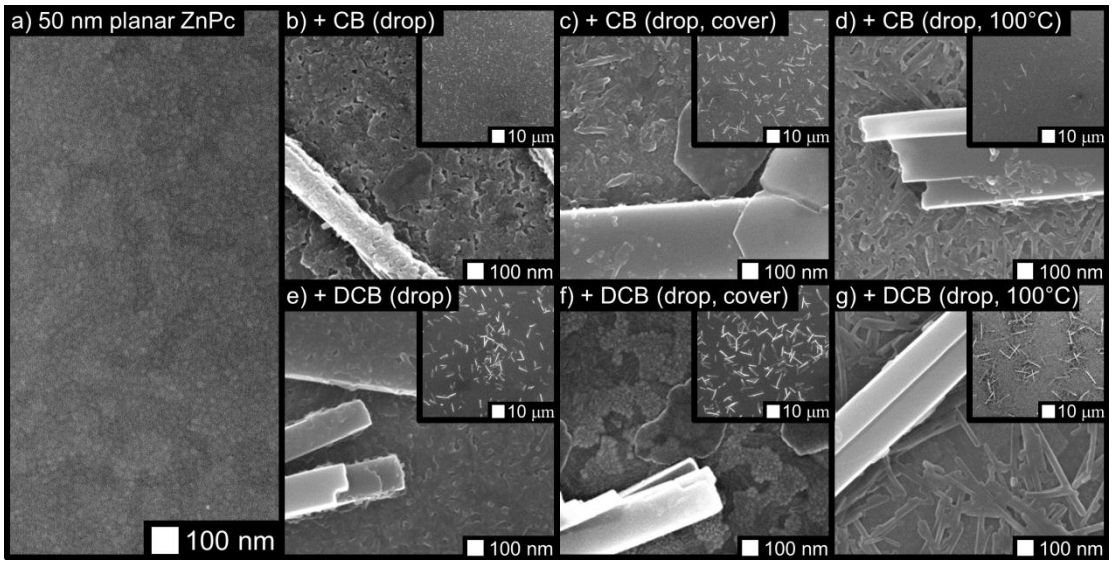

Figure 4.6 Effects of various solvent annealing conditions on a planar ZnPc film (on bare ITO). Insets contain less magnified views of the recrystallized films, which show the spatial density of recrystallized features.

materials comes into play. Specifically, a thin layer of PEDOT:PSS lies underneath the MPc layer; if exposed and dissolved by the solvent, it could affect the recrystallization process and the composition of the residual film. Additionally, even in the absence of PEDOT:PSS, a bare ITO surface may affect the film recrystallization process differently than Si. In the context of OPV device fabrication, the exposure time to the solvent is very short and the PCBM solution is nearly saturated, making the solvent less aggressive on the films. Therefore, the presence of underlying PEDOT:PSS and ITO would likely not have any consequences. Nevertheless, it is still worth investigating for the purpose of creating different recrystallized MPc morphologies.

Shown in Figure 4.6 is a 50 nm planar ZnPc film, along with several recrystallized versions of this film achieved with solvent treatments. Indeed, the final morphology of these films is quite different than those seen on the Si substrate. Here, the film forms rectangular crystals instead of the circular platelets observed previously (Figure 4.2d and 4.2e). The exposure time was further controlled in this set of films by means of covering and heating the samples during exposure. The covered samples had longer exposure because

the evaporated solvent remained in close proximity to the sample surface, decreasing the evaporation rate. It is clear that these longer exposures led to more significant recrystallization, and higher concentrations of crystallites (Figure 4.6c and 4.6f). A mix of both rectangular and platelet crystallites are present in these films. Again, DCB appears to be the more aggressive solvent as it was able to etch the film off the ITO surface completely, revealing a bare surface scattered with crystallites (Figure 4.6f). The heated samples had shorter exposure times due to increased evaporation rates. Compared to the covered samples, a lesser degree of recrystallization could be expected. Indeed, the populations of larger crystals are below that of the covered samples. However, the samples exposed at 100°C are comparable to the ones at room temperature, at least when comparing the spatial density of larger crystals. The difference here is that the higher temperature enabled more rapid and complete dissolution of the film, as evidenced by the strong presence of nanocrystalline material (Figure 4.6d and 4.6g). Thus, the material that did not organize into large crystallites formed small ones instead, unlike the samples at room temperature where the residual film appears to have been undissolved and is left somewhat perforated (Figure 4.6b and 4.6e). Though none of these films stand out as good candidates for OPV devices, the fact that heat and exposure time can be used to influence the interaction between solvents and MPc films is important to recognize. It is significant to note that in all cases the DCB-treated films exhibited a greater degree of recrystallization with a higher number of crystallites, which is consistent with the higher solubility value calculated in the previous section.

Similar to polymer OPV devices, many MPc-based devices utilize a PEDOT:PSS hole transport layer between the ITO and MPc layer, which may further influence solvent-induced film recrystallization. Some examples of recrystallized planar and GLAD ZnPc films on PEDOT:PSS are shown in Figure 4.7. A drop treatment was performed in both these experiments. Again, there are substantial morphological changes to the films; the final morphologies bear no resemblance to their originals, but are quite similar to each other. These platelet formations are akin to those seen previously for a

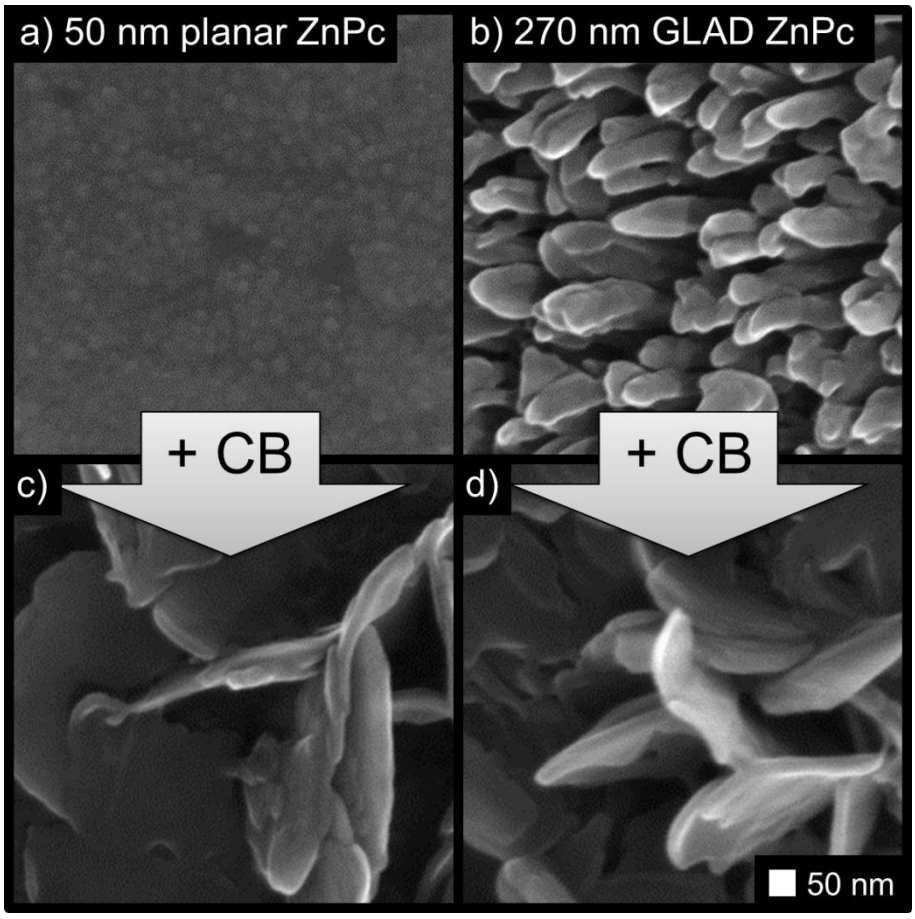

Figure 4.7 Planar (a) and GLAD (b) ZnPc thin films on PEDOT:PSS coated ITO, and the recrystallized films after extended chlorobenzene exposure.

planar ZnPc film on Si (Figure 4.2d and 4.2e). A shorter GLAD film on PEDOT:PSS is shown in Figure 4.8, along with its solvent-treated versions (drop treatment). In the CB case, a mix of rectangular and platelet structures

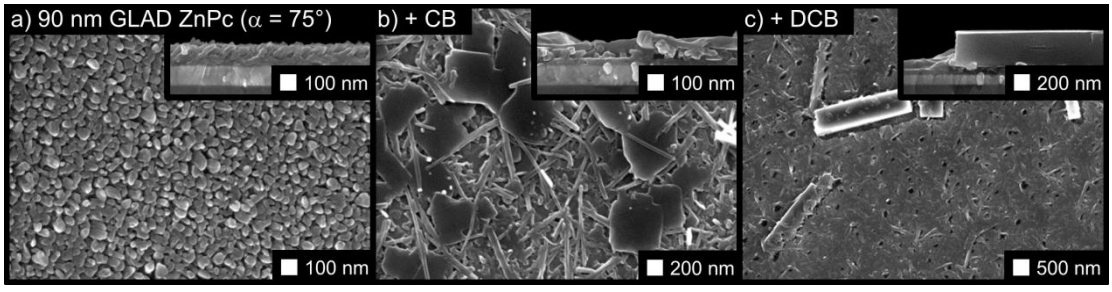

Figure 4.8 Effects of extended exposure to chlorobenzene and dichlorobenzene on a thin GLAD ZnPc film (on PEDOT:PSS coated ITO).

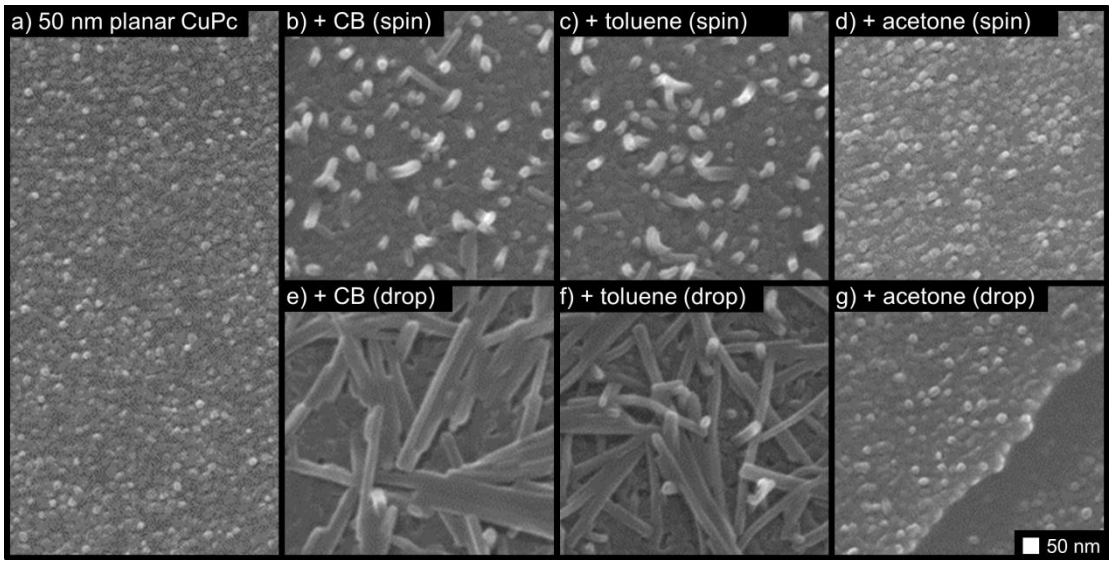

Figure 4.9 Effects of various solvents and exposure times on a planar CuPc thin film grown on PEDOT:PSS coated ITO.

are formed, whereas DCB exposure leads to the formation of very large box structures. Similar variations of these platelet and box structures have been prepared before, albeit with radically different conditions [224]. Again, neither of these recrystallized films are appealing from an OPV device perspective, but the difference between the interactions of these two solvents with ZnPc films is noteworthy.

Previous studies on solvent exposure of planar CuPc films have been able to take advantage of recrystallized film morphologies to improve device performance [172,173]. Attempts at reproducing these films are shown in Figure 4.9, and though the film morphologies are indeed very similar to published ones, improvements in device performance due to recrystallization were never observed. In fact, solvent treatments decreased device performance in all cases, which is discussed further in the following chapter. Because much of this thesis is focused on nanostructured donor layers, the effects of solvent exposure on GLAD-structured MPc films are also of great interest. Some examples of solvent-treated GLAD CuPc are shown in Figure 4.10 (α = 80°) and Figure 4.11 (α = 85°), where short (spin) and long (drop) exposure times are performed. The film deposited at α = 85° appeared to be

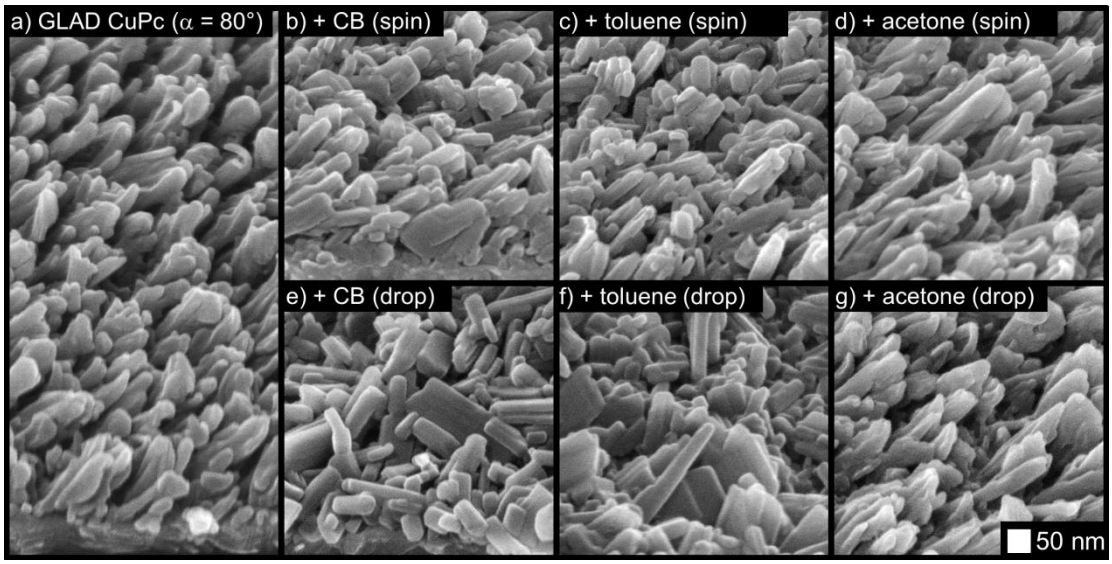

Figure 4.10 Effects of various solvents and exposure times on a GLAD CuPc thin film (slanted post profile, α = 80°) grown on PEDOT:PSS coated ITO.

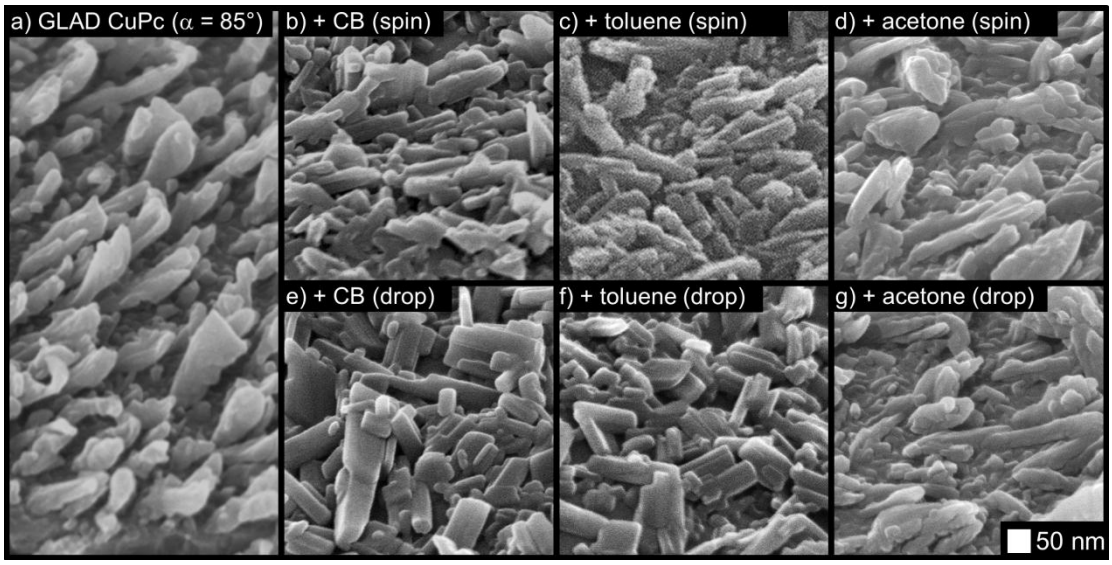

Figure 4.11 Effects of various solvents and exposure times on a GLAD CuPc thin film (slanted post profile, α = 85°) grown on PEDOT:PSS coated ITO.

much more vulnerable to solvent exposure; the original columnar morphology is flattened out in call cases, leaving only disordered heaps of nanocrystals detached from the substrate. The film deposited at α = 80° was able to withstand the solvent exposure a bit better. The spin treatments left

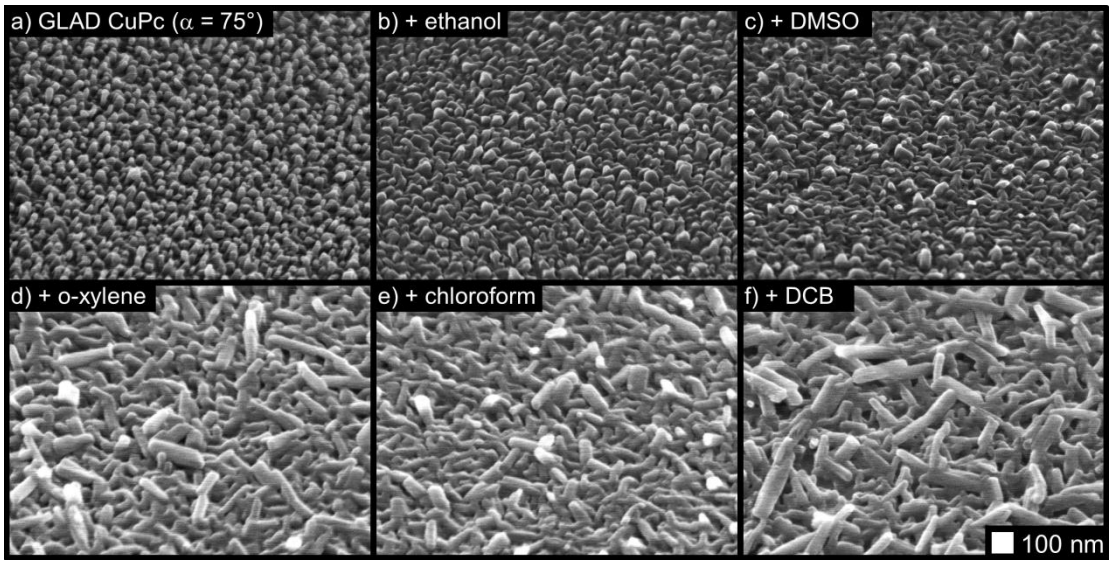

Figure 4.12 Effects of various solvents on a GLAD CuPc thin film (α = 75°) grown on PEDOT:PSS coated ITO.

the film with only marginal modifications, and the original orientation of columnar features remains. The drop treatment, however, left the film completely reorganized and detached from the substrate in most cases. The acetone treatment is the exception; here the original orientation and slanted post morphology are largely unaffected (Figure 4.10g). The acetone treatment was found previously to be most useful for creating columnar film morphologies from planar ones, but is unfortunately unable to improve the morphology of GLAD films, leaving it of little use. All in all, the exposure of GLAD CuPc films to these solvents appears to be detrimental to their columnar morphologies, which raises concerns over the survivability of these films in OPV device fabrication. Using a different PCBM solvent may solve the issue, but the solvents that are least destructive to CuPc and ZnPc films are also least able to dissolve PCBM.

Solvent treatments were performed on a GLAD CuPc film using several other solvents, which are shown in Figure 4.12. In most cases the film loses its original morphology, but ethanol and DMSO are least aggressive. Unfortunately, these solvents are unable to dissolve an adequate amount of PCBM to enable spin casting. Therefore, concerns remain over constructing

an ordered active layer structure using solution filling of GLAD MPc films. These concerns are addressed further in the following chapter. As a preliminary note, PCBM-concentrated solutions make the solvents less able to act on the MPc layer, which provides some optimism. The degree of dissolution and material mixing between planar ZnPc and PCBM is analyzed via ToF-SIMS depth profiling in the following section.

4.3.5. Active layer analysis of PCBM-coated planar ZnPc films

Most of this chapter has dealt with direct contact of pure solvents with MPc films. This was done to identify the relative sensitivities of MPc films to different solvents, as well as to pursue enhanced morphologies that may be possible via solvent-induced recrystallization. However, direct contact between pure solvents and MPc films is rarely encountered in a device fabrication context. Much more relevant is the study of interactions between MPc layers and PCBM solutions in different solvents, which has not been studied before. This focus narrows down the list of possible solvents significantly. The following study focuses on a simple comparison between CB and DCB.

The compositions of bilayer ZnPc/PCBM active layers made by spin-casting PCBM onto planar ZnPc, using either CB or DCB as the PCBM solvent, are of great interest. The layer architecture studied here is as follows: glass / ITO (120 nm) / PEDOT:PSS (30 nm) / ZnPc (20 nm) / PCBM (40 nm). Depth profiles of these multilayer films were acquired via secondary ion mass spectrometry (SIMS), and are shown in Figure 4.13. The ZnPc layer can be identified by the presence of Zn, whereas C is found in both components of the active layer and therefore does not distinguish between them. In the CB case, Zn is well-confined to a particular region within the layer stack, and is only observed far beneath the surface. The results are substantially different when using DCB as the PCBM solvent, where Zn is not only broadly distributed throughout the active layer, but even very present at the surface. This suggests that the active layer becomes more of a mixed heterojunction rather than a bilayer. The mixing that occurs between layers when using DCB

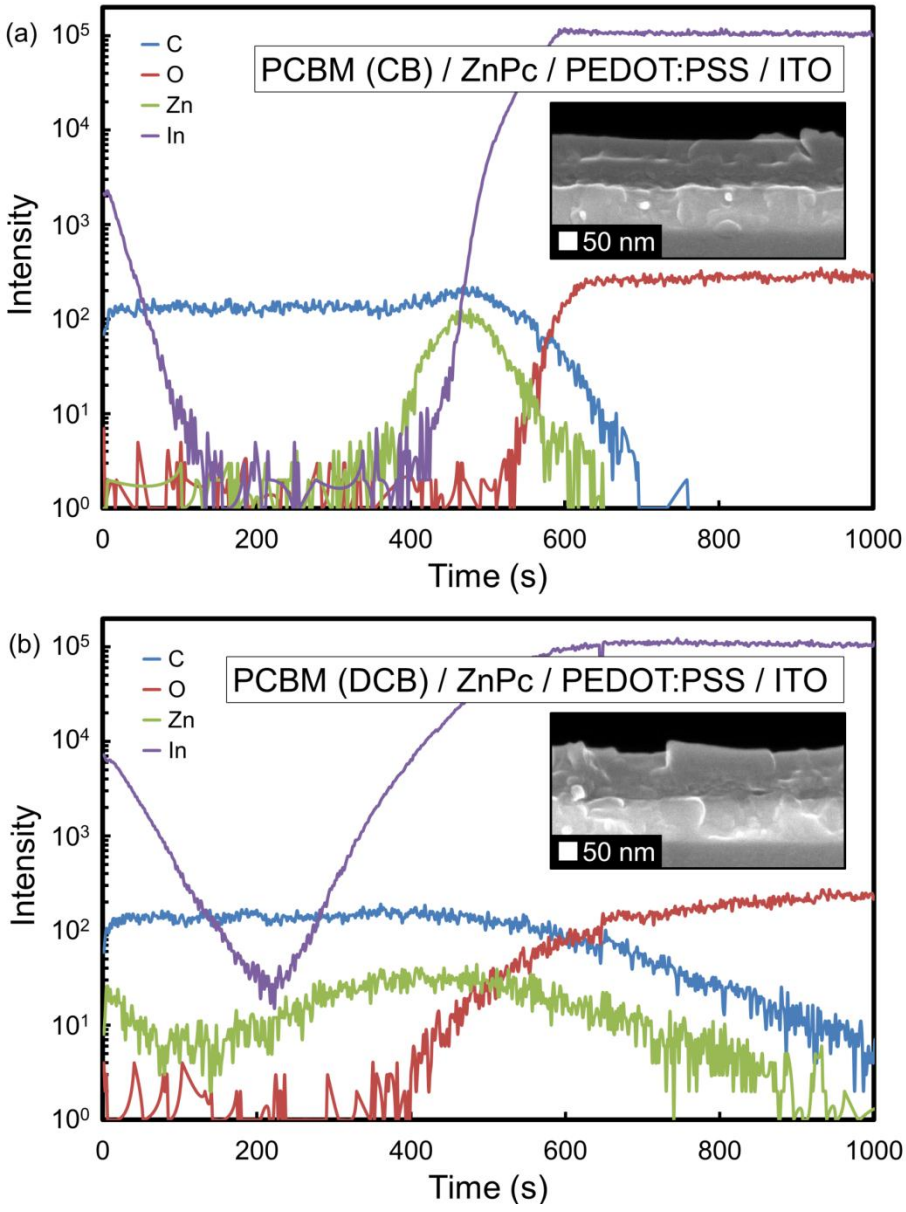

Figure 4.13 SIMS depth profiles for thin bilayer ZnPc/PCBM OPV devices, without top electrodes, using (a) CB and (b) DCB as the PCBM solvent.

as the PCBM solvent provides a strong explanation for the differences in device performance between using different solvents, which is further discussed in the following chapter.

Finally, it is surprising to see that in each case a significant amount of indium is also present at the surface. Indium migration has been observed in organic optoelectronic devices previously [34,230,231], and may provide an explanation for the morphological differences between solvent-treated ZnPc films on Si vs. ITO (Figure 4.2 vs. Figure 4.6).

4.4. Summary

This chapter contains several investigations on the effects of organic solvents on thin MPc films of various morphologies. These MPc films show considerable sensitivity to these solvents; in most cases the films are completely restructured upon evaporation of the solvent. The final morphology of these films is related to the type of solvent used, the exposure time, the temperature during exposure, the original film thickness, and the substrate underlying the MPc film. A variety of recrystallized film morphologies are achieved, most of which exhibit rectangular crystals, circular platelet structures, or a mix of these. The severity of these solvent effects raises concerns over the survivability of GLAD MPc films in OPV device processing, which are addressed further in the following chapter. The final observation from this chapter is that the degree of material mixing in a bilayer ZnPc/PCBM OPV device layout depends strongly on the PCBM solvent used. This is used in the following chapter to optimize the active layer, and consequently device performance.

5. OPV DEVICE OPTIMIZATION[1]

This chapter investigates various factors affecting small molecule OPV device performance and degradation. Fabrication and testing routines are standardized to ensure consistent, reliable results. The chapter concludes with an optimized active layer achieved by introducing nanostructured ZnPc and promoting donor-acceptor material mixing, as illustrated in Figure 5.1.

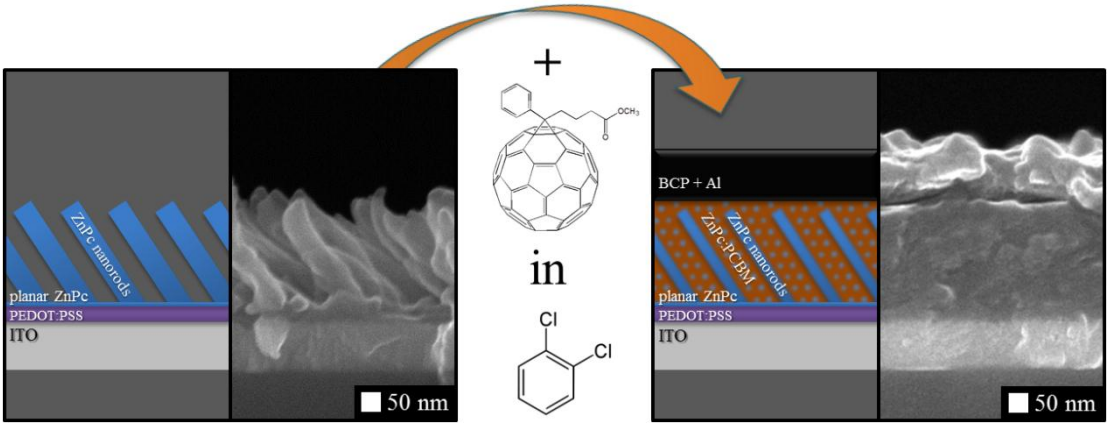

Figure 5.1 Illustration of nanostructured OPV device fabrication.

5.1. Introduction

Optimizing the active layer architecture of small molecule OPV device is a topic of great interest [73,86,97,100,103,168,169,171–174,190,191,194]. Identifying improvements due to changes in the active layer can be challenging, as it requires a thorough understanding of all the factors affecting device performance. The importance of consistent processing conditions has been emphasized elsewhere [232]. Even subtle differences in processing conditions can adversely affect results, or, in some cases, provide unexpected improvements [233].

A properly functioning OPV device requires the integration and

[1]Portions of this chapter were reprinted from [177], Copyright (2011), with permission from Elsevier.

optimization of several material layers. Making improvements to the active layer requires an established comparison: a bilayer device which can be routinely fabricated to provide consistent, reliable results. Organic materials are often sensitive to ambient environments, particularly to oxygen, humidity, and UV radiation. Exposure to these can lead to rapid degradation of materials, films, and their properties, making it difficult to achieve consistent, reliable results. From a commercial perspective, encapsulation is relied upon to provide protection from the elements, which is becoming an increasingly popular area of research [36]. This extra processing is impractical on a small scale in research laboratories, where an understanding of the relative vulnerabilities of the materials and their films, along with appropriate care during processing, is sufficient to innovate in other areas to improve performance.

Material quality, film aging, and film thickness all play important roles in the operation of OPV devices. Many studies have been done on the degradation of small molecule devices [35,36,39]. Much of this chapter investigates the relative sensitivities of the device materials chosen in Chapter 1 (and shown in Figure 1.7). The PEDOT:PSS and MPc films are found to be least sensitive to ambient exposure, whereas PCBM degrades very rapidly, which lays a sense of urgency on all the fabrication processes that follow the PCBM deposition. Section 5.5.4 then discusses the role that solvent effects (discussed in Chapter 4) play in the construction of the active layer, and uses this in combination with nanostructuring (discussed in Chapter 2) to optimize the active layer of ZnPc/PCBM OPV devices. Optimal device performance is achieved with a 30 nm thick GLAD-textured ZnPc film while using DCB as the PCBM solvent. In this case, power conversion efficiencies are up to 3.0%, compared to an average of 2.3% when using CB as the solvent on the same film, and 2.3% also for bilayer devices when using DCB as the solvent. The higher degree of material mixing at the ZnPc/PCBM interface, discussed at the end of the previous chapter, may be the primary mechanism for the photovoltaic improvements seen in these devices.

5.2. Experimental Details

5.2.1. MPc thin film deposition and characterization

CuPc and ZnPc were acquired from Sigma-Aldrich and were purified at least twice for all devices in section 5.5.4, via thermal gradient sublimation at 400°C. All CuPc and ZnPc thin films were deposited at high vacuum (< 2×10^{-7} Torr) in a GLAD apparatus with a throw distance of 34 cm. Unless otherwise stated, films were grown by using a source temperature of 390 ~ 400°C resulting in a deposition rate of 0.7 Å/s at normal incidence. All GLAD films were preceded by a 10 nm planar layer grown at normal incidence immediately prior to GLAD deposition, to prevent any direct contact between the anode and the acceptor. All GLAD films described here are slanted post (SP) films made using the ϕ-sweep substrate motion technique described in Chapter 2. Unless otherwise stated, the ϕ-sweep parameters were $\gamma = 30°$, with one full sweep cycle occurring during every 4-5 nm of film growth.

Solvent-treated films were achieved by placing 4 drops (~ 200 μL) of solvent on the film from a glass pipet and allowing the solvent to volatilize off the film under ambient conditions (the drop treatment from Chapter 4).

Images were acquired using a Hitachi S-4800 field emission SEM. UV/Vis absorbance data was acquired using a Perkin Elmer Lambda 900 UV/VIS/NIR spectrophotometer. Absorbance was calculated as the negative logarithm (base 10) of the transmittance spectrum.

5.2.2. OPV device fabrication and characterization

OPV devices were fabricated on anodes of ITO on glass (8-12 Ω/□, Delta Technologies), coated with a thin layer of PEDOT:PSS (Clevios P VP Al 4083). ITO was cleaned via sonication in IPA followed by an oxygen plasma etch. PEDOT:PSS was applied undiluted, spun at 4000 rpm for 30 seconds, and baked at 80°C for 10 min in air. Following ZnPc deposition, PCBM (American Dye Source) was applied at 30 mg/ml in either CB or DCB (Sigma-Aldrich), and spun in air for 30 seconds at 1000 rpm. The top electrode,

consisting of 15 nm bathocuproine (BCP, Sigma-Aldrich) and 80 ~ 100 nm Al (Lesker), was deposited through a shadow mask over 5 rectangular device areas of 0.20 cm^2 each, in a glovebox evaporator. BCP was purified in the glovebox evaporator by holding the crucible for half an hour at a temperature just below the sublimation point of BCP. These standard fabrication routines apply primarily to devices presented in section 5.5.4. Elsewhere, the fabrication routines would similar.

Current-voltage characteristics of OPV devices were taken in air using a Keithley 2400 source meter, under AM 1.5 G simulated irradiation (Oriel 91191 1000W). For the devices in section 5.5.4, light intensity was calibrated against a KG5 filtered Si reference cell (PV Measurements, Inc., model PVM624). Device performance numbers are usually reported as averages over several (at least 5 ~ 10) devices. Uncertainties were calculated as the standard deviation of each data set. A custom setup was used to measure the external quantum efficiency (EQE) of some of the key devices in section 5.5.4. Here, the test wavelength was controlled with a 0.25 m Czerny-Turner spectrometer (Oriel MS 260i), using a 150 W Xe lamp (Oriel Photomax 60100 housing a Oriel 6256 bulb) as the source. The incident power on the device was monitored during testing using a traceable optical power meter (Gentec-EO, PH100-Si), calibrated for target plane power. Device current was measured using a Keithley 2400 source meter.

5.3. Bilayer Device

To provide context, an example of a bilayer OPV device is shown in Figure 5.2, and its current-voltage curves are shown in Figure 5.3. The device exhibits the following performance parameters: J_{sc} = 3.70 ± 0.15 mA/cm^2, V_{oc} = 0.61 ± 0.01 V, FF = 0.57 ± 0.03, and η = 1.36 ± 0.08%. The layer structure, beginning at the bottom, is glass / ITO (120 nm) / PEDOT:PSS (30 nm) / CuPc (20 nm) / PCBM (40 nm) / BCP (15 nm) / Al (100 nm). This architecture has been studied elsewhere with very similar results [158,172,173,191], though it varies slightly from the archetypal CuPc-based architecture [86] by using

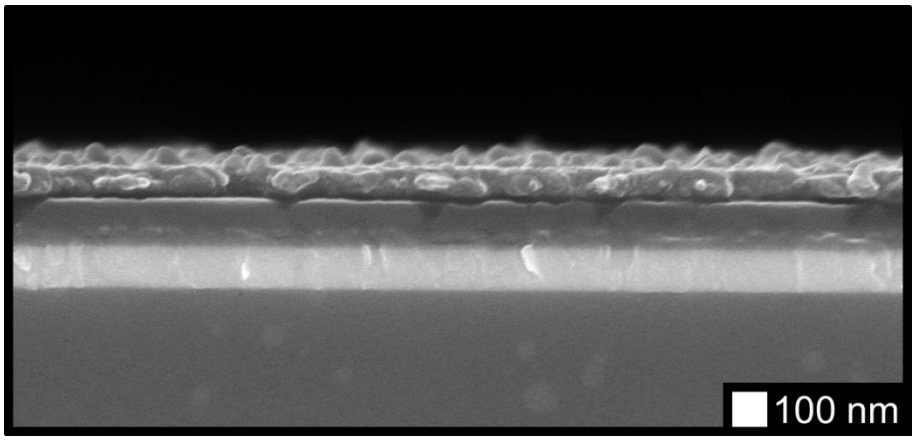

Figure 5.2 Cross-sectional SEM image of a bilayer CuPc/PCBM OPV device.

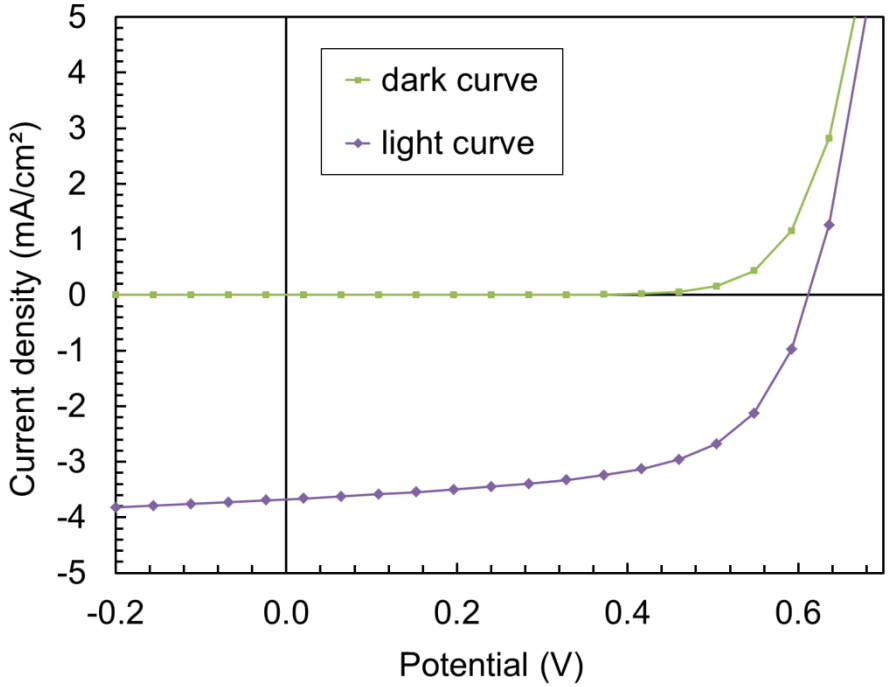

Figure 5.3 Current voltage behavior of a bilayer CuPc/PCBM OPV device.

PCBM instead of C_{60} and including a layer of PEDOT:PSS. This represents the benchmark upon which improvements due to structuring can be made. In the absence of completely inert fabrication environments, significant effort is required to achieve consistent results. Most of the sections within this chapter are aimed at identifying the relative sensitivity of different processing steps and conditions, so that the most critical ones can be controlled.

5.4. Testing, Calibration, and Reporting of Results

The rapid rise in OPV device efficiencies is the result of a highly competitive race to report record results. Within this race, concerns have arisen over testing accuracy, which has motivated the development of OPV-specific testing standards [234]. Currently, record results must be independently certified, usually by Dr. Emery at the National Renewable Energy Laboratory (NREL) in Colorado, whose solar simulator provides unparalleled spectral matching capabilities. Most of the progress within the OPV field can proceed without such scrupulous testing, because relative performance can be evaluated using more commonly available equipment.

Spectral calibration is not unique to OPV testing, of course. The output intensity of solar simulators is known to vary substantially over time, depending on the age and temperature of the bulb, which warrants frequent calibration regardless of sample type. However, the difficulty with OPV device testing arises from the narrow absorption spectrum of most organic materials. Because solar simulators are rated by the average power they deliver over different wavelength ranges, results can vary substantially between simulators depending on the shape of their spectrum over the OPV-relevant range. A spectrum that over-emphasizes the 400 ~ 700 nm region will overestimate device efficiencies, and any spectral deficiencies in this region will lead to underestimated values.

The standard calibration technique for OPV testing in most labs is to use a KG5 filter to ensure that the power within the 300 ~ 800 nm wavelength range matches well with the AM 1.5 G solar standard [234]. To illustrate the importance of this standard, Figure 5.4 shows changes in device behavior due to changes in the spectrum. Changes in J_{sc} and η were dramatic, while the V_{oc} and FF remained remarkably consistent, regardless of the spectrum. Here, colored glass filters (2'' by 2'', 2 mm thickness, Schott Glass) were used to isolate different regions of the spectrum during testing. The incident power in each case was monitored by a power meter and used to calculate efficiency. The relative efficiency values are therefore an indication of how well the

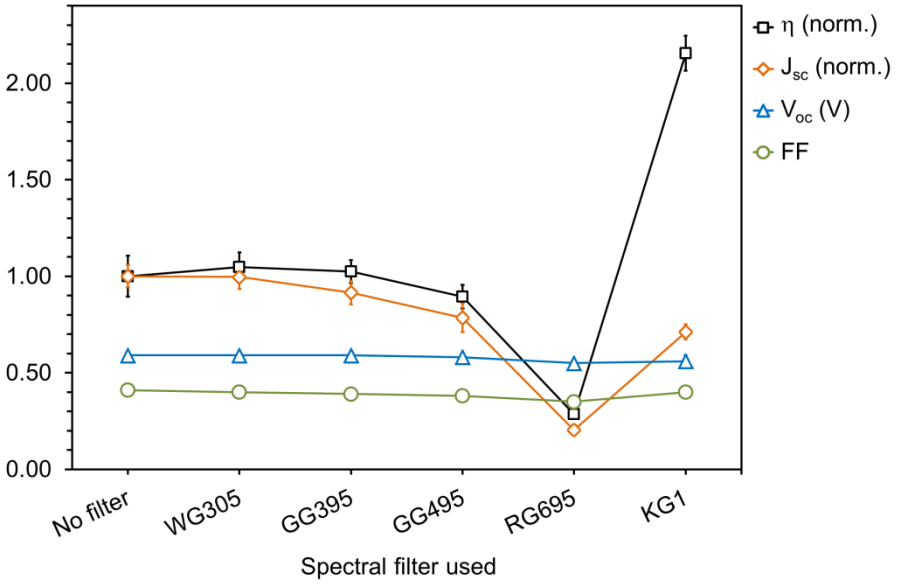

Figure 5.4 Effects of spectral changes on device response. Aside from the KG1, all filters were high-pass filters with a cut-off wavelength corresponding with the number in the filter name (e.g. WG305 transmits wavelengths of 305 nm or above). The KG1 transmits between 300 ~ 800 nm only, similar to a KG5 filter.

filtered spectrum is absorbed and converted by the devices. The filters were mostly high-pass filters, with the cut-off wavelength denoted in the filter name. For example, the WG305 filter transmits everything above 305 nm, the GG395 filter transmits everything above 395 nm, and so on. The exception is the KG1 filter, which is a band-pass filter that transmits light in the 300 ~ 800 nm region, similar to a KG5. The efficiency is much higher in this case, because the KG1 filter aligns so well with the devices' absorption. Further analysis on the simulator spectrum revealed severe deficiencies in the visible region relative to the infrared. Therefore the infrared output of the simulator was high after calibrating the spectrum with a KG5-filtered Si reference cell, but with no consequence on results since devices do not absorb in this region.

For the optimization experiments that follow, device testing was performed prior to establishing the KG5 calibration routine. In these cases, the output of the solar simulator was found to vary substantially. As a result, J_{sc} and η were highly variable between device batches, and are therefore

reported as normalized values in sections 5.5.1 through 5.5.3. As shown above, V_{oc} and FF are hardly affected by changes to the incident spectrum, and are therefore reported as absolute values. The KG5-filtered calibration routine was later employed to enable accurate reporting of absolute values for all performance parameters, which applies to the devices in section 5.5.4.

Rapid degradation of OPV devices makes testing somewhat more challenging. Testing in inert environments is common, and has been shown to improve the FF by up to 40% [107,235]. However, testing in air is far more practical, and is done by many groups reporting record results. In the absence of fully inert processing and testing equipment, the experiments in section 5.5.1 focus on identifying the critical stages that are sensitive to ambient exposure, and appropriate care is taken thereafter to minimize degradation prior to testing.

5.5. Results and Discussion

5.5.1. Material quality and film sensitivity

As mentioned earlier, many organic materials and films are sensitive to ambient environments. Therefore, a firm understanding of the relative degradation speed of each of these layers is critical. A tight process flow that leaves little time between each deposition is preferred, but is not always practical, and is also, as it turns out, unnecessary. This section analyses the degradation behavior of each of the organic layers, as well as the materials and solutions used to deposit these layers.

To begin, a series of devices are made with fresh and aged PEDOT:PSS films. Aged films were placed in a cabinet with exposure to air and varying amounts of indoor lighting. Aging varies between only several hours to over 1 month. Additional layers were deposited simultaneously for all devices and were tested immediately afterwards, the results of which are presented in Figure 5.5. Surprisingly, performance seems to improve slightly as a result of small amounts of aging, but is within error of original values. The PEDOT:PSS layer therefore appears to be fairly robust, with performance

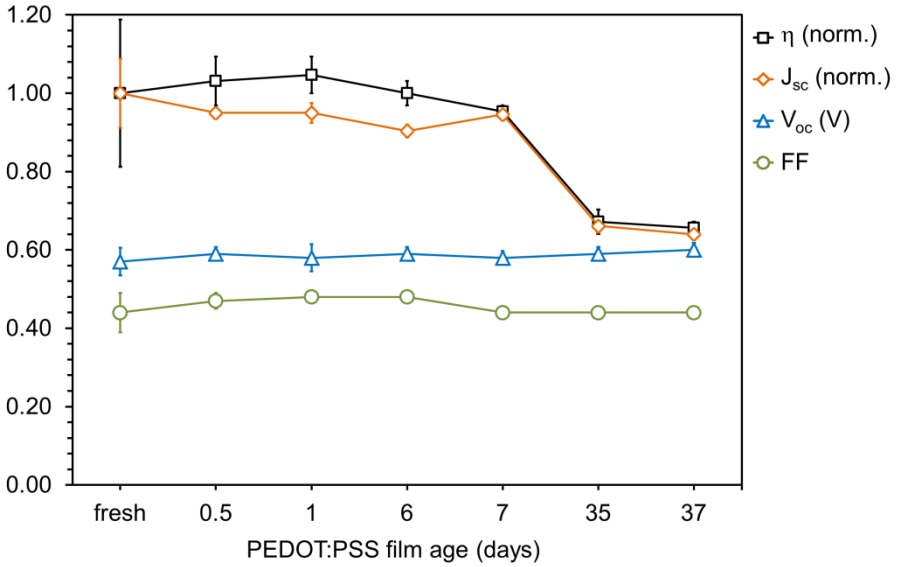

Figure 5.5 Effect of PEDOT:PSS film aging on device performance.

rolling off only at about the one week mark. Even after over a month of exposure to air and light, the devices are able to operate at over 60% of the performance of a completely fresh device. Therefore, when fabricating large device batches, some of the PEDOT:PSS layers are allowed to age while others are being processed. In these cases, the films would have seen a maximum of a few days of aging, which is not a big concern. In most cases, however, a fresh PEDOT:PSS layer is used. Commercial PEDOT:PSS solutions were used as-received, within the quoted shelf life of 9 months.

The next layer to investigate is the MPc layer. Here, both the material purity and the film age are important factors to investigate. First, devices were made using purified and as-received CuPc material that were otherwise identical. The crucible temperature required to maintain a desired deposition rate was 30 ~ 40°C higher for unpurified material, which may be the result of a layer of impurities accumulating in the crucible. The results from these devices are shown in Figure 5.6, where a dramatic increase is seen in all aspects of device performance for those made with purified material. It is important to note that the CuPc material was purified only once for this experiment. The importance of material purity has been emphasized previously [85], where the hole mobility of CuPc is found to increase

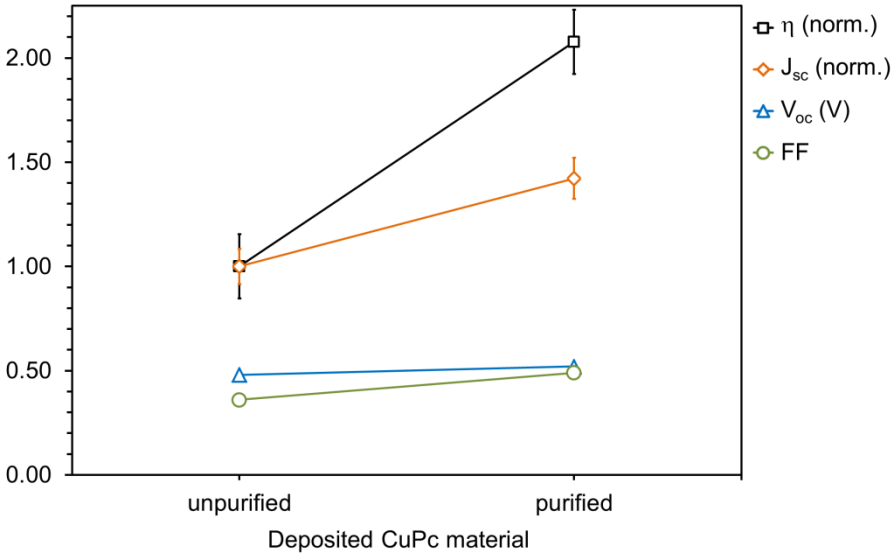

Figure 5.6 Effect of CuPc material purity on device performance.

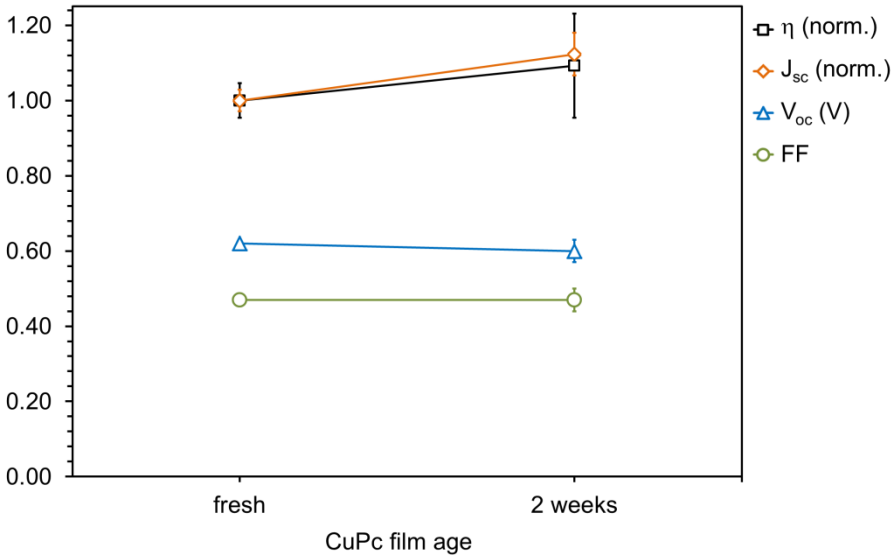

Figure 5.7 Effect of CuPc film aging on device performance.

dramatically by the removal of impurities. Multiple purifications have been found to yield increasingly better results, but the marginal improvements are not worth the extra effort when each procedure is a full day task. Twice purified material seems to be the standard, which is used for all devices in section 5.5.4.

The film age of CuPc was also investigated, the results of which appear in Figure 5.7. Here, fresh CuPc films are compared to ones that have aged for 2 weeks in a dark cabinet with exposure to air. Interestingly, the performance of the aged films shows marginal improvement on average, but is within error of the original values. This is consistent with other studies that have shown higher mobilities in MPc layers as a result of oxygen exposure [110,236,237], despite the surface chemistry remaining unchanged [238]. Similar to PEDOT:PSS, this result enables more relaxed timelines for these films during device fabrication. In some cases, MPc films were allowed to age for several days in dark ambient environments while other devices were being processed. Unlike fresh films that are easily wetted by PCBM solutions, films that are several months old repel them, preventing effective device completion. Therefore, these layers do have a fixed timeframe within which they must be used, but it is the least sensitive of any of the layers.

Out of all the organic layers, the PCBM layer exhibited the greatest sensitivity to air exposure. Solutions of PCBM were always mixed immediately prior to spin-casting, due to the drop in performance seen with aged solutions in Figure 5.8. In addition, devices were transported and tested with a sense of urgency after the PCBM casting, as degradation proceeds very quickly thereafter. This is illustrated in Figure 5.9, where rapid changes to the J_{sc} and FF are evident over short timescales. Significant drops in performance were even observed during testing in many cases. Remarkably, the V_{oc} remained constant, which suggests that the D/A interface is not the source of degradation. The cathode was deposited on top of the PCBM in a glovebox evaporator. This limited the exposure times to ~ 10 minutes between PCBM casting and loading into the glovebox, and ~ 10 minutes between removal from the glovebox and testing. Ideally, PCBM casting and device testing would also take place in an inert environment [107,235]. Without encapsulation, light exposure has been shown to facilitate device degradation [34]. Therefore, samples were hereafter concealed by aluminum foil during transportation between fabrication and testing labs.

The mechanism of PCBM degradation is well studied. Contamination

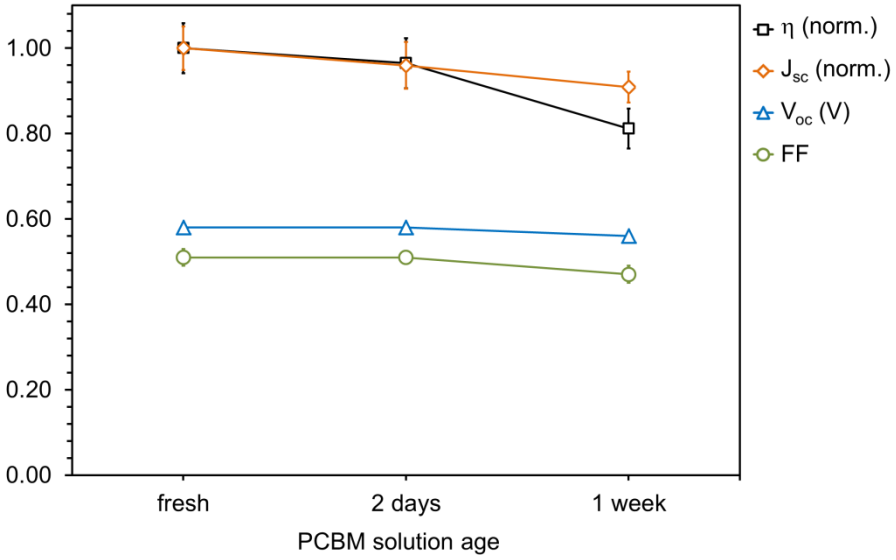

Figure 5.8 Effect of PCBM solution age on device performance

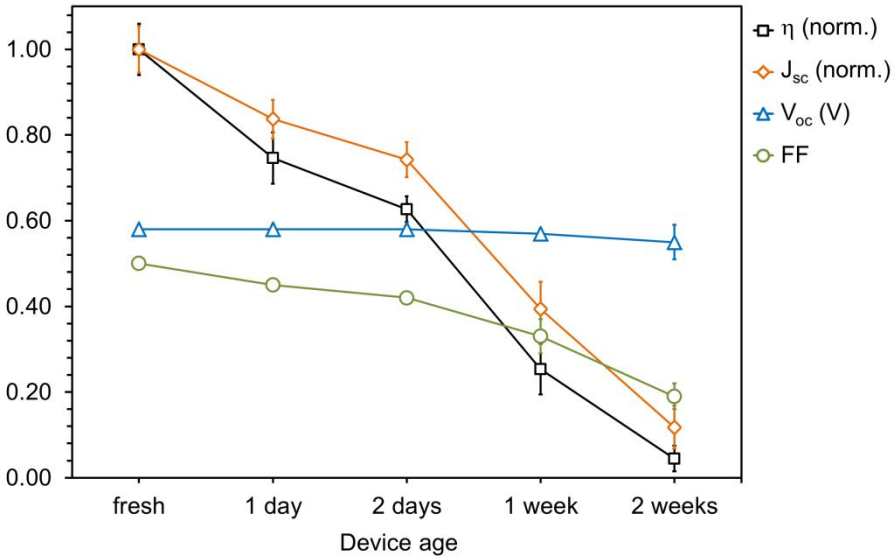

Figure 5.9 Effect of device aging on device performance.

or degradation at any of the interfaces in OPV devices introduces defect and trap states, which impede charge transport. This is revealed by an s-shaped kink in the current-voltage curves, and a correspondingly poor FF [119–122], which is clearly observed in Figure 5.9. In particular, exposure of C_{60} (or PCBM) to oxygen is detrimental to its conductivity and electron mobility

[138,235,239,240], which is consistent with the results presented here. This is in direct contrast with the aging of MPc layers, whose properties are actually enhanced by oxygen exposure. In other words, oxygen in these layers performs well as a p-dopant, and must be avoided in the PCBM layer to ensure optimal performance.

5.5.2. Film thickness optimizations

Proper operation of OPV devices requires a certain degree of thickness precision when depositing organic layers. The thicknesses of the active layer materials either determine or influence each of the η_A, η_{ED}, and η_{CC}. The thickness of the interface layers affect the series resistance and can also be used to determine the placement of the active layer with respect to the incident and reflected optical fields. Ideally, the donor layer would coincide with the maxima of the optical field intensity, which can be achieved by use of an optical spacer interface layer [16,21]. These effects become more critical in tandem devices, where multilayer stacks result in much thicker devices and thickness precision is critical [4,21,67]. This section investigates the effect of varying the PEDOT:PSS, MPc, and PCBM layer thicknesses. The cathode layer thickness is dealt with in the following section.

The PEDOT:PSS layer thickness is least critical to device performance out of any of the organic layers. A thickness of 40 ~ 60 nm is most common. Device results from a 30 nm and a 90 nm thick PEDOT:PSS film are compared in Figure 5.10. A slight decrease in J_{sc} is observed in the device with thicker PEDOT:PSS, which may be due to increased series resistance, but the changes are not dramatic. The 90 nm layer was accomplished by spinning an undiluted solution at 4000 rpm for 30 seconds. The 30 nm layer was made in the same way, but with a 2:1 dilution with deionized water (2 parts H_2O to 1 part PEDOT:PSS). It is important to note that this study was done with a relatively old (several months) bottle of material. Afterwards, fresher material was used, whereby a standard procedure of spinning undiluted material at 4000 rpm yielded a layer thickness of about 40 nm, which was used for all devices in section 5.4.4. The takeaway from the current study is that device

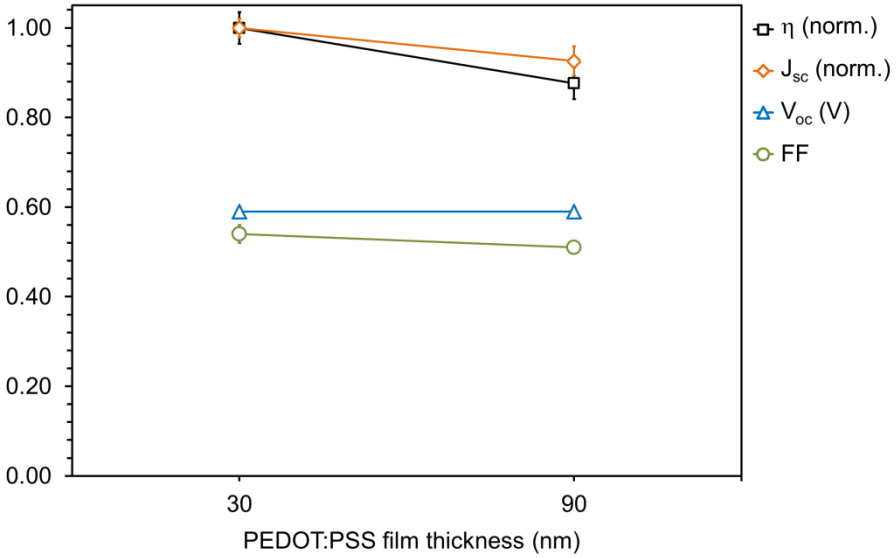

Figure 5.10 Effect of PEDOT:PSS film thickness on device performance.

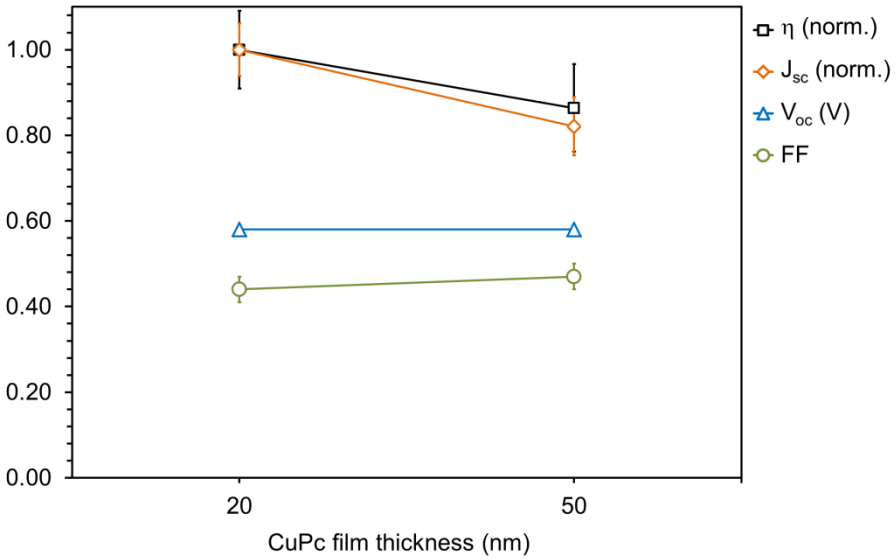

Figure 5.11 Effect of CuPc film thickness on device performance.

performance does not rely heavily on the PEDOT:PSS layer thickness, which is a fortunate and unsurprising observation. As a side note, the bake time for PEDOT:PSS was tracked between 5 – 20 minutes, and no changes to device performance were seen within that range. The standard bake time going forward is 10 minutes.

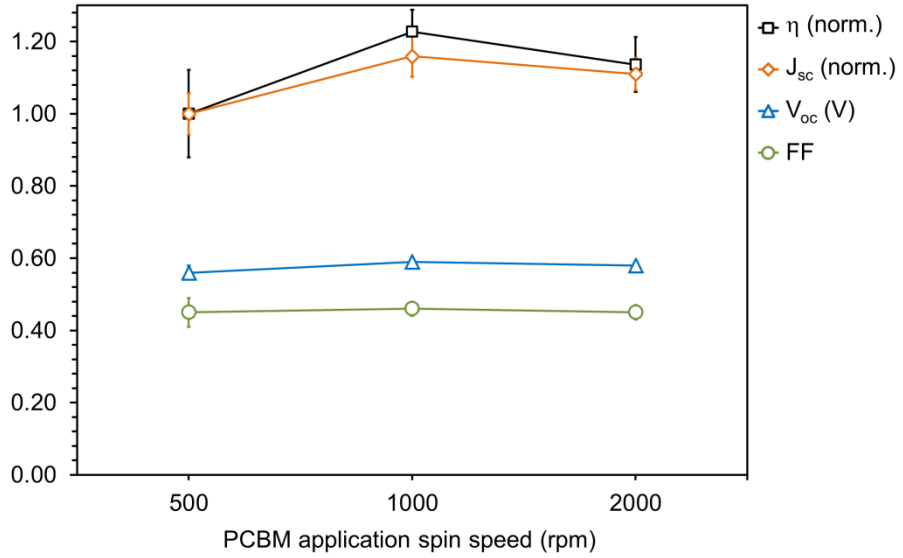

Figure 5.12 Effect of PCBM spin speed on device performance.

The thickness of the MPc layer is more important, specifically because of the short exciton diffusion length in MPc materials, as discussed in Chapter 1. The performance of devices containing CuPc layers of 20 nm and 50 nm thickness is compared in Figure 5.11. Unsurprisingly, the V_{oc} and FF remained constant, but the J_{sc} dropped slightly in the thicker device. This is likely due to a poor η_{ED}, because the layer thickness significantly exceeds L_D. Additional devices were made with much thicker active layers, which showed further drops in performance relative to a 50 nm layer as the CuPc thickness increased.

Similar thickness sensitivities are seen for the PCBM layer, as shown in Figure 5.12. Here, the spin speed is varied during PCBM casting, while always using a 30 mg/mL solution. The corresponding film thicknesses are approximately 100 nm (500 rpm), 40 nm (1000 rpm), and 30 nm (2000 rpm). Unlike CuPc, where an increase in thickness at least improves η_A, an increase in the PCBM thickness is of little value. Meanwhile, a thicker layer increases the series resistance, which is likely responsible for the poor performance of the film cast at 500 rpm. The devices with films cast at 1000 rpm and 2000 rpm perform within error of each other. Going forward, devices are made using 30 mg/mL PCBM solutions spun at 1000 rpm.

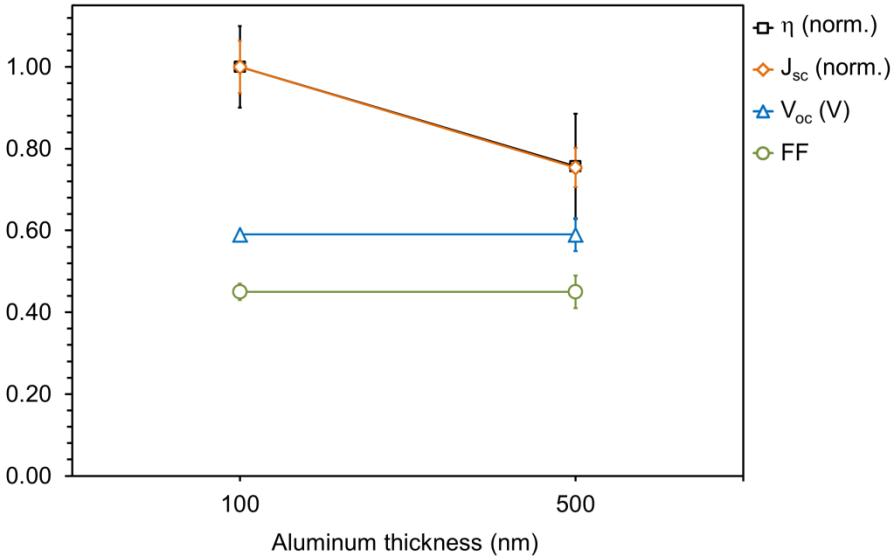

Figure 5.13 Effect of aluminum film thickness on device performance.

5.5.3. Cathode optimization

The design of the cathode is subject to few basic criteria. Strong lateral conductivity and an appropriate work function for electron collection from the active layer are the two most important. A transparent electrode is desired in some cases, for example to provide semitransparent panels for niche applications such as integration into windows. In most cases, however, aluminum is used. The target thickness and deposition rate used to deposit this layer must bear in mind the potential for damaging the device either by overheating or by penetrating the adjacent organic layer. Additionally, the cathode must be robust enough to withstand pressure from spring-loaded pins used to contact devices during testing.

The first experiment on the cathode looked at the effect of a 500 nm thick aluminum layer, compared to a standard layer of 100 nm, the results of which are shown in Figure 5.13. A deposition rate of 5.0 Å/s was used in both cases. The performance of devices with the thick cathode dropped dramatically, which suggests that the devices were overheated during deposition. The additional heat from condensation of five times the aluminum vapor would be significant, therefore excessive heating was likely.

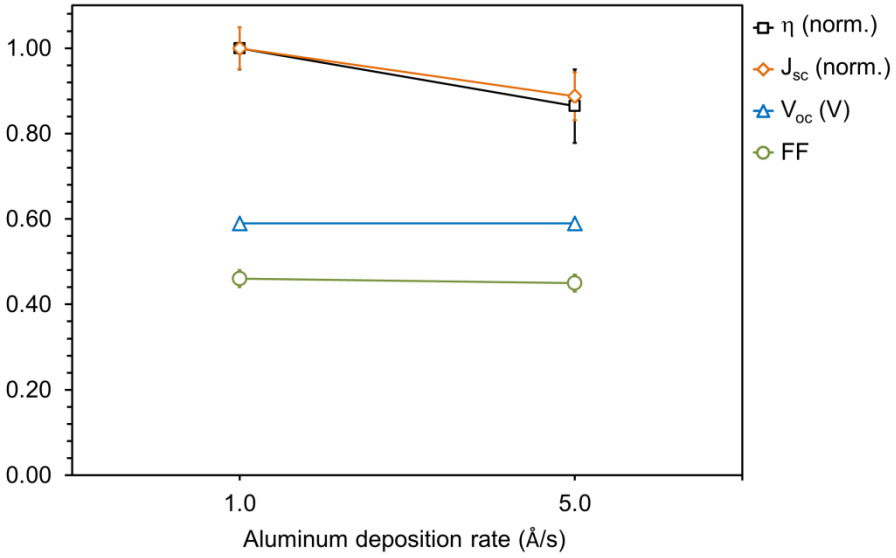

Figure 5.14 Effect of aluminum deposition rate on device performance.

After this, a thermocouple was installed directly beside the sample chuck to monitor temperature. The thermocouple temperature rose rapidly during depositions, reaching 100 ± 10°C for a 100 nm thick film, and often exceeding 150°C for a 200 nm thick film, which is more than significant enough to affect device performance. Heating is not necessarily bad; annealing is often used to improve devices. In particular, annealing at 220 ~ 250°C has been shown to increase the performance of CuPc/PTCBI devices [109,241]. For CuPc/C_{60} devices, the optimal temperature is around 100°C [108,158,242], beyond which CuPc will transition to its β crystalline form and reduce performance [227]. Many annealing experiments were later done on CuPc devices similar to those in Figure 5.13, at temperatures of up to 110°C, but no improvements were seen. The high temperatures reached by the samples during aluminum deposition may explain why post-deposition annealing failed to make further improvements in these cases.

The next experiment on the cathode investigated the effect of the deposition rate. Rates of 1.0 and 5.0 Å/s were compared, and a 100 nm thick aluminum layer was deposited in each case. The results, shown in Figure 5.14, suggest that a lower rate is better. This is likely due to less damage

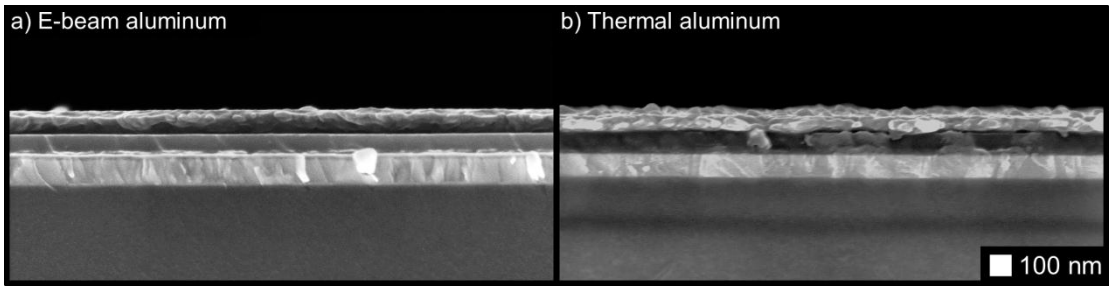

Figure 5.15 Cross-section SEM images of OPV devices. The aluminum deposition method in each case is denoted in the image.

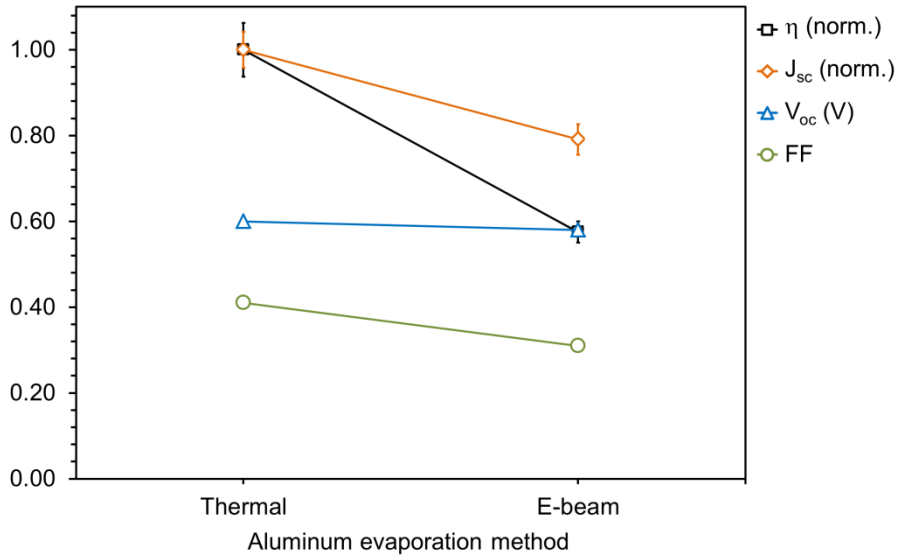

Figure 5.16 Effect of aluminum deposition method on device performance.

occurring at the organic/cathode interface during deposition, which has been the primary motivation for using a buffer layer here [137,138]. A higher deposition rate may result in greater penetration of the active layer and therefore a higher population of defect states at the interface.

Later, a study was done on bilayer ZnPc devices that compared aluminum cathodes deposited using different source heating techniques (see Figure 5.15 and Figure 5.16). In both cases, the deposition rate was around 10 Å/s. The motivation here was to commission an alternative system for cathode depositions, in order to reduce fabrication backlog during the downtimes of the glovebox evaporator. However, the difference in device

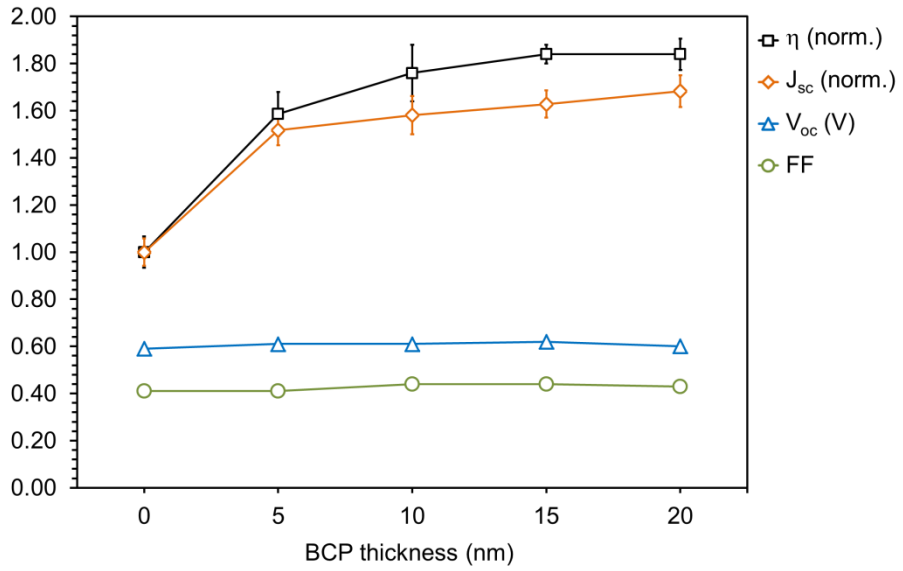

Figure 5.17 Effect of bathocuproine (BCP) film thickness on device performance.

performance seen here is even more severe. The FF and J_{sc} were both negatively impacted by the electron beam deposition process, causing a drop in overall photoconversion efficiency of over 40%. It is likely that the organic layers were damaged by exposure to high energy radiation originating from the electron beam source heating. UV radiation is well-known to facilitate degradation in OPV active layers [34,38], and electron beam source heating emits x-ray radiation [243], which would no doubt be even more harmful to organic materials. As such, all future aluminum depositions were conducted in the glovebox evaporator.

The results of both Figure 5.14 and Figure 5.16 motivate the integration of bathocuproine (BCP), in order to prevent damage to the active layer during cathode deposition. Only a thin layer of this material is required, but the thickness sensitivity of this layer is known to be high [143]. Layers of up to 20 nm were used in this investigation, the results of which are shown in Figure 5.17. In this case, a 100 nm aluminum cathode was deposited on top of the BCP at 2.5 Å/s. The BCP thickness was calibrated by depositing a 50 nm layer on Si, the bulk of which varied between 40-60 nm, resulting in a 20% error on the thickness values. After introducing BCP, the performance of devices not

Table 5.1 Summary of the relative importance of material quality, film degradation, and thickness precision observed for the various layers in MPc OPV devices.

Layer	Material purity / solution age	Film degradation timescale	Optimal thickness (nm)	Thickness sensitivity
PEDOT:PSS	Use commercial solution as is, good for several months	Days	40	Low
MPc	Purify commercial material prior to use	Weeks	20	Moderate
PCBM	Use commercial material as is, good for several months	Minutes	40	Moderate
BCP	Purify commercial material prior to use	-	15	High
Al	Use commercial material as is	-	100	Moderate

only increased, but became less dependent on the deposition rate of aluminum. A rate of 2.5 Å/s was used for all devices that follow, which resulted in more practical deposition times than 1.0 Å/s, while still alleviating concerns related to interface damage.

A summary of all findings in sections 5.5.1 – 5.5.3 related to material quality, film degradation, and thickness sensitivity can been seen in Table 5.1.

5.5.4. Active layer optimization

This section describes two methods to optimize the distribution of donor material within the active layer. The first is by means of dissolution by the PCBM solvent to create a mixed heterojunction, and the second is by using GLAD to create a textured donor film. Together, they form a powerful new approach to improving small molecule active layers. The solvent technique is discussed first, in a bilayer context, after which the nanostructured films are introduced. This is done to isolate the impact of each of these effects, and thereby enable the appropriate attribution of performance improvements due to GLAD structuring.

Bilayer devices: choice of solvent and solution temperature

As a control study, bilayer OPV devices were fabricated with the following architecture: ITO (120 nm) / PEDOT:PSS (40 nm) / ZnPc (50 nm) / PCBM (70 nm) / BCP (15 nm) / Al (80 nm). The PCBM solution temperature was varied to influence the interaction between the ZnPc film and the solvent. Cross-sectional views of these devices are shown in Figure 5.18, which reveal subtle distinctions in the abruptness of the ZnPc/PCBM interface. Though the overall active layer thickness remains constant, the most well-defined boundary between ZnPc and PCBM occurs when the PCBM is applied cold (Figure 5.18a). The current-voltage curves for these devices are shown in Figure 5.19, and device performance metrics are summarized in **Error! Reference source not found.**.

As seen in the current-voltage curves, the solution temperature has little impact when using CB as the solvent. However, a significant improvement is seen in the photocurrent when using DCB as the solvent. This enhancement is likely due to improved mixing of materials at the D/A interface, as observed in the previous chapter (Figure 4.13).

The ZnPc layer used here is thicker than what is typically used in such devices, the purpose of which is to allow an investigation of the unique structures in the solvent-treated films (which, under 50 nm thickness, cease to form platelet structures) as well as to provide an absorption-matched comparison to thicker GLAD-structured devices. Both of these tasks are addressed below.

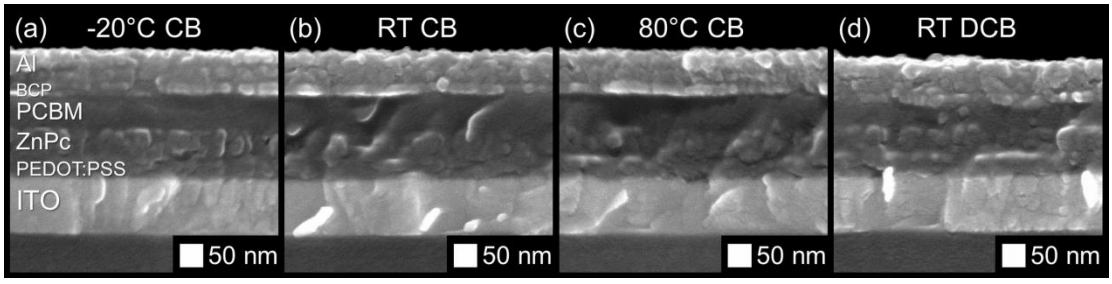

Figure 5.18 Cross-sectional views of bilayer ZnPc/PCBM OPV devices. The PCBM solvent and solution temperature used in each case are denoted in the image.

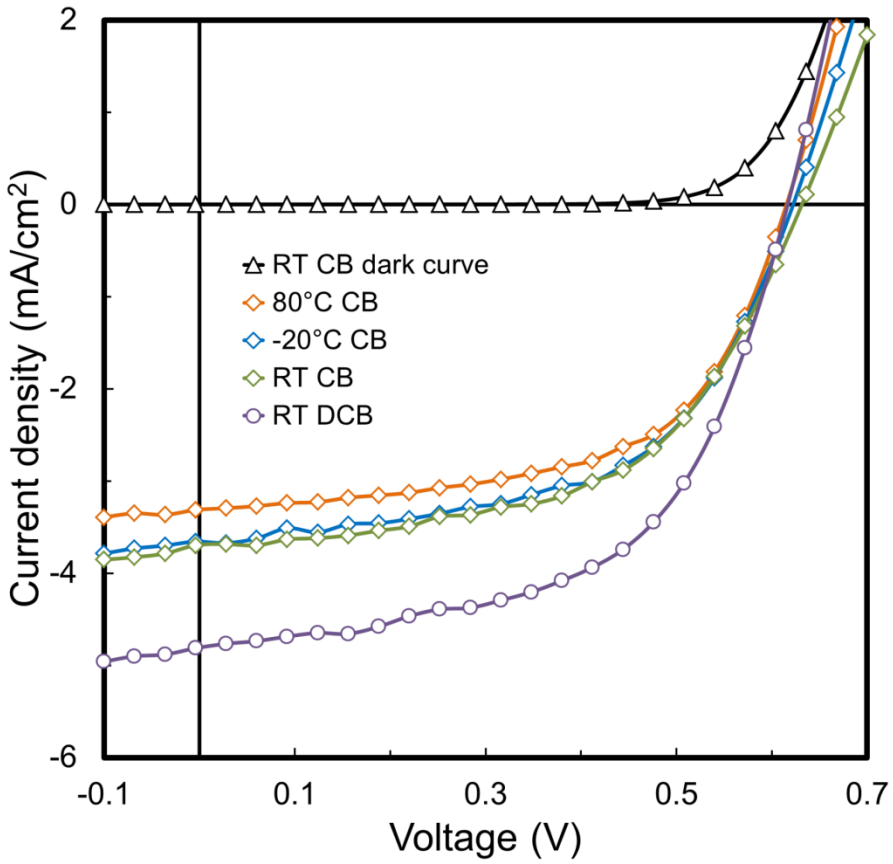

Figure 5.19 Current-voltage characteristics of bilayer ZnPc/PCBM OPV devices made using different PCBM solvents and solution temperatures.

Nanostructured devices

Photovoltaic devices were fabricated with the same layer structure as the bilayer devices, but here the planar layer is replaced with structured ZnPc films. The structuring is accomplished either by depositing with GLAD or by direct exposure of a planar film to solvents using a drop treatment. Figure 5.20 shows cross-sectional views of the PCBM-coated ZnPc films for each of these two approaches. Figure 5.20a is the PCBM-coated version of Figure 4.7c and Figure 5.20b is the PCBM-coated version of Figure 4.8a. The PCBM solutions in both CB and DCB wet the ZnPc films very well, enabling effective filling of the structured films.

With the solvent-structured approach, the platelets seen in Figure 4.7c largely maintain their structure during the coating process (Figure 5.20a),

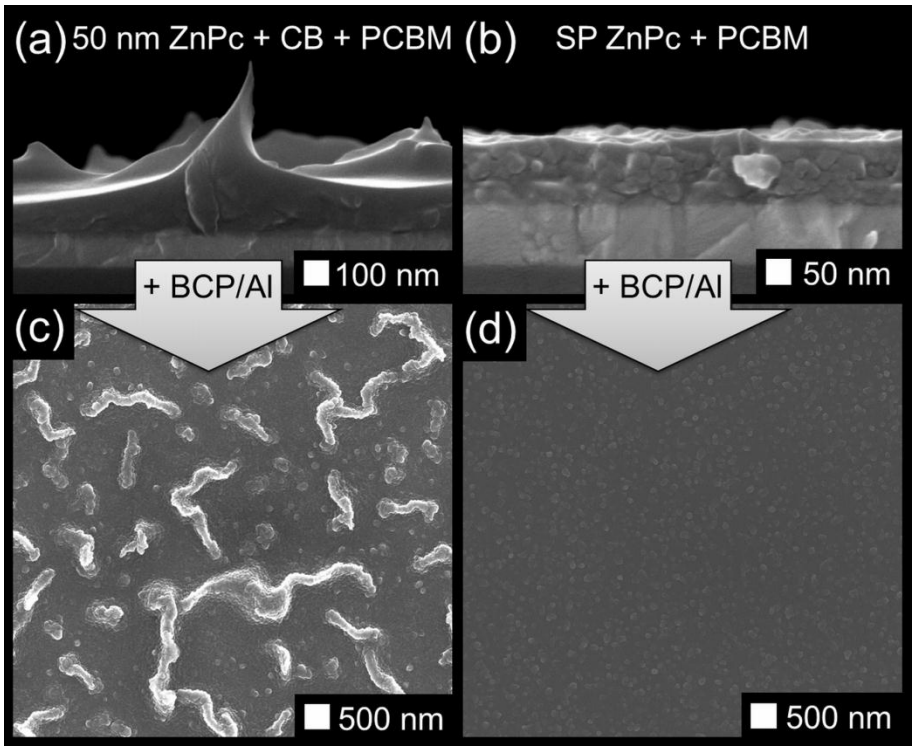

Figure 5.20 Cross-sectional views of PCBM coated ZnPc films and aerial views of the corresponding Al electrode on each. The ZnPc film and solvent used in each case was (a, c) 50 nm planar + CB, CB, and (b, d) 90 nm SP via GLAD, DCB.

which translates into sharp peaks and ridges across the PCBM coating. These contours are still apparent after depositing the BCP/Al electrode (see Figure 5.20c), which suggests that CB is not as able to dissolve ZnPc when being used as the PCBM carrier.

When using the slanted post (SP) ZnPc structured film, the PCBM coating not only fills the film completely but also leaves a much smoother top surface (shown in Figure 5.20b). In addition, the overburden could be controlled by varying the spin speed during PCBM application. OPV devices were made with several of these structured morphologies and thicknesses. Additional bilayer devices were also made, with a 20 nm thick ZnPc layer (as is common for these devices). It was ensured that the bilayer devices had comparable absorption to the structured devices, in order to isolate the effects of morphology alone on photovoltaic performance (see Figure 5.21). The

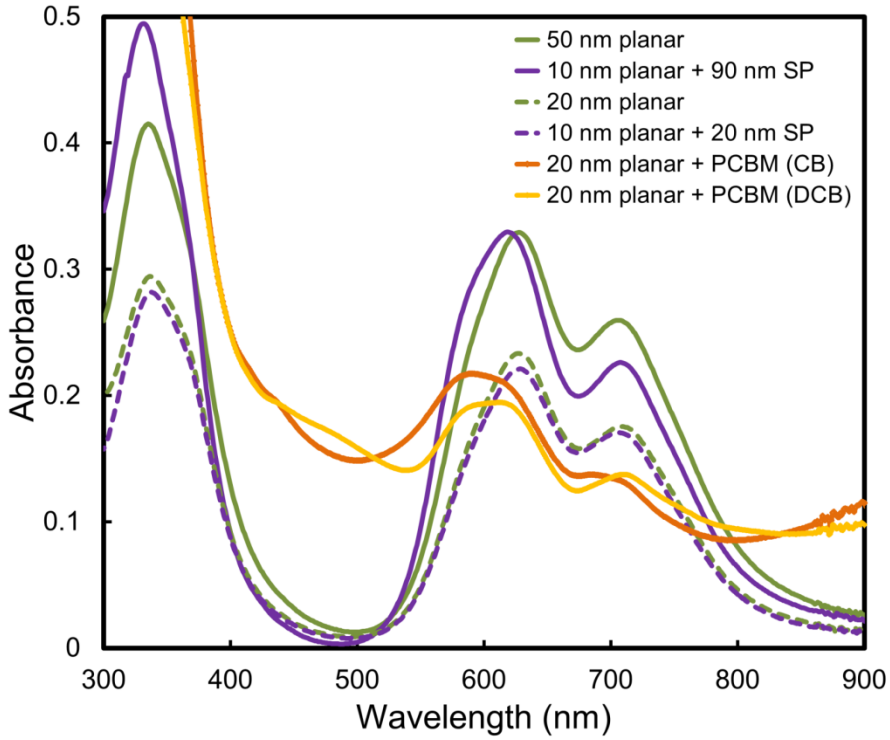

Figure 5.21 Absorbance of various planar, structured, and PCBM-coated ZnPc thin films.

results of all these devices are summarized in Table 5.2, and current-voltage curves for the key structured devices are shown in Figure 5.22.

Solvent treatment prior to PCBM coating hindered device performance in all cases. Even though the CB treatment created somewhat appealing platelet structures, which survived the PCBM coating process, the disorder in the film morphology and changes to the film composition (mentioned in Chapter 4) counteracted any advantage posed by the structure of the crystallites. In the case of DCB treatment, the structures created were far from ideal to begin with (large rectangular boxes with dimensions of 500 nm or greater, similar to those seen in Figure 4.8c). These large box structures were not dissolved during PCBM coating and were still present after complete device fabrication, as confirmed by SEM. Thus, the lower performance is not surprising. However, the fact that photovoltaic activity is still seen in these devices likely means that some of the ZnPc material remains as a functional

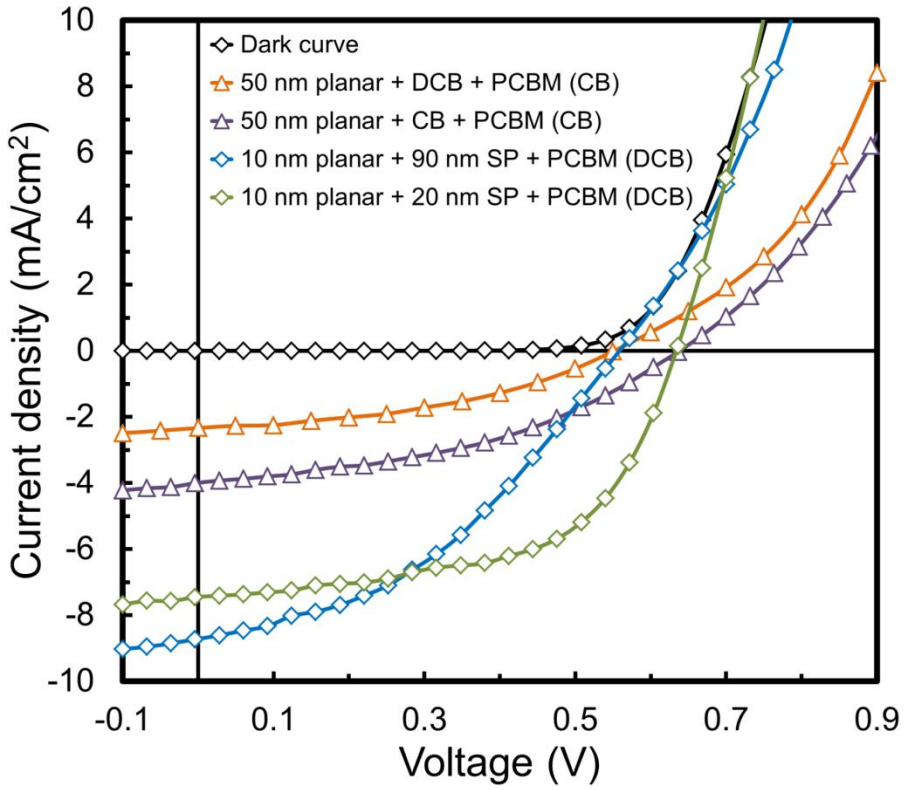

Figure 5.22 Current-voltage behavior of various structured ZnPc OPV devices.

planar layer, while the rest is reorganized into box structures.

Upon examining the performance of the GLAD SP films in devices, the the highest short circuit current density (J_{sc}) is achieved by the thickest film. This is due to the increased light absorption, as shown in Figure 5.21. However, the large active layer thickness allows the poor charge carrier properties of these organic materials to limit the collection of free charges, leading to a low fill factor (FF). In addition, exposure to air may be a greater concern for thick structured ZnPc films, whose larger surface area could permit more severe contamination than less textured films. As a result, the highest photoconversion efficiency is still observed when using the thin structured ZnPc film (10 nm planar + 20 nm SP). In this case, an average photoconversion efficiency of 2.86% is achieved when using DCB as the PCBM solvent. The best result among these devices was 3.0%, which is near the performance of some of the best ZnPc devices to date [97,98,244]. It is

Table 5.2 Performance parameters for various ZnPc/PCBM OPV devices.

ZnPc film morphology	α	Solvent treatment	PCBM solvent	J_{sc} (mA/cm^2)	V_{oc} (V)	η (%)	FF	R_s (Ω cm^2)	R_p (kΩ cm^2)
50 nm planar	0°	-	CB	3.67 ± 0.09	0.624 ± 0.004	1.37 ± 0.04	0.57 ± 0.01	19 ± 4	1.0 ± 0.3
50 nm planar	0°	-	-20°C CB	3.68 ± 0.04	0.617 ± 0.004	1.33 ± 0.02	0.56 ± 0.02	19 ± 1	0.76 ± 0.01
50 nm planar	0°	-	80°C CB	3.4 ± 0.1	0.614 ± 0.002	1.24 ± 0.05	0.57 ± 0.03	22 ± 6	1.0 ± 0.2
50 nm planar	0°	-	DCB	4.9 ± 0.2	0.618 ± 0.006	1.74 ± 0.06	0.55 ± 0.04	16 ± 3	0.7 ± 0.1
50 nm planar	0°	CB	CB	4.09 ± 0.08	0.638 ± 0.001	1.12 ± 0.02	0.41 ± 0.05	16 ± 1	0.46 ± 0.04
50 nm planar	0°	DCB	CB	2.3 ± 0.3	0.56 ± 0.02	0.56 ± 0.07	0.41 ± 0.06	12 ± 1	0.4 ± 0.2
20 nm planar	0°	-	CB	5.7 ± 0.1	0.637 ± 0.005	2.10 ± 0.08	0.55 ± 0.07	10 ± 1	0.6 ± 0.2
20 nm planar	0°	-	DCB	6.8 ± 0.3	0.62 ± 0.01	2.3 ± 0.2	0.51 ± 0.08	9.9 ± 0.9	0.5 ± 0.1
10 nm planar + 20 nm SP	75°	-	CB	5.9 ± 0.2	0.640 ± 0.002	2.29 ± 0.08	0.57 ± 0.09	10.3 ± 0.4	0.6 ± 0.2
10 nm planar + 20 nm SP	75°	-	DCB	7.5 ± 0.2	0.629 ± 0.005	2.86 ± 0.09	0.6 ± 0.1	9.1 ± 0.5	0.6 ± 0.3
10 nm planar + 90 nm SP	75°	-	CB	6.6 ± 0.2	0.583 ± 0.006	1.88 ± 0.06	0.5 ± 0.1	13 ± 1	0.5 ± 0.2
10 nm planar + 90 nm SP	75°	-	DCB	8.79 ± 0.09	0.552 ± 0.005	2.0 ± 0.1	0.4 ± 0.1	10.6 ± 0.4	0.38 ± 0.07

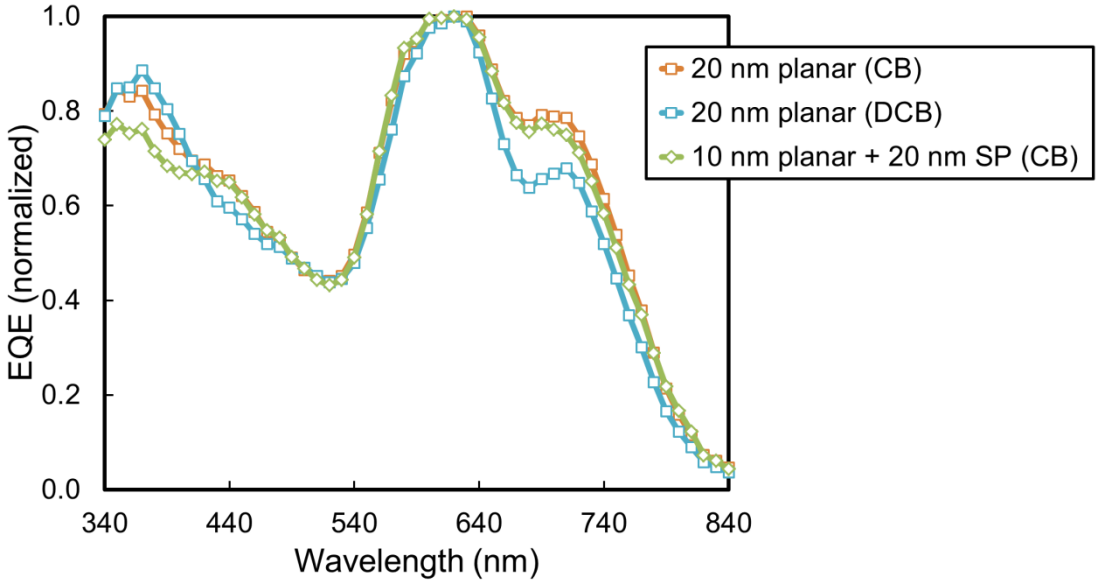

Figure 5.23 Normalized EQE spectra of bilayer and nanostructured ZnPc OPV devices processed with different PCBM solvents (as indicated in the figure).

possible that these results could be further improved by using $PC_{71}BM$ in place of $PC_{61}BM$, as demonstrated elsewhere [16,105–108].

External quantum efficiency (EQE) was measured and compared between the top performing devices to identify the relative contribution of the different ZnPc absorption peaks in each case. Normalized results from these measurements are shown in Figure 5.23. The device degradation that occurred during testing was too significant to use the absolute measured values to calibrate against the photocurrent in the I-V curves. Absolute EQE values were generally in the range of 0.25 – 0.32 near 620 nm, which is on par with standard bilayer ZnPc devices and about half that of the best published results [98,244]. The samples were measured many times, alternating between I-V and EQE, and the J_{sc} decreased between each measurement. The curves shown here are from devices that have experienced a comparable amount of degradation. The relative contribution of different absorption peaks does not change significantly between devices using different ZnPc morphologies or PCBM solvents. Solvent-treated devices degraded even faster than the others,

making it difficult to identify the spectral region responsible for photocurrent in these devices. As shown in Chapter 4, the absorption spectrum of ZnPc films changes significantly upon solvent exposure, enabling access to other spectral regions for potential photoconversion. Encapsulation or inert testing environments would be necessary to gain further insight into these devices.

Overall, the ZnPc morphology improvements created with GLAD provide photoconversion performance enhancement regardless of the amount of material in the device. In other words, with all else being equal, a 10 nm planar + 90 nm SP film always outperforms the 50 nm planar film. Similarly, a 10 nm planar + 20 nm SP film always outperforms the 20 nm planar film. It is significant to note that the series resistances of the devices using a 50 nm planar film are nearly 50% higher than for devices using a 10 nm planar + 90 nm SP film. Remarkably, the series resistances of thick GLAD-structured devices is as low as the thinnest planar and nanostructured devices. In this case it is evident that the nanostructured architecture promotes better charge transport while containing the same amount of material as the bilayer device. The absorbance profiles of these films are used as grounds to determine that they contained a comparable amount of material (see Figure 5.21). Also, Figure 5.21 shows that as the films grow thicker and their morphologies deviate more significantly (between planar and GLAD), so do their absorbance profiles. This is similar to that observed previously with SP CuPc thin films in Chapter 2 (see Figure 2.10).

The absorbance profiles reveal an important difference between the thin bilayer devices prepared using CB vs. DCB as the PCBM solvent, and that is the amount of material stripped off by the solvent during the coating process. In particular, the ZnPc absorbance peak around 600 ~ 620 nm is lower when using DCB than when using CB, suggesting that DCB is more able to dissolve the ZnPc material while holding 30 mg/ml PCBM. Along with the depth profiles in the previous chapter, this supports the notion that the superior performance observed when using DCB over CB is due to more significant mixing at the interface.

5.6. Summary

This chapter focused on optimizing the performance of MPc-based OPV devices. Individual layers were each optimized to establish a fabrication routine for bilayer devices that would yield strong and consistent results. Whereas PEDOT:PSS and MPc layers were found to be fairly robust, the PCBM layer degraded rapidly upon exposure to air, and procedures were implemented to reduce this exposure. The presence of a BCP blocking layer at the cathode was found to improve performance and reduce sensitivity to the cathode deposition rate. Upon achieving a standardized bilayer device, the focus shifted to optimizing the morphology of the active layer materials.

The effects of organic solvents on MPc thin films, which were the topic of Chapter 4, were used to optimize nanostructured ZnPc/PCBM OPV devices. The nanostructured ZnPc film morphologies are maintained when coated with PCBM, but a degree of material mixing occurs that is dependent on the solvent, as per the results in Chapter 4. This indicates that a planar donor layer can yield either a bilayer or mixed heterojunction, depending on the solvent used to cast the acceptor. When using a nanostructured donor layer, such as a GLAD film, the end result can then be a combination of the interdigitated donor and acceptor layers with a mixed heterojunction forming throughout the acceptor region. This provides an alternative approach to the well-established codeposition techniques that are routinely used in fabricating mixed heterojunction OPV active layers, while additionally allowing the use of ideal donor layer morphologies.

Photovoltaic performance in ZnPc/PCBM OPV devices was strongly related to the ZnPc film morphology and thickness, as well as PCBM solvent. The best result was achieved with a 10 nm planar + 20 nm slanted post ZnPc film morphology while using DCB as the PCBM solvent, which exhibited photoconversion efficiencies of up to 3.0%. These findings provide motivation for continued optimization of small molecule OPV devices through a combination of direct donor material structuring and optimal solvent choice for casting the acceptor layer (or vice versa).

6. ION BOMBARDED MPc FILMS[1]

6.1. Introduction

Ion sputtering is often employed by surface analysis techniques, such as AES, XPS, and SIMS, to generate depth profiles of multilayer films. The limits imposed on depth profiling by the effects of ion sputtering on surface topography have been studied thoroughly for many metal and semiconductor thin films [245–255]. Ripples and cones are among the most common surface features produced by ion bombardment. The severity of surface topography changes during ion sputtering depends on the characteristics of the sample and the ion beam, and can often be reduced by means of sample rotation [249,256,257]. Accurate depth profiling of polymer and organic layers is considerably more challenging than inorganic materials, but has been improved as of late [258–264]. Few studies have been done on plasma etched MPc films, and the effects on morphology are not well known.

This chapter investigates the evolution of metal phthalocyanine thin films as they are etched with argon plasma. Significant morphological changes occur as a result of the ion bombardment: a planar surface becomes an array of nanopillars with sub-20 nm diameters. The morphology changes are independent of RF power, which controls the etch rate only. Analysis with XPS shows surface concentrations of copper and oxygen increasing with etch time, while carbon and nitrogen are depleted. Despite these changes in surface stoichiometry, no change is seen in the work function. The UV/Vis and FTIR absorbance profiles, as well as XRD data, show no changes other than the peaks diminishing with etch time. However, the surface changes render the etched films highly resistive, and OPV devices employing these films operate poorly. As a whole, these findings have important implications for the accuracy of various depth profiling techniques employing sputtering (AES/XPS/SIMS), and pose intriguing possibilities for OPV devices which seek nanopillar thin films of MPc materials as an optimal structure.

[1]A version of this chapter has been published in *Molecules* [178].

6.2. Experimental Details

CuPc and ZnPc were purchased from Sigma-Aldrich and purified via thermal gradient sublimation prior to deposition. Both planar and GLAD thin films were deposited in a standard GLAD apparatus, with a throw distance of 34 cm, and a source temperature of about 400°C. A variety of substrates were used, to enable various characterization techniques. ITO-coated glass (Delta Technologies, 8-12 Ω/□) was used for OPV device samples and analysis by SEM; Si wafers (Evergreen Semiconductor Materials) were used for analysis by XRD, XPS, and UPS; KBr discs (Fisher Scientific) were used to gather FTIR profiles; and glass microscope slides (Fisher Scientific) were used for UV/Vis absorbance profiles. Argon plasma etching was performed in an Oxford Plasmalab μEtch RIE chamber, with 110 sccm Ar gas flow and a chamber pressure of 190 mTorr. The standard RF power used was 220 W, but was changed on occasion, as explained in the text.

Electron microscope images were acquired using a Hitachi field emission S-4800 SEM. X-ray photoelectron spectroscopy (XPS) was performed at high vacuum ($< 5 \times 10^{-10}$ Torr) with a Kratos Ultra spectrometer, using an Al Kα radiation source ($h\nu$ = 1486.71 eV). Measurements were done using incident beam angles of 0° and 60° to probe different surface depths. Atomic concentrations were calculated using the relative peak intensities while accounting for the atomic sensitivity factors. Ultraviolet photoelectron spectroscopy (UPS) was performed in the same environment as XPS, using a He I ($h\nu$ = 21.21 eV) radiation source. Absorbance over visible regions was measured with a Perkin Elmer Lambda 900 UV/VIS/NIR spectrophotometer. Infrared absorbance was captured with a Nicolet Nexus 760 FTIR spectrometer with a DTGS detector and a sample chamber purged with N_2. X-ray diffraction (XRD) data was collected by Michael Fleischauer with a Bruker D8 diffractometer, equipped with a Cu source and area detector, and calibrated against a silver behenate reference standard.

For OPV device fabrication, a 30 mg/mL solution of PCBM (American Dye Source) in chlorobenzene (Sigma-Aldrich) was spun onto the CuPc films

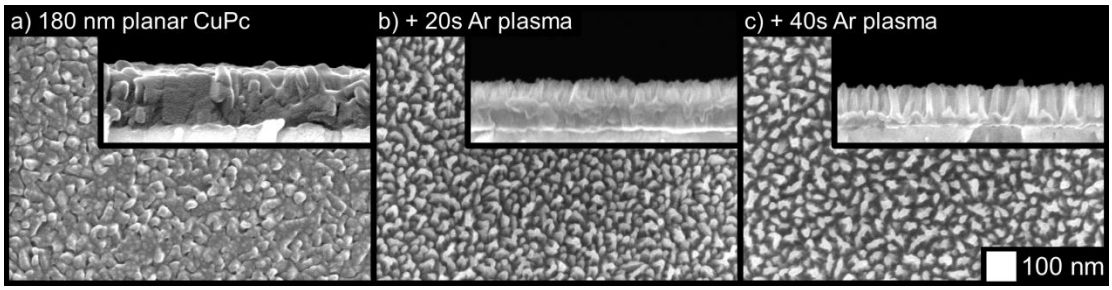

Figure 6.1 Effects of argon plasma etching on a planar CuPc thin film.

at 1000 rpm for 30 seconds. The top electrode consisted of 15 nm bathocuproine (Sigma-Aldrich) and 100 nm Al (Lesker), deposited over 5 rectangular device areas of 0.20 cm^2 each, in a glovebox evaporator. Current-voltage curves were taken in air using a Keithley 2400 source meter, under AM 1.5 G simulated irradiation (Oriel 91191 1000W).

6.3. Results and Discussion

6.3.1. Columnar MPc film morphologies via plasma etching

The first nanopillar films were fabricated by etching a set of 180 nm thick planar CuPc films with argon plasma. Films were etched with an RF power of 220 W for 20 and 40 seconds, resulting in the fascinating columnar morphologies seen in Figure 6.1. Simply from a morphological perspective, the dimensions of the columnar film features are far superior to any of the films presented in this thesis so far. With column diameters of around 20 nm or less, they are smaller than the columns found in the best small molecule films produced to date [175], and are extremely well suited to the exciton diffusion lengths of MPc materials. In addition, the etched columns in Figure 6.1c are wider at the base and taper off at the top, making them more robust than the GLAD films which struggled with top-heavy columns due to broadening. From a structural perspective, this may improve their survivability during the solution-based filling process.

Etching with oxygen gas instead of argon was also performed, with a chamber pressure of 150 mTorr, RF power of 220 W, and gas flow rate of 80

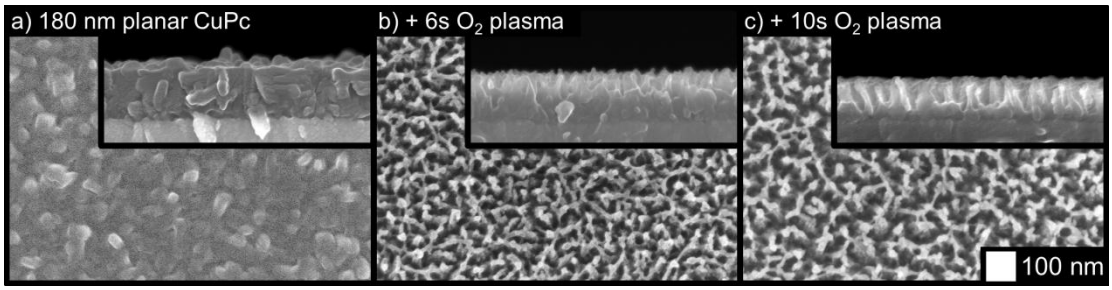

Figure 6.2 Effects of oxygen plasma etching on a planar CuPc thin film.

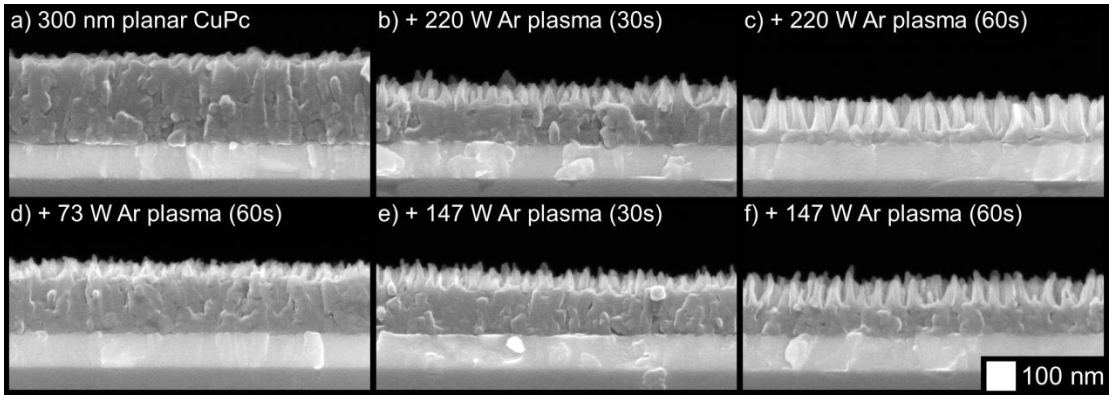

Figure 6.3 Effects of different etch conditions and etch times on the morphology of CuPc thin films etched with argon plasma.

sccm. The results are shown in Figure 6.2. Here, etching proceeded much faster due to the reactivity of ionized oxygen, which enhances removal of organic material in conjunction with physical sputtering. A somewhat similar final morphology can be achieved with oxygen plasma compared to argon plasma, albeit with a more disordered and fragile network of remaining features. The likelihood of chemical changes to the film is higher with oxygen, making oxygen plasma etched films less interesting than argon plasma etched films. As such, argon was determined to be the etching gas of choice, and no additional oxygen-etched films were investigated.

The RF power was varied to investigate the sensitivity of morphology to the etch conditions. A 300 nm planar film was exposed to argon plasmas for various periods of time with three levels of RF power: 73 W, 147 W, and 220 W. The images shown in Figure 6.3 reveal similar etching behavior in all cases, only at different rates. Etched films resembled others that were etched

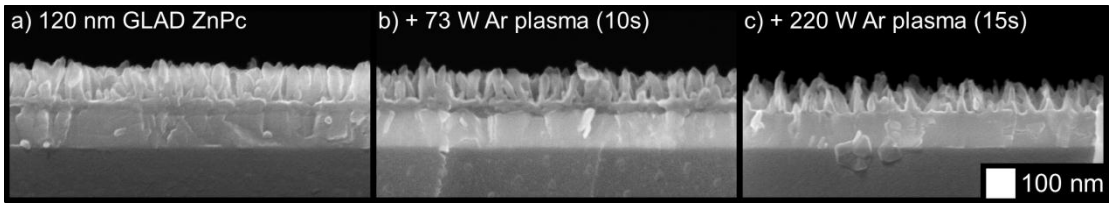

Figure 6.4 Effects of different argon plasma etching conditions on a thin GLAD ZnPc film.

to similar depths under different conditions. Thus, the etching mechanism remains the same, and changes in RF power affect etch rates only.

It may be possible to further improve these etched film morphologies by starting with an already textured MPc film, for example a GLAD film. This approach could introduce additional control over columnar dimensions and spacing, while requiring less etching and disturbance of the original film. Alternatively, this approach can be thought of as a way to refine the structure of a GLAD film via ion bombardment, which is not an entirely new concept. In fact, ion milling and reactive ion etching have been shown previously to enhance the morphology and properties of various inorganic GLAD films in other applications [265–269]. Figure 6.4 shows the effects of etching a 120 nm GLAD ZnPc film. The original film has a slanted post morphology (pointing into the page), which appears largely untouched by a low power etch but deteriorates significantly under a more aggressive etch (Figure 6.4b vs. 6.4c), with an overall thinning of the areal density of posts observed. In these cases, any structural enhancements due to etching are not obvious. It is possible that a vertical post morphology may be more receptive to plasma etch refinements, and that thicker films with broader columns would benefit more, but this will require future study.

6.3.2. Surface analysis and electronic properties

The creation of columnar film morphologies out of planar ones with ion sputtering potentially affects the surface composition. The harmful effects of UV radiation from the plasma alone may impact the survivability of the sample [34,38]. In addition, when considering that the ion energies from the

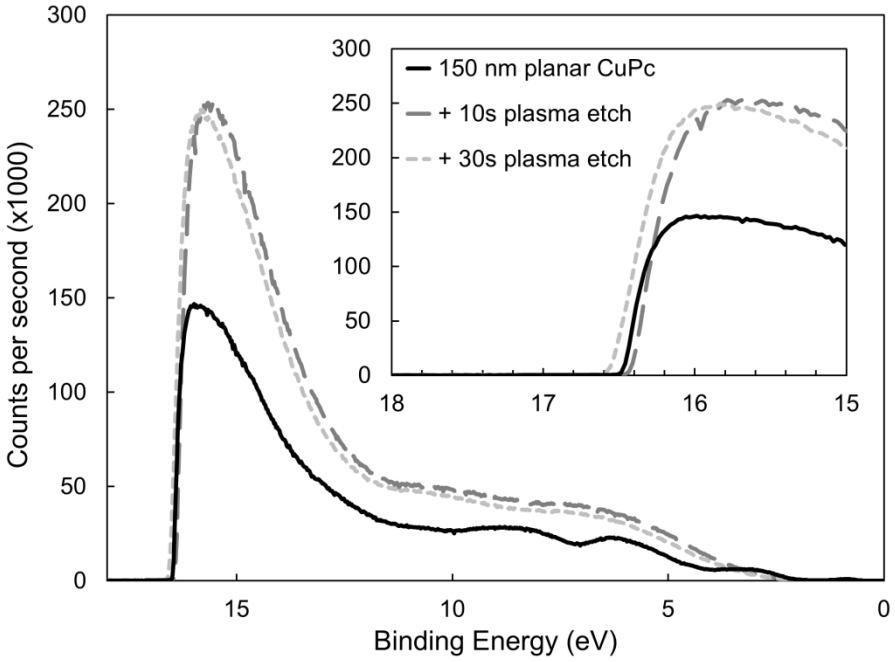

Figure 6.5 Changes to the UPS spectra of a planar CuPc thin film due to argon plasma etching.

plasma are at least comparable to or greater than the intramolecular bond energies in metal phthalocyanines, changes in surface composition may be expected [270,271]. Unsurprisingly, ion beams with MeV ion energies have been shown to be very destructive to MPc molecules [272]. However, the strong π network of MPc molecules may help them avoid fragmentation from impacts of only tens of eV, due to protection by delocalized electrons [273].

The surfaces of the etched CuPc films in this investigation were analyzed with ultraviolet photoelectron spectroscopy (UPS) and x-ray photoelectron spectroscopy (XPS). The UPS curves, shown in Figure 6.5, show virtually no change in the onset energy for electron ejection, at around 16.5 eV. Consequently, the work function is consistent across all samples, at 4.7 ± 0.1 eV, which is slightly higher than other published values [108,242], but may be simply due to more air exposure [238]. These results provide little insight into the effects of etching, and direct contact resistance measurements could not be performed due to the mechanical sensitivity of the nanopillar films. Analysis by XPS reveals more significant information.

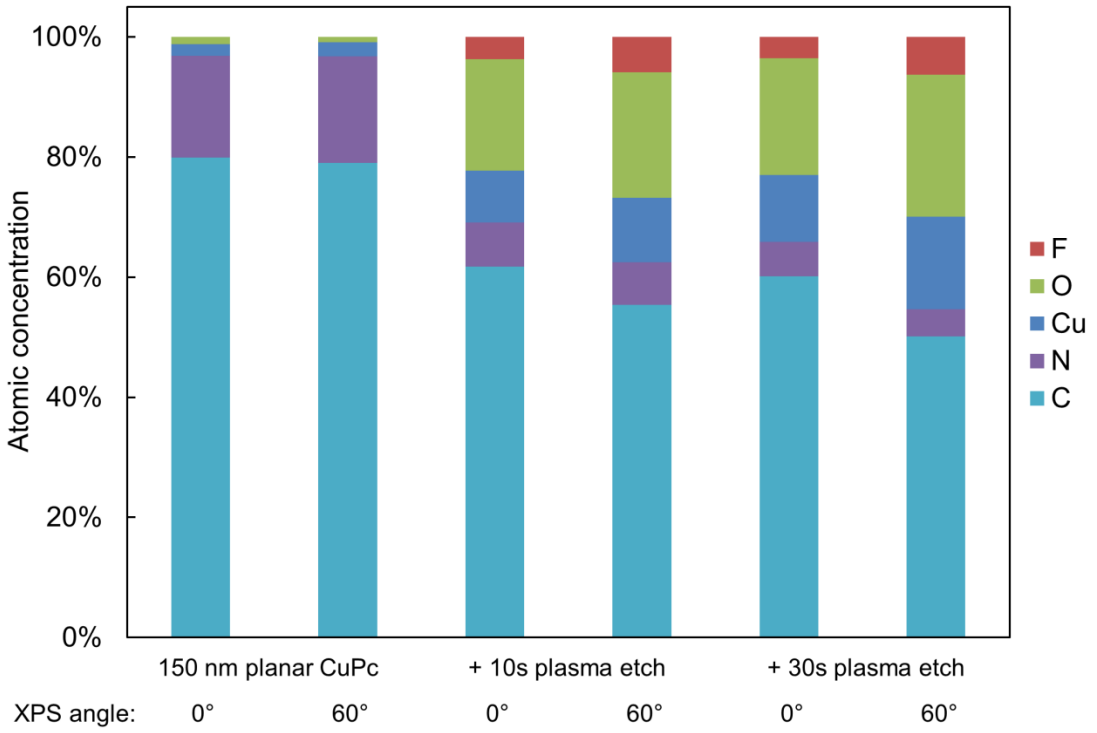

Figure 6.6 Changes to the surface composition of a planar CuPc thin film due to argon plasma etching.

The atomic concentrations of various elements were calculated from the relative XPS peak heights, and are presented in Figure 6.6. Significant and immediate removal of C and N is evident in the sample etched for 10 seconds, which does not change much further in the 30 second etch. Meanwhile, higher concentrations of Cu are revealed by the etching, which is consistent with results from other etch chemistries [271]. Evidently, the CuPc molecules are not surviving the impacts of the Ar ions, and lighter elements are being preferentially removed over heavier ones. Interestingly, a significant amount of O and F are introduced to the surface, which are likely the result of residual gases in the etch chamber binding to the fragmented molecules as a means of stabilization. For device quality CuPc it may be necessary to perform the etching in a UHV environment. The composition of the original planar CuPc film is independent of the incident beam angle, which suggests that the surface and subsurface are very similar. For the etched films,

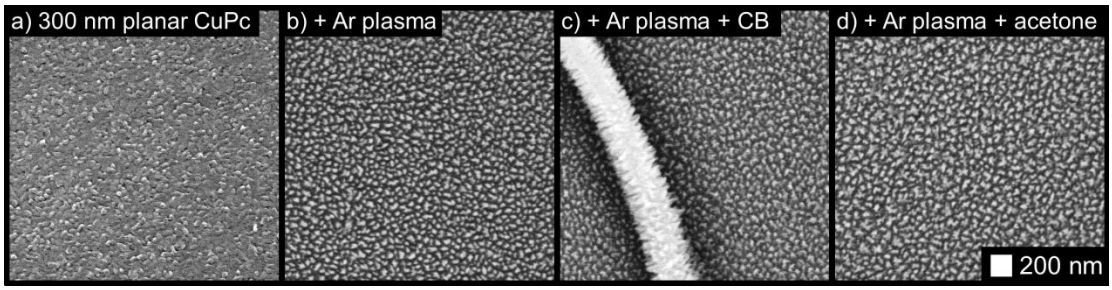

Figure 6.7 Effects of solvent exposure on an argon plasma etched CuPc film.

however, the surface is slightly richer in Cu while being depleted of C and N, which confirms the preferential removal of C and N over Cu mentioned previously. These changes to surface composition leave little optimism for potential functionality at the OPV active layer interface.

As seen in Chapter 4, MPc thin films demonstrate recrystallization effects as a result of exposure to various organic solvents. The etched films were also subjected to solvent exposure, but showed no morphology changes, as seen in Figure 6.7. The only effects seen were film buckling, presumably due to stress induced in the film, as a result of exposure to chlorobenzene. This lack of film restructuring indicates either a lack of CuPc remaining in the film, or a barrier present at the film surface that cannot be penetrated by the solvents. From the absorbance data that follows, the barrier explanation is more plausible, but the film would not be functional for use in OPV active layers in either case. These unfortunate results are not surprising, as hardening of MPc films by plasma irradiation has been observed when using other etch chemistries as well [271].

Despite the significant surface changes, OPV devices were made using these columnar etched CuPc films. The films were easily filled by coating with PCBM, as shown in Figure 6.8. As expected, the devices exhibited very high series resistance and no photovoltaic behavior, as seen in Figure 6.9. The active layer interface was not functional. Not only was current unable to pass through the device, there was no exciton dissociation at the interface, as evidenced by the lack of photocurrent under illumination. Unfortunately, it appears that achieving functional OPV devices that employ plasma etched MPc layers will be very challenging.

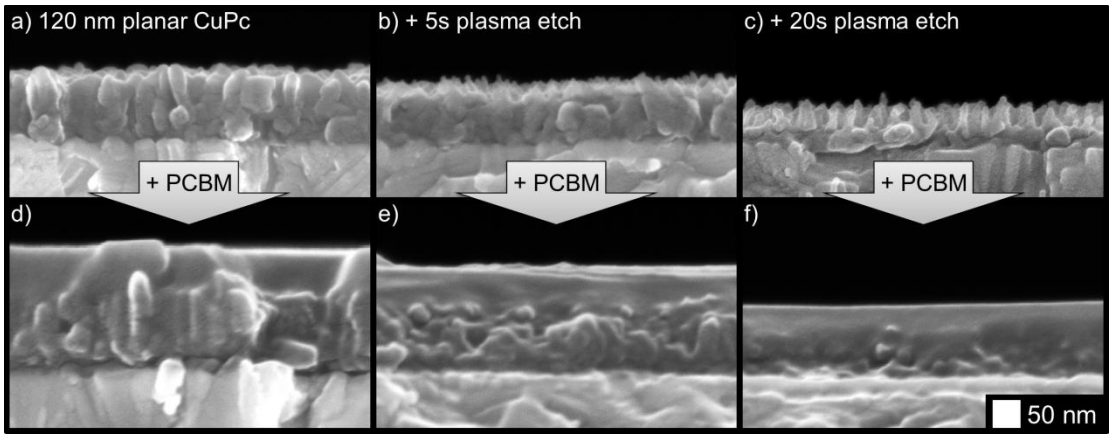

Figure 6.8 PCBM coatings on planar and etched CuPc thin films.

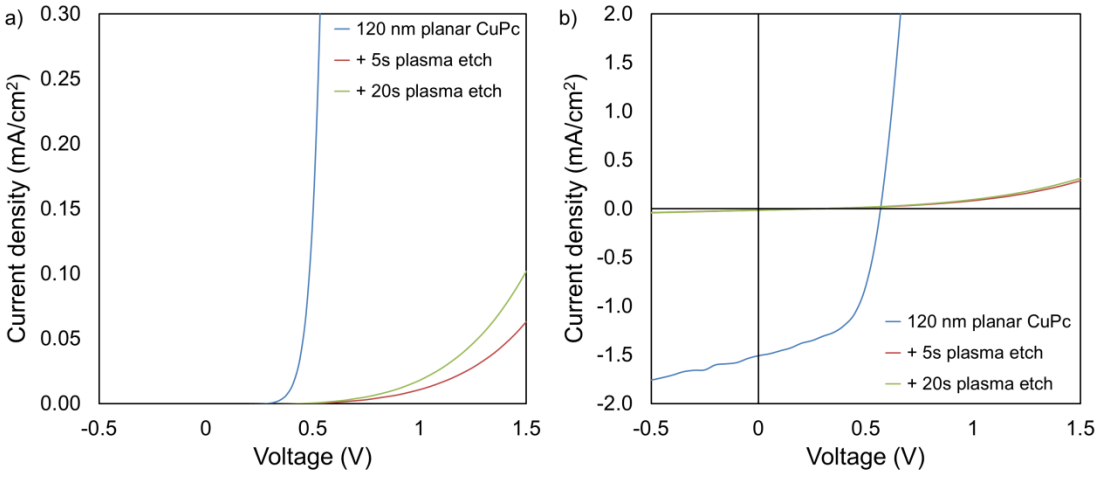

Figure 6.9 Current-voltage behavior of OPV devices containing planar and etched CuPc layers a) in dark conditions, and b) under illumination.

6.3.3. Bulk film analysis

The disappointing device results shown in the previous section question whether any CuPc material remains in the etched films at all. Absorbance profiles were gathered in both the visible and infrared spectral regions, which are shown in Figure 6.10 and Figure 6.11, respectively. In both cases, no changes to the shape of the absorbance spectra are seen as a result of the etching, but only diminished peak heights. This is consistent with the removal of material seen by SEM, and confirms that much of the remaining film avoids being damaged. Likewise, the XRD profiles shown in Figure 6.12

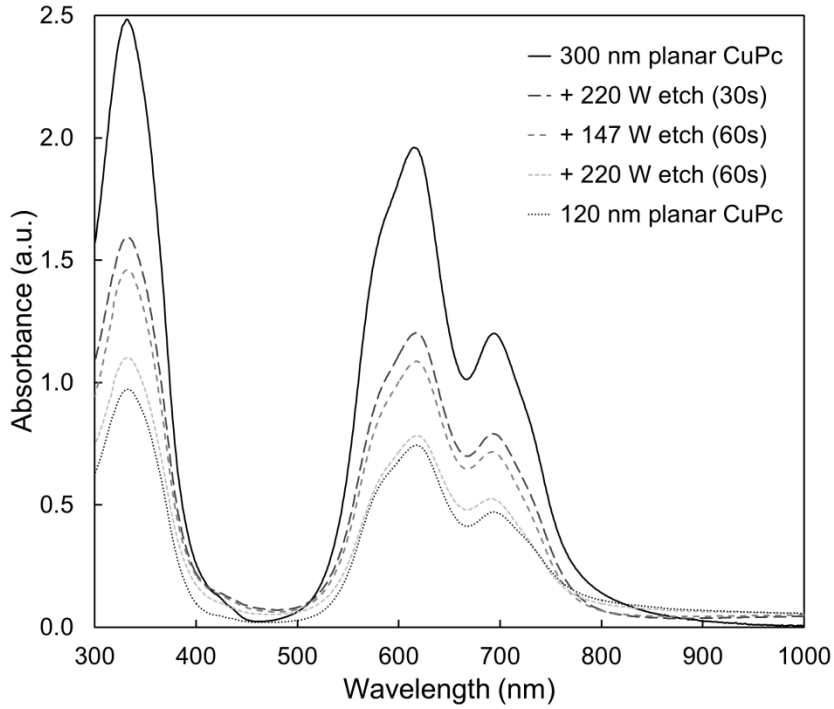

Figure 6.10 Changes to thin film absorbance as a result of argon plasma etching.

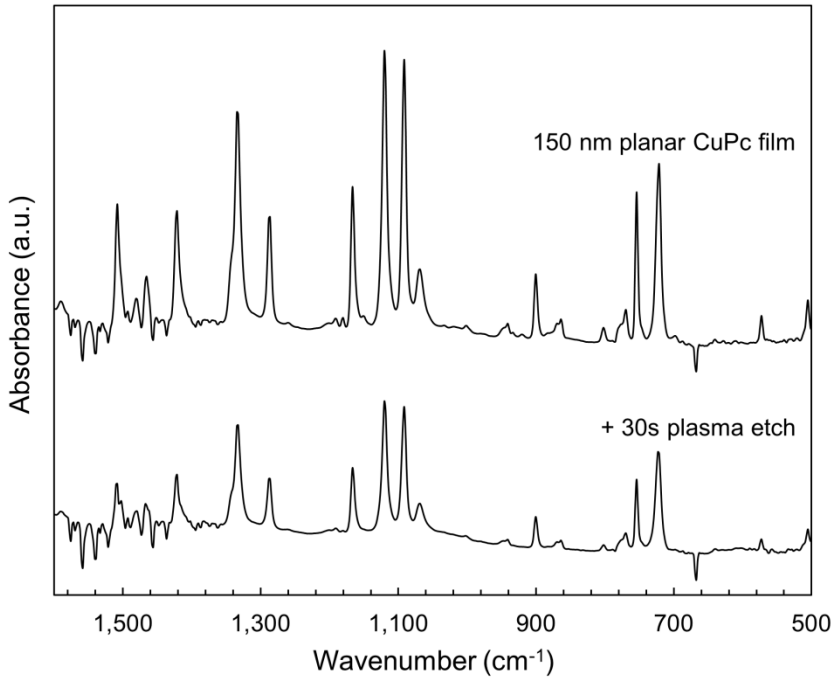

Figure 6.11 Changes to FTIR absorbance spectra of a CuPc thin film due to 220 W argon plasma etching.

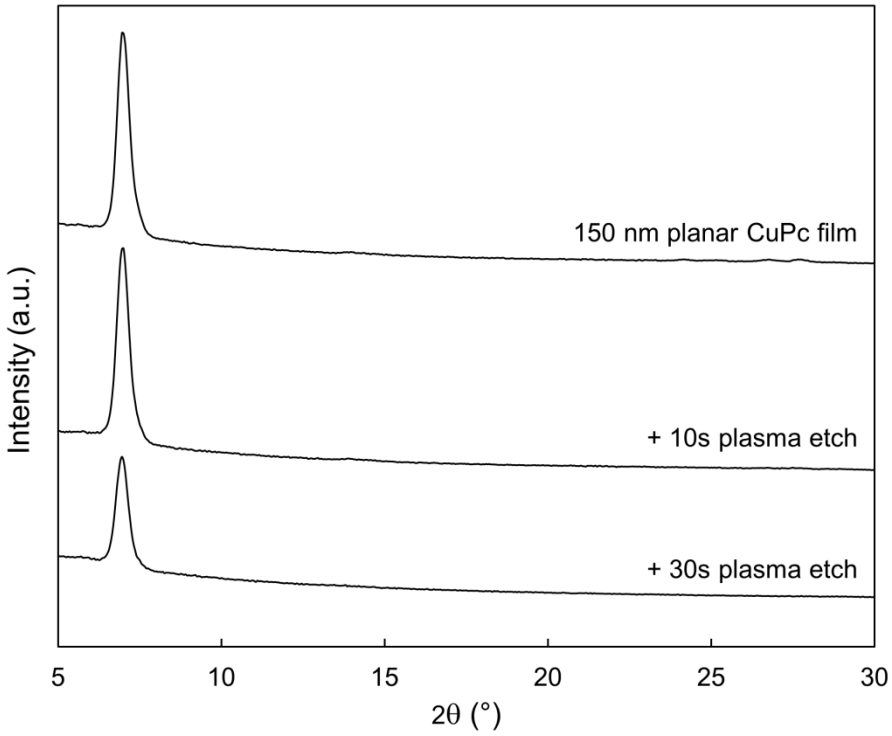

Figure 6.12 Changes to the XRD spectrum of a planar CuPc thin film as a result of 220 W argon plasma etching.

show no changes other than peaks diminishing with etch time. Thus, the material that does remain in the film appears to maintain both its molecular and crystalline structure. It is significant to note that the remaining absorbance of the most etched CuPc film in Figure 6.10 maintains comparable absorbance to a 120 nm planar un-etched film. Therefore, these films possess nearly the same amount of CuPc material, equivalent to six times the amount used in a typical bilayer OPV device. This confirms that the film morphology seen in Figure 6.3c is suitable as an ideal OPV active layer architecture. Every point of light absorption in this nanopillar film would be within a single exciton diffusion length of the D/A interface, and the film would capture significantly more incident light than a commonly used 20 nm planar layer. If the interface were functional, the architecture fabricated by plasma etching would be very useful.

Alternative sputtering techniques may enable structuring of MPc films while minimizing surface damage. Recently, C_{60} ion beams have been used to minimize sputtering damage to organic films during analysis [260–264]. Increasing the incident angle of the ion beam has been found to further minimize sputtering damage [264]. Coincidentally, C_{60} is the acceptor molecule commonly used with MPc materials in the active layer of small molecule OPV devices. This may be very suitable if ion energies are used that are conducive to maintaining molecular structure, particularly since any residue in the film from the ion beam may be functional in the active layer. Therefore, attempting damage-free, ion-induced structuring of MPc films with C_{60} is a topic worthy of further investigation.

6.4. Summary

This chapter investigated the effects of argon plasma etching on metal phthalocyanine thin films. Planar films of these materials are readily transformed into nanopillar films with dimensions extremely well suited to OPV devices. The films maintain much of their original molecular characteristics, such as absorbance profiles and crystalline order. However, changes to the surface composition suggest that the ion bombardment causes fragmentation of the molecules at the film surface, leaving the films with much higher electrical resistance, thus making it difficult to exploit their ideal film morphology to improve OPV device performance. Meanwhile, the morphology changes point to additional complexity for depth profiling of multilayer films containing these materials.

7. NANOPILLAR ITO VIA Ar PLASMA[1]

This chapter presents vertically aligned ITO nanopillar films achieved by exposing planar ITO films to Ar plasma, as shown in Figure 7.1. The etch conditions determine the size, spacing, and aspect ratio of the pillars. Annealing in air and forming gas is used to recover and optimize the optical transmittance and electrical conductivity of the nanopillar films. The final product is an ITO film whose superior optical transmittance and strong electrical conductivity combine with its robust columnar morphology and processing scalability to make it suitable for use in highly absorbing organic solar cells.

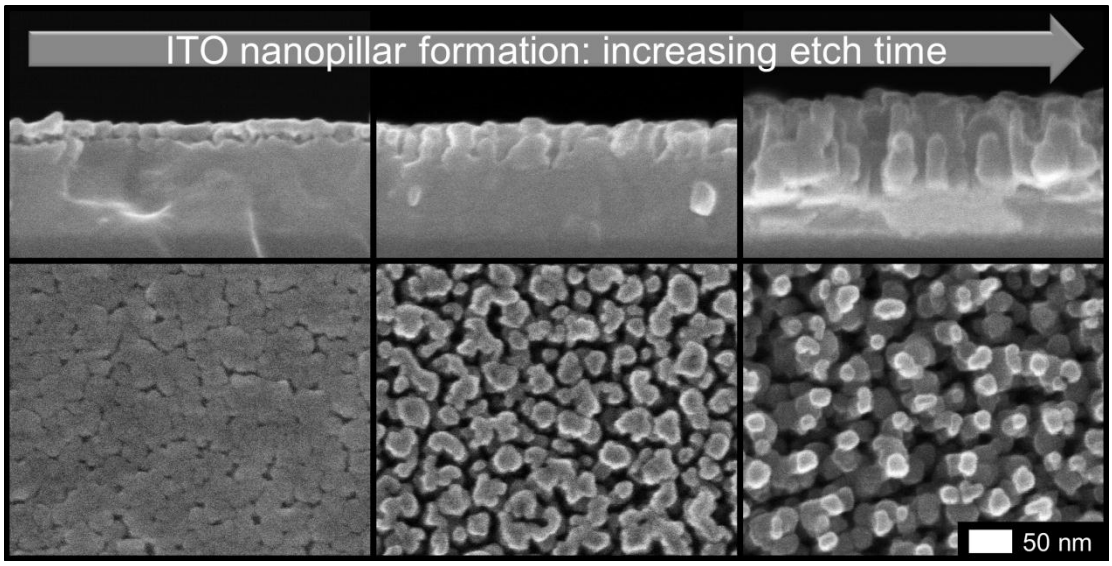

Figure 7.1 Illustration of nanopillar ITO formation due to argon plasma etching.

7.1. Introduction

Indium tin oxide (ITO) is a transparent conducting oxide commonly used for sensors, displays, light emitting diodes, and solar cells [146,274–285]. It is most commonly used as a planar film, but in some cases higher surface

[1]Portions of this chapter have been reprinted with permission from [179]. Copyright [2012], American Vacuum Society.

area is useful. In particular, polymer OPV devices stand to benefit from nanostructured electrodes which could facilitate charge carrier collection from materials with poor mobilities. In these devices, optimal efficiency is typically achieved with active layers around 80 nm in thickness and is quite sensitive to variation [16,17,50,285–288], which presents serious challenges from a manufacturing perspective [289]. Thicker active layers (200 ~ 300 nm) are desired to improve absorption and reduce the sensitivity of performance to thickness variation [289–291]. However, this leads to increased series resistance and reduced quantum efficiency as a result of the poor charge carrier transport properties of the polymer and the build-up of space charge. Thus, in the absence of materials with higher mobilities, a new strategy for improved charge collection is required. Nanostructured ITO electrodes provide a solution to these issues by facilitating charge collection and thereby enabling performance improvements, as shown previously [193,292–296].

A nanostructured electrode could also be useful for small molecule OPV devices, not only with a MHJ (similar to polymer devices), but also for a conformal coating approach, as illustrated in Figure 7.2. In this case, exciton transport to the D/A interface would occur orthogonally to the direction of incoming light, so η_A and η_{ED} could be decoupled. As a result, η_A could be maximized while maintaining a very thin donor layer, which would ensure that η_{ED} and η_{CC} remain high as well. Electrons would have to travel a further distance through the acceptor to reach the cathode, but this would likely not be a serious issue given the superb transport properties of fullerenes. Achieving a conformal coating may be challenging, but a technique such as electrodeposition may be useful here, which has been used previously to create CuPc nanowire structures [297,298]. Alternatively, layer-by-layer deposition of a CuPc-based active layer has been demonstrated [299], which may be another route to conformally coating a nanostructured electrode. These studies are left for future work, while the current chapter focuses on structuring ITO.

Nanostructured ITO has been performed using a variety of techniques [300–304], but a more robust, uniform, columnar morphology is still needed.

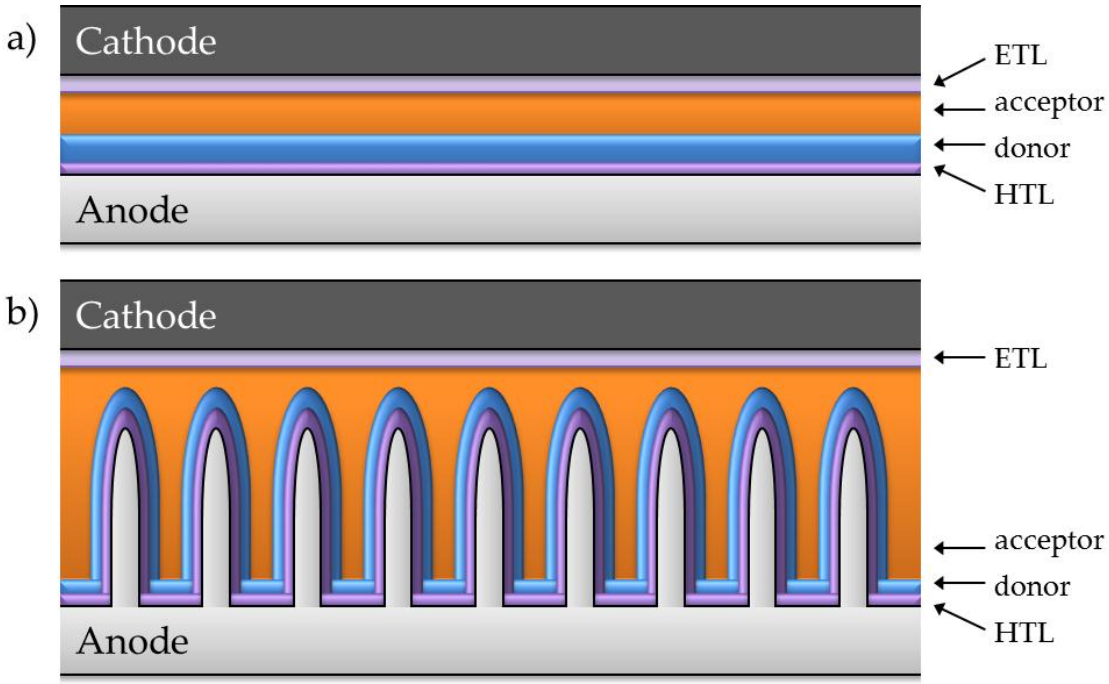

Figure 7.2 Cross-sectional device architecture for a) a conventional bilayer OPV device, and b) a nanostructured electrode device with conformal donor layer coating.

This chapter employs the use of argon plasma etching, an established and scalable manufacturing process which enables large-area uniformity and a variety of tunable parameters for application specific optimization. This approach requires no additional deposition of material and lends itself well to current manufacturing processes. Uniform nanopillar arrays with appealing dimensions for OPV devices are achieved.

Etching of ITO in optoelectronic devices is often used to pattern films at the microscale via lithography [277,280,282,305]. Ion beam erosion has been found previously to modify the surface morphology of several metals and semiconductors [245,246,252–255,306], but is usually undesirable. This chapter presents a variety of appealing nanopillar ITO film morphologies achieved by the use of argon plasma etching.

7.2. Experimental Details

Commercial ITO was acquired from Delta Technologies (10 cm × 10 cm, 8-12 Ω/□, 120 ± 10 nm thickness on 1.1 mm polished corning float glass), diced into 1 inch squares, and rinsed with IPA and deionized water before use. Etching was performed in an RIE chamber (Oxford Plasmalab μEtch) at between 150 – 190 mTorr (regulated by an exhaust control valve), with 110 sccm Ar gas flow and RF power of 200 – 290 W (13.56 MHz). A two-stage annealing procedure was used to improve the optical and electrical properties of the films, as described in [193]: 90 min at 500°C in air followed by 60 min at 375°C in 5% H_2 (balance Ar). Images were acquired with a Hitachi field emission S-4800 SEM. Optical transmittance was measured with a Perkin Elmer Lambda 900 UV/VIS/NIR spectrophotometer and sheet resistance was measured with a four-point probe. X-ray photoelectron spectroscopy (XPS) and ultraviolet photoelectron spectroscopy (UPS) were performed at high vacuum ($< 5 \times 10^{-10}$ Torr) with a Kratos Ultra spectrometer, using Al Kα ($h\nu$ = 1486.71 eV) and He I ($h\nu$ = 21.21 eV) radiation sources, respectively. A 10 min air plasma clean was performed prior to analysis to replicate OPV device fabrication conditions. X-ray diffraction (XRD) data was collected by Michael Fleischauer using a Bruker D8 diffractometer equipped with a Cu source and area detector, calibrated against a silver behenate reference standard.

7.3. Results and Discussion

7.3.1. Nanopillar ITO formation

The most uniform morphology of 20 ~ 30 nm diameter ITO nanopillars was achieved by etching commercial ITO samples with Ar plasma at 190 mTorr and 220 W. To illustrate the evolution of ITO nanopillars as they are formed, structured films were made using etch times of 5 min, 10 min, and 20 min (see Figure 7.3). In this case, 9 samples were present during the 5 min etch, 6 remained for the following 5 min etch, and 3 remained for the final 10 min etch. As such, the 10 min sample saw one interruption during etching

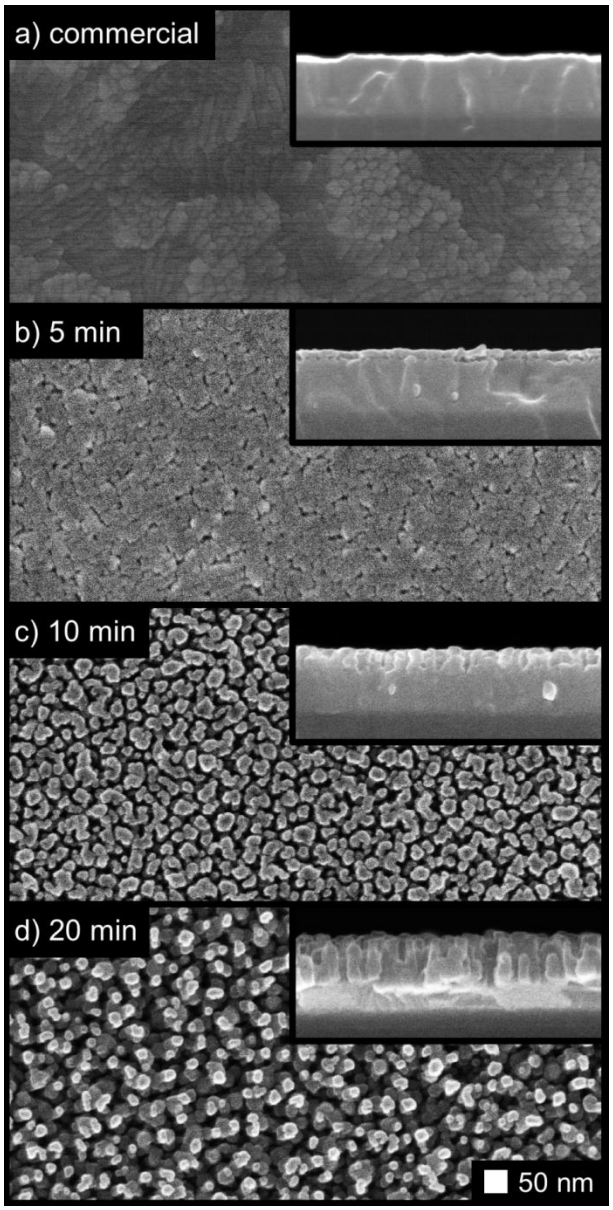

Figure 7.3 SEM images of a) the original commercial ITO film, and b-d) the nanopillar ITO films with different etch times (denoted in the image).

and the 20 min sample saw two. During each interruption, the venting of the chamber exposed samples to the ambient, and the re-ignition and stabilization of the plasma was required, which may reduce the average etch rate compared to a continuous etching process. Additionally, interrupting the etch process may limit the temperature increases experienced by the samples.

At the 5 min mark, only a slight removal of material at grain boundaries is observed, while further etching reveals thinner columns with increased spacing and porosity, as seen in Figure 7.3. Film morphology was consistent across all samples present in the etch chamber, except for areas within ≤ 5 mm of the sample edge, where extra etching was evident. The extent of the edge effects was consistent, regardless of the number of samples in the etch chamber, which indicates that they are an artifact of the substrate edge and not the edge of the plasma. The number of samples in the etch chamber did, however, affect the bias voltage (addressed further in Appendix A). Along with the effects of interrupting the plasma periodically to remove samples, this could provide a noticeable difference in the morphologies in Figure 7.3 compared to if they had been etched continuously.

Etched ITO samples typically appeared brown and cloudy; the longer the etch time, the more opaque the samples became. In addition, their sheet resistance increased as well. The recovery of optical transparency and electrical conductivity is discussed in the following section.

7.3.2. Optical and electrical properties

Both the optical transmittance and electrical conductivity were found to change substantially as a result of the etch process. The absorption of the film increased with etch time (see Figure 7.4), which is likely due to the preferential removal of oxygen, leaving a higher presence of metallic indium [307]. In the most severe case (20 min etch), the transmittance fell to 50% at 500 nm. Sheet resistance was also found to increase with etching (see Table 7.1), which may be caused by increased trapping of dopant entities at the grain boundaries [308]. This would occur if the ion bombardment from the plasma is damaging the crystal structure of the film; fortunately, this damage can be repaired by annealing.

Annealing at 500°C in air was used to recover the optical transmittance by oxidizing indium, which was followed by annealing at 375°C in 5% H_2 (balance Ar) to improve the electrical conductivity by repopulating the conduction band through the removal of excess oxygen [309]. Both of these

Table 7.1 Changes to the sheet resistance (R_s, Ω/□) of commercial and nanopillar ITO films due to etching, annealing, and cleaning processes. For the original commercials films, R_s = 13.0 ± 0.1. The relative surface composition of Sn and In is shown for the final processed film in each case, as well as the work function.

Etch time	R_s after etch	R_s after 1st anneal	R_s after 2nd anneal	R_s after plasma clean	Sn/In	Φ (eV)
commercial	-	65.5 ± 0.7	12.76 ± 0.07	13.10 ± 0.05	0.16 ± 0.02	4.47 ± 0.02
5 min	16.50 ± 0.05	75.9 ± 0.2	13.37 ± 0.09	13.46 ± 0.05	0.11 ± 0.03	4.50 ± 0.02
10 min	18.92 ± 0.02	75.7 ± 0.9	14.14 ± 0.05	14.46 ± 0.05	0.12 ± 0.03	4.60 ± 0.02
20 min	32.86 ± 0.09	76.8 ± 0.2	21.89 ± 0.09	22.25 ± 0.09	0.14 ± 0.04	4.52 ± 0.02

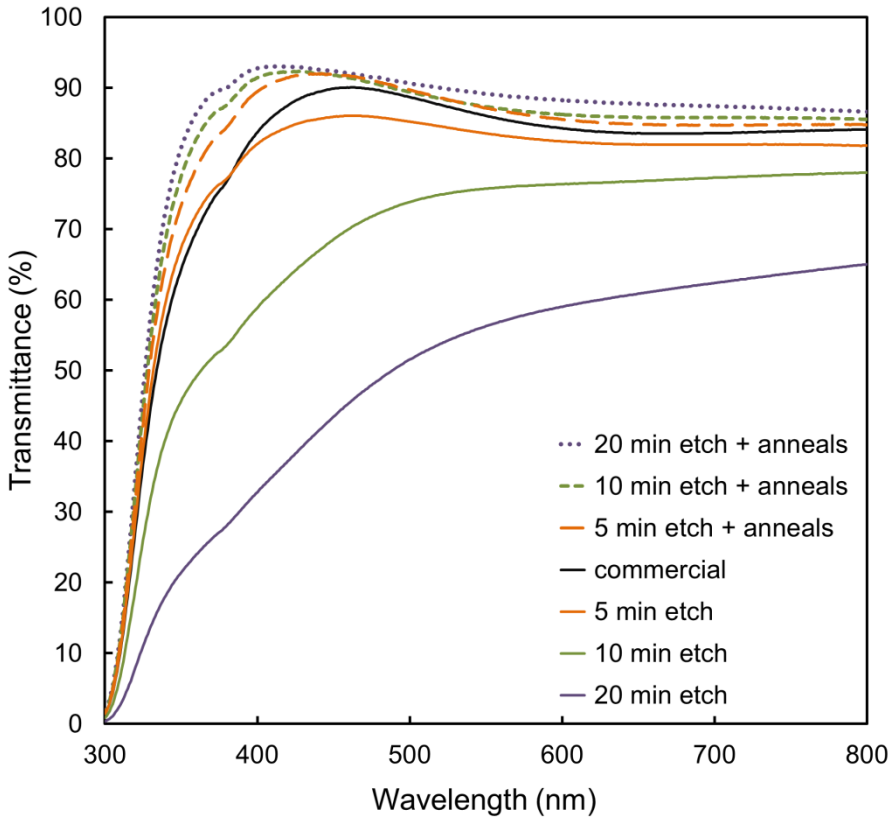

Figure 7.4 Transmittance spectra of nanopillar ITO films.

anneals contribute to improvement of film crystallinity, which increases conductivity by liberating donors from grain boundaries [308]. Morphology

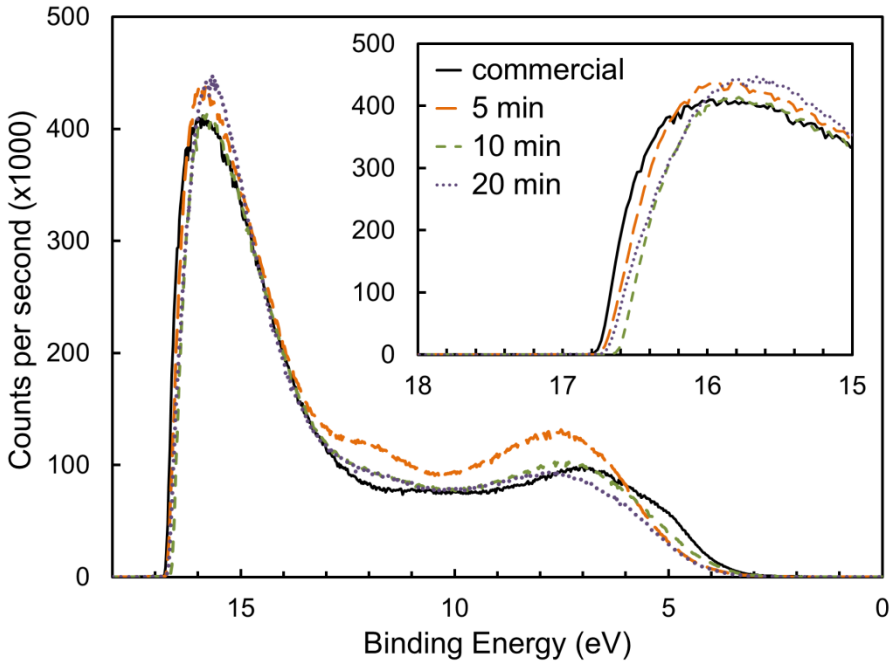

Figure 7.5 UPS spectra of nanopillar ITO films.

was monitored at each step and did not change (some examples are shown in Appendix B). The transmittance spectra for before and after the annealing stages are compared in Figure 7.4.

Remarkably, the 20 min etched sample recovers from being the least transparent to being the most transparent. In all cases, the etched films inherited anti-reflective properties compared to the commercial film, due to the loss of bulk material as well as a porous morphology, which lowers the refractive index. The final sheet resistance of the structured ITO films remained sufficiently low, as seen in Table 7.1. Though the 20 min etched sample remains more resistive than the rest, its strong lateral conductivity is remarkable considering it lost over half of its bulk thickness.

Changes to the films' surface stoichiometry were monitored with XPS, which was performed with an incident beam angle of 60° to focus on pillar tops and sides. Atomic concentrations were calculated using the relative peak intensities while accounting for the atomic sensitivity factors, and the ratio of Sn to In for each is presented in Table 7.1. Etching appeared to reduce Sn

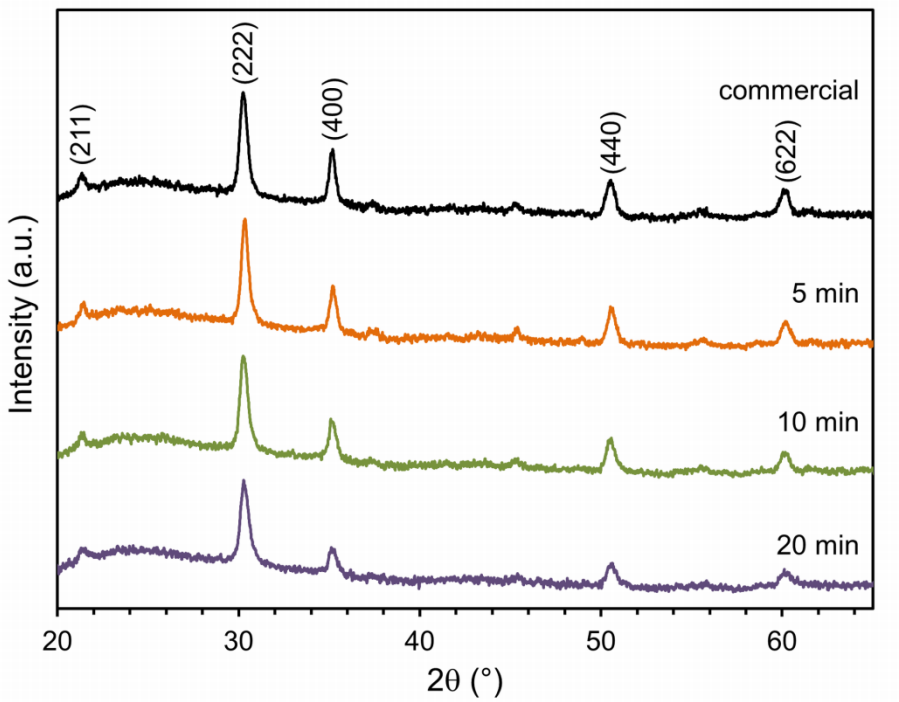

Figure 7.6 XRD data for annealed nanopillar ITO films.

content at the surface, though in all cases the surface stoichiometry is similar to previously published values [310]. The UPS spectra were measured (without breaking vacuum) to determine work function (Φ), and are shown in Figure 7.5. The work function values, listed in Table 7.1, show marginal variation and fall within the range of previously published values for ITO [310–312]. All of these films are therefore functionally suitable for use in optoelectronic devices.

7.3.3. Crystallinity analysis

The XRD spectra for the annealed nanopillar ITO films were collected and compared to that of the commercial film, as shown in Figure 7.6. According to the calibration routine, the peak positions are accurate to 0.29 ± 0.04°. The films maintain their crystallinity very well, which enables their recovered conductivity and further demonstrates their sustained suitability for optoelectronic devices. In particular, the 20 min etched film shows only slightly diminished peak heights, which is excellent considering how much of

the planar film has been removed.

7.3.4. Morphologies of different etch conditions

Nanopillar ITO films with vastly different morphologies were achieved by varying the etch conditions. Nanopillar diameter, spacing, and uniformity, as well as etch rate, were all determined by the chamber pressure and RF power used for etching. Some of these alternative film structures are presented in Figure 7.7. Nanopillar morphology is achieved in all cases, but more aggressive etching is achieved with higher power and pressure. The film restructuring is more dramatic in these cases, with pillar diameters becoming far greater than the average surface grain size (which can be seen in Figure 7.3a). For the films with narrow features (Figure 7.7c, 7.7d, and 7.3), preferential erosion of the grain boundaries is likely the primary mechanism for nanopillar formation, which is often used to explain surface texturing due to ion bombardment [246,313,314]. A certain amount of redeposition also occurs in these cases, however, as evidenced by the slight increase in film thickness. The etch mechanism is less clear for the films with larger pillars, but may be dominated by redeposition.

It is significant to note that the film in Figure 7.7c appears to have been etched slightly further than the one in Figure 7.3c, despite being etched under the same pressure and power for the same amount of time. This is partly attributed to the difference in substrate area present during etching, which affects the bias voltage, as mentioned previously. In these cases, two 1 inch substrates were placed adjacently in the etch chamber and etched for 10 continuous minutes (as opposed to the sequence performed for films in Figure 7.3). The different degree of etching may also be the result of interruptions to the etching of films in Figure 7.3. Again, the optical transmittance was measured at each processing stage, and is shown in Figure 7.8. The sheet resistances were measured after etching and after the two-stage annealing process, which are compared in Table 7.2. The data here shows similar trends to those above, where both transmittance and sheet resistance increase with the degree of etching.

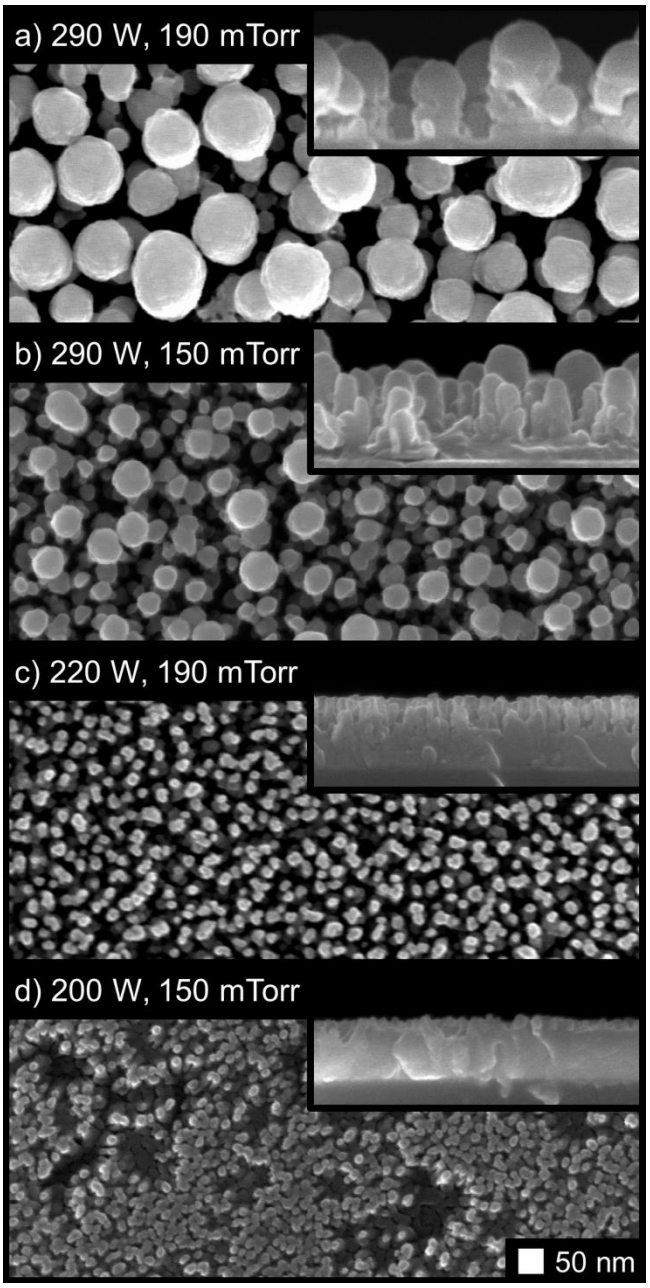

Figure 7.7 SEM images of various etched ITO films. The RF power and chamber pressure in each case were a) 290 W and 190 mTorr; b) 290 W and 150 mTorr; c) 220 W and 190 mTorr; and d) 200 W and 150 mTorr.

Table 7.2 Sheet resistance of various etched ITO films after etching and annealing stages.

Etch conditions	After etch (Ω/□)	After annealing (Ω/□)
290 W, 190 mTorr	$3.7 \pm 0.1 \times 10^3$	$2.1 \pm 0.2 \times 10^3$
290 W, 150 mTorr	216 ± 5	152 ± 7
220 W, 190 mTorr	21.1 ± 0.1	15.6 ± 0.1
200 W, 150 mTorr	20.4 ± 0.2	15.3 ± 0.1

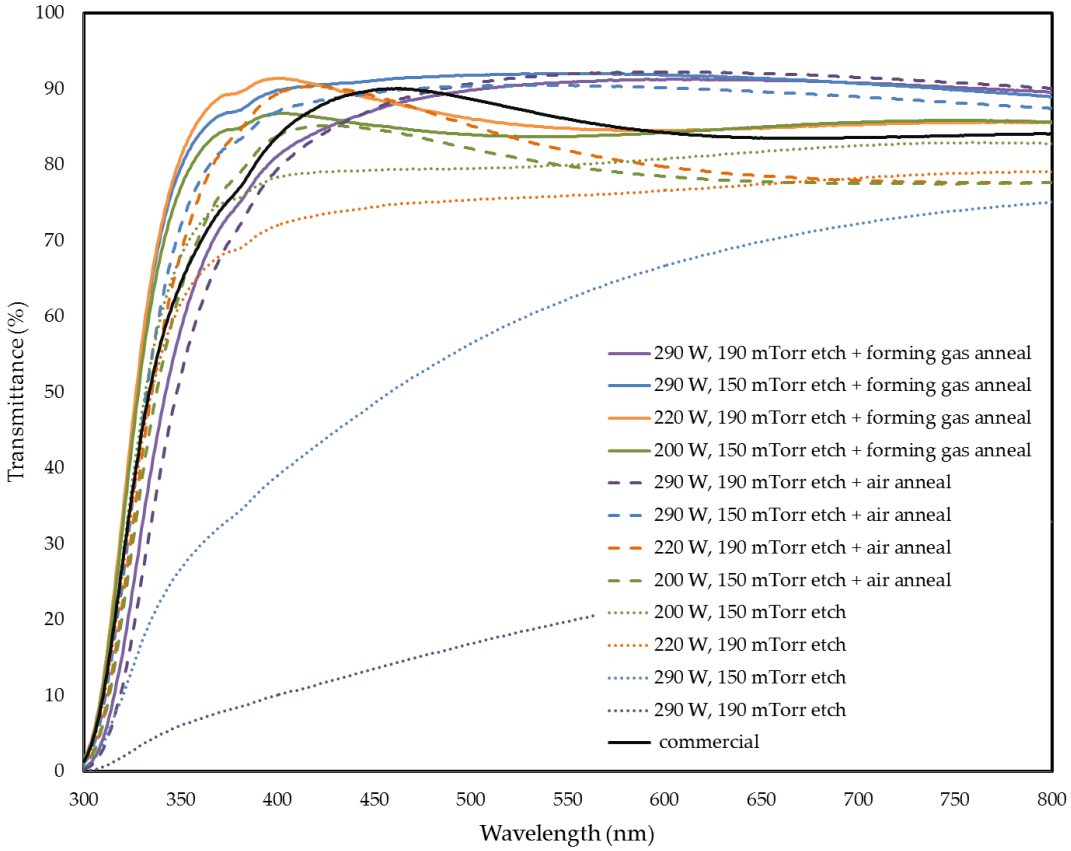

Figure 7.8 Transmittance of etched ITO films at different processing stages.

7.3.5. Etching thicker ITO films

Much thicker OPV devices require much thicker structured electrodes. Figure 7.9 shows some preliminary results from etching a 400 nm thick

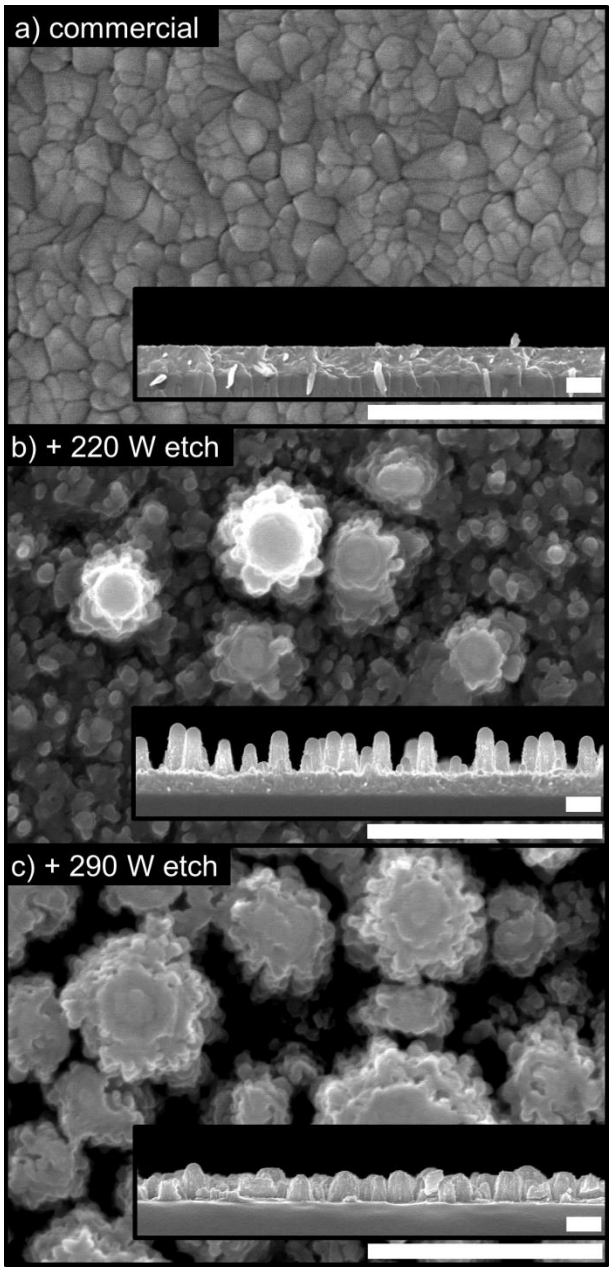

Figure 7.9 Aerial view SEM images of thick commercial and nanopillar ITO films (insets are side views). Scale bars are 500 nm.

commercial ITO film. Two different etches were performed, in which only the RF power was changed. The pressure was held at 190 mTorr with argon, as usual. Again, nanopillar structures are revealed in the etched films, with considerably larger column diameters. Interestingly, the bulk film thickness is

hardly changed in the 220 W etch case; meanwhile nanopillars grew up to 500 nm or more. This indicates a much more complex etch mechanism than simply sputter erosion. Re-deposition of material during etching is clearly evident. Though these structured ITO films are not yet optimized for OPV devices, they illustrate the great potential of the technique in yielding truly uniform, robust, columnar electrodes for OPV applications.

7.4. Summary

The preparation of nanostructured ITO thin films using argon plasma etching was shown. Nanopillar films are achieved with a variety of morphologies, as determined by the etch conditions and substrate area present during etching. These films exhibit excellent optical transmittance and electrical conductivity, which are accomplished by sequential annealing in air and forming gas. The morphologies and properties of these nanopillar films make them suitable for use in highly efficient optoelectronic devices, particularly OPVs. Conformal coating of these structured electrodes with either an interface material for polymer devices, or a small molecule donor layer for molecular devices, is necessary for successful device integration. Work in this area is ongoing. In addition, the results in this chapter warrant further work on plasma etching of metal oxide thin films for applications in other areas, such as batteries, fuel cells, sensors, and anti-reflective coatings.

8. CONCLUSIONS

8.1. Summary of Thesis Results

This thesis outlines several new methods that may be used to achieve structured, ordered heterojunctions in organic photovoltaic (OPV) devices for improved photoconversion efficiency. Control over donor layer morphology is demonstrated by using glancing angle deposition, block copolymer surface patterning, solvent recrystallization, and argon plasma etching. A structured electrode is also presented, which gives rise to completely different OPV device architecture possibilities.

8.1.1. GLAD MPc thin films and OPV devices

A large variety of metal phthalocyanine (MPc) film morphologies were achieved using the glancing angle deposition (GLAD) technique. As with many other organic materials, the increased surface diffusion of molecules encouraged a high degree of column broadening. This was mitigated by use of ϕ-sweep substrate motion during deposition, which enabled the fabrication of very uniform slanted post film morphologies. Average column diameters of around 40 ~ 50 nm were maintained while growing films even far beyond the ideal 200 nm thickness.

Integrating GLAD MPc layers into OPV devices required filling with an organic acceptor material. The most effective route to filling is with solution casting, which presented challenges regarding the effects of solvents on the MPc layer. Several solvents were evaluated for this purpose, most of which were found to significantly recrystallize the MPc material upon direct exposure with the film. Significant changes to the films' properties were observed as a result, from both an absorbance and a crystallinity perspective. The recrystallized films exhibited resilience to further morphology changes when coated with PCBM in chlorobenzene (CB), suggesting that this solvent is less able to act on the MPc layer when loaded with PCBM. Furthermore,

analysis with SIMS was used to confirm that the bilayer architecture is preserved when coating a planar ZnPc film with PCBM in CB. A distinct region of Zn was observed well below the active layer surface in this case. However, somewhat of a mixed heterojunction was seen when using dichlorobenzene (DCB) as the PCBM solvent in the same scenario. In this case, Zn was not only observed throughout the entire active layer, it was even present at the surface. Surprisingly, this result turned out to be beneficial for device operation.

The optimization of a bilayer OPV device was performed, which served as the foundation for identifying performance improvements due to nanostructuring. Film thicknesses were each optimized, and the effects of ambient exposure were identified to minimize device degradation prior to testing. While PEDOT:PSS and MPc films survived well in atmospheric conditions, the PCBM layer degraded rapidly when exposed to oxygen. Such exposure was therefore minimized during processing. Incorporating an exciton blocking layer at the cathode was able to improve device performance substantially, by alleviating damage to the active layer during the metal deposition. The purity of the MPc source materials was also found to be a critical factor affecting performance. Despite the various sensitivities observed for these devices, careful control of these factors enabled the effects of nanostructuring to be observed and evaluated.

The optimization of a ZnPc/PCBM active layer involved a balance of solvent effects and nanostructuring via GLAD. Photoconversion efficiencies of up to 3.0% were seen for devices made with a thin structured ZnPc layer when DCB was used as the PCBM solvent. These devices achieved an average efficiency of 2.86%, which compared well with the 2.3% result seen by both bilayer devices using the same solvent, and structured devices made using CB as the PCBM solvent. Despite the significantly higher absorption of thicker structured ZnPc films, only a marginal improvement in photocurrent was seen in these thicker devices, and the overall performance decreased. This suggests that the columnar dimensions in these films are still too much larger than the exciton diffusion length for their structure to be fully utilized.

The solvent-recrystallized films performed poorly in OPV devices, presumably due to the modifications in film composition that resulted from solvent exposure.

In conclusion, nanostructuring via GLAD has shown to improve the photoconversion efficiency of small molecule OPV devices. Substantial further improvements are still possible with this approach, if the exciton diffusion length and columnar film feature diameters can further approach one another.

8.1.2. Seeded GLAD MPc thin films

Increased order in GLAD films was demonstrated through the use of seeded substrates. Columnar films with the most relevant dimensions were obtained by using block copolymer substrate seeding techniques, which enabled the column spacing to be varied between 40 and 60 nm. Perfect adherence to the surface patterns enabled periodic columnar arrays of ZnPc to be fabricated on Si surfaces. The degree of consistency achieved here, regarding column diameter and spacing, surpasses that seen with any other technique used to deposit MPc materials thus far.

When grown to thicknesses much greater than the seed spacing, these seeded films deviate from the original pattern. Nevertheless, column diameters are reduced by using seeded substrates, and the column densities of seeded films are much higher than those grown on bare surfaces. Both of these characteristics would be advantageous in a device context, provided the seeding could occur in a manner compatible with device fabrication. Seeded ITO surfaces were demonstrated, and the fabrication of SiO_2 seed patterns on Si was performed as well. These achievements provide an avenue for device-compatible seeding processes, but further work is needed for complete device integration.

8.1.3. Ion bombarded MPc films

One of the most unforeseen events over the course of the work in the thesis was the formation of vertically aligned nanopillar films that resulted

from etching planar films with argon plasma. The dimensions of the film features seen here are extremely well-suited to the short exciton diffusion lengths in MPc materials. Additionally, the columnar geometries in this case appear to be more structurally robust than those grown with GLAD. A significant amount of MPc material remains in the film, as evidenced by well-maintained absorbance profiles. Upon further analysis, however, significant changes to the surface stoichiometry were seen, indicating a thin layer of surface damage overlaying the film. This damaged surface translates into a non-functioning active layer interface when used in an OPV device, where no photocurrent is seen. Nevertheless, MPc molecules are known to be resilient against fragmentation when subject to impacts of tens of eV. Therefore, by use of other ion energies or chemistries, undamaging ion-induced MPc film structuring may yet be possible, which poses intriguing possibilities for small molecule OPV devices.

8.1.4. Nanopillar ITO via Ar plasma

Argon plasma etching was capable of inducing morphology changes in ITO films as well. Nanopillar ITO films were created out of commercial ones by the same means as MPc etching, but with longer etch times. In these cases, however, many more film varieties were possible and film properties could be recovered. Nanopillar diameters ranged from tens to hundreds of nanometers, and the variation in possible pillar heights was even greater.

Fortunately, the ion-induced damage to these films could be reversed by means of a two-stage annealing process in air and forming gas. Whereas etching left the films rather opaque, the annealed films showed even greater transmittance than the original commercial film. The surface texturing acts as an anti-reflection coating as a result of its lower index of refraction. Similarly, though the sheet resistance increased dramatically as a result of etching, it was nearly recovered in the annealed films despite reductions in the bulk layer thickness. Finally, the work function of the nanopillar ITO films closely matched that of the original commercial film. Therefore, these nanopillar ITO films maintain their suitability for use in optoelectronic devices, and thereby

provide a compelling approach to preparing and utilizing nanostructured electrodes at a manufacturing scale. The platform established here may be developed further for applications in a variety of areas, including organic solar cells, batteries, fuel cells, sensors, and anti-reflection coatings.

8.2. Future Work

8.2.1. GLAD MPc thin films and OPV devices

Further improvements to GLAD-structured donor layers in OPV devices are still possible if the columnar diameters in these films can be further constrained. It is well known that surface treatments can be used to encourage different molecular orientations of MPc films as they grow; perhaps these same treatments would also yield different GLAD film morphologies, preferably with thinner columns and tighter spacing.

A more comprehensive survey of GLAD small molecule films would yield further insight into the benefits imposed by nanostructuring. A comparison between materials with different exciton diffusion lengths and charge carrier mobilities may help to identify the required combination of parameters that would enable fully optimized GLAD structured devices. Materials with high exciton lifetimes are desired most; if any such materials emerge, they should be targeted first for structuring with GLAD.

The recrystallization effects of organic solvents on MPc films open up a variety of future possibilities. Further work with different PCBM solvents and concentrations may lead to increased control over the degree of material mixing at the interface. New acceptor materials could also be pursued in order to achieve a pristine interdigitated device. Materials that can be cast using solvents that do not dissolve the MPc layer would be preferred.

By eliminating the exposure of PCBM films to oxygen prior to testing, degradation could be minimized, and better performance would be observed. Any efforts here should keep in mind that MPc films may not benefit from completely inert environments; oxygen exposure may be necessary here, prior to PCBM application.

8.2.2. Seeded GLAD MPc thin films

Many of the film morphologies achieved with block copolymer substrate seeding are already very appealing from an OPV device perspective. Integration into devices requires further optimization of the ITO surface seeding process to incorporate the SiO_2 seeds already accomplished on Si. Conveniently, the surface seeding process ends with an oxygen plasma cleaning stage, which is the first stage of device fabrication. Currently, the optimized plasma conditions for these processes are different, which must be reconciled for successful device fabrication. These issues are fundamentally solvable and devices incorporating seeded MPc layers should be possible.

8.2.3. Ion bombarded MPc films

The surface damage imposed by argon plasma on MPc films is severe. So far, however, only a few variations of the etch process have been performed. The possibility for damage-free ion-induced structuring of these films, via different ion energies and etch chemistries, remains. Depending on the extent of the damage, repairing the surface via annealing may be possible. Additional experiments and analysis will reveal whether catastrophic surface damage is fundamentally preventable, repairable, or neither.

8.2.4. Nanopillar ITO via Ar plasma

The outstanding morphologies and properties of nanopillar ITO films shown in this thesis warrant the most immediate attention of future investigators. Two key achievements remain here that would enable improved polymer OPV devices. Firstly, a better understanding of the etching and growth mechanisms in the thicker ITO films is necessary, to enable the superb nanopillar dimensions observed in thinner films to extend into much thicker ones. Secondly, the development of a surface treatment or interface layer that replaces PEDOT:PSS is necessary. This layer or treatment must maintain the morphology of the structured electrode while facilitating hole transport out of the active layer. New surface treatments to eliminate the

PEDOT:PSS layer are a current topic of great interest; attention must be paid here to identify any that would be suitable to a structured electrode. Again, in this case the challenges are fundamentally solvable, and the possibilities posed by doing so are compelling.

8.3. Final remarks

The goal of this thesis was to demonstrate the formation of small molecule thin films with nanoscale morphologies designed specifically for OPV devices. This has been achieved by employing a variety of nanofabrication techniques, and improvements in device performance were achieved as a result. Many unexpected phenomena were encountered as a result of these endeavours, which provide new and exciting possibilities for further OPV device improvements. With the appropriate balance of skill and luck, further development of these device designs may contribute to the bright outlook for organic solar systems, and ultimately the design of new energy infrastructure less dependent on fossil fuels.

REFERENCES

[1] J. Newton, *Uncommon Friends: Life with Thomas Edison, Henry Ford, Harvey Firestone, Alexis Carrel, and Charles Lindbergh*, p. 31, Harcourt Brace Jovanovich, San Diego, CA (1989).

[2] J. H. Werner, "Second and Third Generation Photovoltaics – Dreams and Reality," *Adv. Solid State Phys.* **44**, 51–67 (2004).

[3] S. E. Shaheen, D. S. Ginley, and G. E. Jabbour, "Organic-Based Photovoltaics: Toward Low-Cost Power Generation," *MRS Bulletin* **30**, 10–19 (2005).

[4] T. Ameri, G. Dennler, C. Lungenschmied, and C. J. Brabec, "Organic tandem solar cells: A review," *Energy Environ. Sci.* **2**, 347–363 (2009).

[5] SBI Energy Market Report, "U.S. Solar Energy Market World Data," Rockville, MD (2010).

[6] SBI Energy Market Report, "Global Solar Inverter Markets," Rockville, MD (2011).

[7] S. Lizin, S. Van Passel, E. De Schepper, and L. Vranken, "The future of organic photovoltaic solar cells as a direct power source for consumer electronics," *Sol. Energy Mater. Sol. Cells* **103**, 1–10 (2012).

[8] C. Wadia, A. P. Alivisatos, and D. M. Kammen, "Materials Availability Expands the Opportunity for Large-Scale Photovoltaics Deployment," *Environ. Sci. Technol.* **43**, 2072–2077 (2009).

[9] R. R. King, D. C. Law, K. M. Edmondson, C. M. Fetzer, G. S. Kinsey, H. Yoon, R. A. Sherif, and N. H. Karam, "40% efficient metamorphic GaInP/GaInAs/Ge multijunction solar cells," *Appl. Phys. Lett.* **90**, 183516 (2007).

[10] M. Green, K. Emery, Y. Hishikawa, W. Warta, and E. D. Dunlop, "Solar cell efficiency tables (version 39)," *Prog. Photovolt: Res. Appl.* **20**, 12–20 (2012).

[11] A. Shah, P. Torres, R. Tscharner, N. Wyrsch, and H. Keppner, "Photovoltaic Technology: The Case for Thin-Film Solar Cells," *Science* **285**, 692–698 (1999).

[12] M. A. Green, "Learning experience for thin-film solar modules: First Solar, Inc. case study," *Prog. Photovolt: Res. Appl.* **19**, 498–500 (2011).

[13] D. Eaglesham, "Innovation in Solar Technologies," *World Future Energy Summit*, Abu Dhabi, UAE (2012).

[14] C. Tang, "Two-layer organic photovoltaic cell," *Appl. Phys. Lett.* **48**, 183–185 (1986).

[15] J. Y. Kim, K. Lee, N. E. Coates, D. Moses, T.-Q. Nguyen, M. Dante, and A. J. Heeger, "Efficient tandem polymer solar cells fabricated by all-solution processing," *Science* **317**, 222–225 (2007).

[16] S. H. Park, A. Roy, S. Beaupré, S. Cho, N. Coates, J. S. Moon, D. Moses, M. Leclerc, K. Lee, et al., "Bulk heterojunction solar cells with internal quantum efficiency approaching 100%," *Nat. Photonics* **3**, 297–303 (2009).

[17] H.-Y. Chen, J. Hou, S. Zhang, Y. Liang, G. Yang, Y. Yang, L. Yu, Y. Wu, and G. Li, "Polymer solar cells with enhanced open-circuit voltage and efficiency," *Nat. Photonics* **3**, 649–653 (2009).

[18] T. D. Nielsen, C. Cruickshank, S. Foged, J. Thorsen, and F. C. Krebs, "Business, market and intellectual property analysis of polymer solar cells," *Sol. Energy Mater. Sol. Cells* **94**, 1553–1571 (2010).

[19] L. Dou, J. You, J. Yang, C.-C. Chen, Y. He, S. Murase, T. Moriarty, K. Emery, G. Li, et al., "Tandem polymer solar cells featuring a spectrally matched low-bandgap polymer," *Nat. Photonics* **6**, 180–185 (2012).

[20] G. Li, R. Zhu, and Y. Yang, "Polymer solar cells," *Nat. Photonics* **6**, 153–161 (2012).

[21] M. Riede, C. Uhrich, J. Widmer, R. Timmreck, D. Wynands, G. Schwartz, W.-M. Gnehr, D. Hildebrandt, A. Weiss, et al., "Efficient Organic Tandem Solar Cells based on Small Molecules," *Adv. Funct. Mater.* **21**, 3019–3028 (2011).

[22] R. F. Service, "Outlook Brightens for Plastic Solar Cells," *Science* **332**, 293 (2011).

[23] C. J. Brabec, "Organic photovoltaics: technology and market," *Sol. Energy Mater. Sol. Cells* **83**, 273–292 (2004).

[24] S. R. Forrest, "The path to ubiquitous and low-cost organic electronic appliances on plastic," *Nature* **428**, 911–918 (2004).

[25] D. J. Gundlach, "Low power, high impact," *Nat. Mater.* **6**, 173–174 (2007).

[26] N. Stingelin-Stutzmann, "Complexity made simple," *Nat. Mater.* **7**, 171–172 (2008).

[27] T. Sekitani, U. Zschieschang, H. Klauk, and T. Someya, "Flexible organic transistors and circuits with extreme bending stability," *Nat. Mater.* **9**, 1015–1022 (2010).

[28] M. Kaltenbrunner, M. S. White, E. D. Głowacki, T. Sekitani, T. Someya, N. S. Sariciftci, and S. Bauer, "Ultrathin and lightweight organic solar cells with high flexibility," *Nat. Commun.* **3**, 770 (2012).

[29] M. Jørgensen, K. Norrman, S. A. Gevorgyan, T. Tromholt, B. Andreasen, and F. C. Krebs, "Stability of polymer solar cells.," *Adv. Mater.* **24**, 580–612 (2012).

[30] C. J. Brabec, S. Gowrisanker, J. J. M. Halls, D. Laird, S. Jia, and S. P. Williams, "Polymer-Fullerene Bulk-Heterojunction Solar Cells," *Adv. Mater.* **22**, 3839–3856 (2010).

[31] K. Mikaye, Y. Uetani, T. Seike, T. Kato, K. Oya, K. Yoshimura, and T. Ohnishi, "Development of Next Generation Organic Solar Cell," *R&D Report, "SUMITOMO KAGAKU"* **2010-I**, 1–12 (2010).

[32] F. C. Krebs, J. Fyenbo, and M. Jørgensen, "Product integration of compact roll-to roll processed polymer solar cell modules: methods and manufacture using flexographic printing, slot-die coating and rotary screen printing," *J. Mater. Chem.* **20**, 8994–9001 (2010).

[33] G. A. Rivière, J.-J. Simon, L. Escoubas, W. Vervisch, and M. Pasquinelli, "Photo-electrical characterizations of plastic solar modules," *Sol. Energy Mater. Sol. Cells* **102**, 19–25 (2012).

[34] M. Jørgensen, K. Norrman, and F. C. Krebs, "Stability/degradation of polymer solar cells," *Sol. Energy Mater. Sol. Cells* **92**, 686–714 (2008).

[35] M. Hermenau, M. Riede, K. Leo, S. A. Gevorgyan, F. C. Krebs, and K. Norrman, "Water and oxygen induced degradation of small molecule organic solar cells," *Sol. Energy Mater. Sol. Cells* **95**, 1268–1277 (2011).

[36] M. Hermenau, S. Schubert, H. Klumbies, J. Fahlteich, L. Müller-Meskamp, K. Leo, and M. Riede, "The effect of barrier performance on the lifetime of small-molecule organic solar cells," *Sol. Energy Mater. Sol. Cells* **97**, 102–108 (2012).

[37] J. A. Hauch, P. Schilinsky, S. A. Choulis, R. Childers, M. Biele, and C. J. Brabec, "Flexible organic P3HT:PCBM bulk-heterojunction modules with more than 1 year outdoor lifetime," *Sol. Energy Mater. Sol. Cells* **92**, 727–731 (2008).

[38] C. H. Peters, I. T. Sachs-Quintana, J. P. Kastrop, S. Beaupré, M. Leclerc, and M. D. McGehee, "High Efficiency Polymer Solar Cells with Long Operating Lifetimes," *Adv. Energy Mater.* **1**, 491–494 (2011).

[39] R. Franke, B. Maennig, A. Petrich, and M. Pfeiffer, "Long-term stability of tandem solar cells containing small organic molecules," *Sol. Energy Mater. Sol. Cells* **92**, 732–735 (2008).

[40] N. Kim, W. J. Potscavage, A. Sundaramoothi, C. Henderson, B. Kippelen, and S. Graham, "A correlation study between barrier film performance and shelf lifetime of encapsulated organic solar cells," *Sol. Energy Mater. Sol. Cells* **101**, 140–146 (2012).

[41] W. J. Potscavage, S. Yoo, B. Domercq, and B. Kippelen, "Encapsulation of pentacene/C60 organic solar cells with Al2O3 deposited by atomic layer deposition," *Appl. Phys. Lett.* **90**, 253511 (2007).

[42] C. H. Peters, "Lifetime and Reliability of Polymer Solar Cells," PhD Thesis, Materials Science and Engineering, Stanford University (2011).

[43] www.heliatek.com, "Press release: Heliatek sets new world record efficiency of 10.7 % for its organic tandem cell," accessed April 27, 2012.

[44] www.heliatek.com, "Small molecules with a big impact," accessed April 27, 2012.

[45] M. Riede, "Small-molecule organic solar cells employing novel materials," *SPIE Optics+Photonics*, 8116–02, San Diego, CA, USA (2011).

[46] H. Shirakawa, E. J. Louis, A. G. MacDiarmid, C. K. Chiang, and A. J. Heeger, "Synthesis of electrically conducting organic polymers: halogen derivatives of polyacetylene, (CH)x," *J. Chem. Soc., Chem. Commun.*, 578–580 (1977).

[47] C. W. Tang and S. A. VanSlyke, "Organic electroluminescent diodes," *Appl. Phys. Lett.* **51**, 913–915 (1987).

[48] J. H. Burroughes, D. D. C. Bradley, A. R. Brown, R. N. Marks, K. Mackay, R. H. Friend, P. L. Burns, and A. B. Holmes, "Light-emitting diodes based on conjugated polymers," *Nature* **347**, 539–541 (1990).

[49] N. S. Sariciftci, L. Smilowitz, A. J. Heeger, and F. Wudl, "Photoinduced electron transfer from a conducting polymer to buckminsterfullerene," *Science* **258**, 1474–1476 (1992).

[50] W. Ma, C. Yang, X. Gong, K. Lee, and A. J. Heeger, "Thermally Stable, Efficient Polymer Solar Cells with Nanoscale Control of the Interpenetrating Network Morphology," *Adv. Funct. Mater.* **15**, 1617–1622 (2005).

[51] S. Aramaki, "Solution-Processible Crystalline Organic Semiconductors for Photovoltaic Application," *2011 MRS Fall*, H8.6, Boston, MA, USA (2011).

[52] B. A. Gregg, "The Photoconversion Mechanism of Excitonic Solar Cells," *MRS Bulletin* **30**, 20–22 (2005).

[53] G. D. Scholes and G. Rumbles, "Excitons in nanoscale systems," *Nat. Mater.* **5**, 683–696 (2006).

[54] M. Knupfer, "Exciton binding energies in organic semiconductors," *Appl. Phys. A* **77**, 623–626 (2003).

[55] B. A. Gregg, "Excitonic Solar Cells," *J. Phys. Chem. B* **107**, 4688–4698 (2003).

[56] J. G. Van Dijken, M. D. Fleischauer, and M. J. Brett, "Morphology control of CuPc thin films using Glancing Angle Deposition," in *Proc. 33rd IEEE Photov. Spec. Conf.*, pp. 1222–1225 (2008).

[57] S. R. Forrest, "The Limits to Organic Photovoltaic Cell Efficiency," *MRS Bulletin* **30**, 28–32 (2005).

[58] P. Peumans, V. Bulović, and S. R. Forrest, "Efficient photon harvesting at high optical intensities in ultrathin organic double-heterostructure photovoltaic diodes," *Appl. Phys. Lett.* **76**, 2650–2652 (2000).

[59] C. Zhang, S. W. Tong, C. Jiang, E. T. Kang, D. S. H. Chan, and C. Zhu, "Simple tandem organic photovoltaic cells for improved energy conversion efficiency," *Appl. Phys. Lett.* **92**, 083310 (2008).

[60] C. Zhang, S. W. Tong, C. Jiang, E. T. Kang, D. S. H. Chan, and C. Zhu, "Efficient multilayer organic solar cells using the optical interference peak," *Appl. Phys. Lett.* **93**, 043307 (2008).

[61] J. Xue, S. Uchida, B. P. Rand, and S. R. Forrest, "Asymmetric tandem organic photovoltaic cells with hybrid planar-mixed molecular heterojunctions," *Appl. Phys. Lett.* **85**, 5757 (2004).

[62] B. Azzopardi, C. J. M. Emmott, A. Urbina, F. C. Krebs, J. Mutale, and J. Nelson, "Economic assessment of solar electricity production from organic-based photovoltaic modules in a domestic environment," *Energy Environ. Sci.* **4**, 3741–3753 (2011).

[63] R. I. Gearba, T. Mills, J. Morris, R. Pindak, C. T. Black, and X. Zhu, "Quantifying Interfacial Electric Fields and Local Crystallinity in Polymer-Fullerene Bulk-Heterojunction Solar Cells," *Adv. Funct. Mater.* **21**, 2666–2673 (2011).

[64] P. Peumans and S. R. Forrest, "Separation of geminate charge-pairs at donor–acceptor interfaces in disordered solids," *Chem. Phys. Lett.* **398**, 27–31 (2004).

[65] J.-L. Brédas, D. Beljonne, V. Coropceanu, and J. Cornil, "Charge-transfer and energy-transfer processes in pi-conjugated oligomers and polymers: a molecular picture," *Chem. Rev.* **104**, 4971–5004 (2004).

[66] M. C. Scharber, D. Mühlbacher, M. Koppe, P. Denk, C. Waldauf, A. J. Heeger, and C. J. Brabec, "Design Rules for Donors in Bulk-Heterojunction Solar Cells—Towards 10 % Energy-Conversion Efficiency," *Adv. Mater.* **18**, 789–794 (2006).

[67] G. Dennler, M. C. Scharber, T. Ameri, P. Denk, K. Forberich, C. Waldauf, and C. J. Brabec, "Design Rules for Donors in Bulk-Heterojunction Tandem Solar Cells-Towards 15 % Energy-Conversion Efficiency," *Adv. Mater.* **20**, 579–583 (2008).

[68] S. E. Gledhill, B. Scott, and B. A. Gregg, "Organic and nano-structured composite photovoltaics: An overview," *J. Mater. Res.* **20**, 3167–3179 (2005).

[69] B. Rand, D. Burk, and S. Forrest, "Offset energies at organic semiconductor heterojunctions and their influence on the open-circuit voltage of thin-film solar cells," *Phys. Rev. B* **75**, 1–11 (2007).

[70] W. Shockley and H. J. Queisser, "Detailed Balance Limit of Efficiency of p-n Junction Solar Cells," *J. Appl. Phys.* **32**, 510–519 (1961).

[71] T. Trupke, M. A. Green, and P. Würfel, "Improving solar cell efficiencies by up-conversion of sub-band-gap light," *J. Appl. Phys.* **92**, 4117–4122 (2002).

[72] Y. Terao, H. Sasabe, and C. Adachi, "Correlation of hole mobility, exciton diffusion length, and solar cell characteristics in phthalocyanine/fullerene organic solar cells," *Appl. Phys. Lett.* **90**, 103515 (2007).

[73] F. Yang and S. R. Forrest, "Photocurrent generation in nanostructured organic solar cells," *ACS Nano* **2**, 1022–1032 (2008).

[74] P. Peumans, A. Yakimov, and S. R. Forrest, "Small molecular weight organic thin-film photodetectors and solar cells," *J. Appl. Phys.* **93**, 3693–3723 (2003).

[75] B. P. Rand, J. Genoe, P. Heremans, and J. Poortmans, "Solar Cells Utilizing Small Molecular Weight Organic Semiconductors," *Prog. Photovolt: Res. Appl.* **15**, 659–676 (2007).

[76] R. R. Lunt, N. C. Giebink, A. A. Belak, J. B. Benziger, and S. R. Forrest, "Exciton diffusion lengths of organic semiconductor thin films measured by spectrally resolved photoluminescence quenching," *J. Appl. Phys.* **105**, 053711 (2009).

[77] K. J. Bergemann and S. R. Forrest, "Measurement of exciton diffusion lengths in optically thin organic films," *Appl. Phys. Lett.* **99**, 243303 (2011).

[78] H. Gommans, S. Schols, A. Kadashchuk, and P. Heremans, "Exciton Diffusion Length and Lifetime in Subphthalocyanine Films," *J. Phys. Chem. C* **113**, 2974–2979 (2009).

[79] R. R. Lunt, J. B. Benziger, and S. R. Forrest, "Relationship between crystalline order and exciton diffusion length in molecular organic semiconductors," *Adv. Mater.* **22**, 1233–1236 (2010).

[80] B. A. Gregg, "Evolution of Photophysical and Photovoltaic Properties of Perylene Bis(phenethylimide) Films upon Solvent Vapor Annealing," *J. Phys. Chem.* **100**, 852–859 (1996).

[81] V. D. Mihailetchi, H. X. Xie, B. de Boer, L. J. A. Koster, and P. W. M. Blom, "Charge Transport and Photocurrent Generation in Poly(3-hexylthiophene):

Methanofullerene Bulk-Heterojunction Solar Cells," *Adv. Funct. Mater.* **16**, 699–708 (2006).

[82] B. P. Rand, J. Xue, S. Uchida, and S. R. Forrest, "Mixed donor-acceptor molecular heterojunctions for photovoltaic applications. I. Material properties," *J. Appl. Phys.* **98**, 124902 (2005).

[83] N. Karl, K.-H. Kraft, J. Marktanner, M. Munch, F. Schatz, R. Stehle, and H.-M. Uhde, "Fast electronic transport in organic molecular solids?," *J. Vac. Sci. Technol. A* **17**, 2318–2328 (1999).

[84] A. Opitz, M. Bronner, and W. Brütting, "Ambipolar charge carrier transport in mixed organic layers of phthalocyanine and fullerene," *J. Appl. Phys.* **101**, 063709 (2007).

[85] R. F. Salzman, J. Xue, B. P. Rand, A. Alexander, M. E. Thompson, and S. R. Forrest, "The effects of copper phthalocyanine purity on organic solar cell performance," *Org. Electron.* **6**, 242–246 (2005).

[86] J. Xue, B. P. Rand, S. Uchida, and S. R. Forrest, "A Hybrid Planar-Mixed Molecular Heterojunction Photovoltaic Cell," *Adv. Mater.* **17**, 66–71 (2005).

[87] S. S. Mali, D. S. Dalavi, P. N. Bhosale, C. A. Betty, A. K. Chauhan, and P. S. Patil, "Electro-optical properties of copper phthalocyanines (CuPc) vacuum deposited thin films," *RSC Adv.* **2**, 2100–2104 (2012).

[88] S. Karan and B. Mallik, "Effects of annealing on the morphology and optical property of copper (II) phthalocyanine nanostructured thin films," *Solid State Commun.* **143**, 289–294 (2007).

[89] T. Misra, "A comparative study of theoretical and experimental results on davydov splitting in molecular crystals," *Rev. Pur. Appl. Chem.* **15**, 39 (1965).

[90] F. Yang, M. Shtein, and S. R. Forrest, "Controlled growth of a molecular bulk heterojunction photovoltaic cell," *Nat. Mater.* **4**, 37–41 (2005).

[91] T. Stübinger and W. Brütting, "Exciton diffusion and optical interference in organic donor–acceptor photovoltaic cells," *J. Appl. Phys.* **90**, 3632 (2001).

[92] J. Gao, J. B. Xu, M. Zhu, N. Ke, and D. Ma, "Thickness dependence of mobility in CuPc thin film on amorphous SiO2 substrate," *J. Phys. D: Appl. Phys.* **40**, 5666–5669 (2007).

[93] J. Zhang, J. Wang, H. Wang, and D. Yan, "Organic thin-film transistors in sandwich configuration," *Appl. Phys. Lett.* **84**, 142 (2004).

[94] M. Ofuji, K. Ishikawa, H. Takezoe, K. Inaba, and K. Omote, "Crystallite size effect on the hole mobility of uniaxially aligned copper phthalocyanine thin-film field-effect transistors," *Appl. Phys. Lett.* **86**, 062114 (2005).

[95] J. Yuan, J. Zhang, J. Wang, X. Yan, D. Yan, and W. Xu, "Bottom-contact organic field-effect transistors having low-dielectric layer under source and drain electrodes," *Appl. Phys. Lett.* **82**, 3967 (2003).

[96] I. Bruder, J. Schöneboom, R. Dinnebier, A. Ojala, S. Schäfer, R. Sens, P. Erk, and J. Weis, "What determines the performance of metal phthalocyanines (MPc, M=Zn, Cu, Ni, Fe) in organic heterojunction solar cells? A combined experimental and theoretical investigation," *Org. Electron.* **11**, 377–387 (2010).

[97] S. Pfuetzner, C. Mickel, J. Jankowski, M. Hein, J. Meiss, C. Schuenemann, C. Elschner, A. A. Levin, B. Rellinghaus, et al., "The influence of substrate heating on morphology and layer growth in C60:ZnPc bulk heterojunction solar cells," *Org. Electron.* **12**, 435–441 (2011).

[98] W. Zeng, K. S. Yong, Z. M. Kam, F. Zhu, and Y. Li, "Effect of blend layer morphology on performance of ZnPc:C60-based photovoltaic cells," *Appl. Phys. Lett.* **97**, 133304 (2010).

[99] H. H. P. Gommans, D. Cheyns, T. Aernouts, C. Girotto, J. Poortmans, and P. Heremans, "Electro-Optical Study of Subphthalocyanine in a Bilayer Organic Solar Cell," *Adv. Funct. Mater.* **17**, 2653–2658 (2007).

[100] R. Pandey, A. A. Gunawan, K. A. Mkhoyan, and R. J. Holmes, "Efficient Organic Photovoltaic Cells Based on Nanocrystalline Mixtures of Boron Subphthalocyanine Chloride and C60," *Adv. Funct. Mater.* **22**, 617–624 (2012).

[101] R. Pandey and R. J. Holmes, "Graded donor-acceptor heterojunctions for efficient organic photovoltaic cells," *Adv. Mater.* **22**, 5301–5305 (2010).

[102] K. V. Chauhan, P. Sullivan, J. L. Yang, and T. S. Jones, "Efficient Organic Photovoltaic Cells through Structural Modification of Chloroaluminum Phthalocyanine/Fullerene Heterojunctions," *J. Phys. Chem. C* **114**, 3304–3308 (2010).

[103] W. Wang, D. Placencia, and N. R. Armstrong, "Planar and textured heterojunction organic photovoltaics based on chloroindium phthalocyanine (ClInPc) versus titanyl phthalocyanine (TiOPc) donor layers," *Org. Electron.* **12**, 383–393 (2011).

[104] R. R. Lunt, T. P. Osedach, P. R. Brown, J. A. Rowehl, and V. Bulović, "Practical roadmap and limits to nanostructured photovoltaics," *Adv. Mater.* **23**, 5712–5727 (2011).

[105] R. A. J. Janssen, J. C. Hummelen, and N. S. Sariciftci, "Polymer-Fullerene Bulk Heterojunction Solar Cells," *MRS Bulletin* **30**, 33–36 (2005).

[106] X. Xi, W. Li, J. Wu, J. Ji, Z. Shi, and G. Li, "A comparative study on the performances of small molecule organic solar cells based on CuPc/C60 and CuPc/C70," *Sol. Energy Mater. Sol. Cells* **94**, 2435–2441 (2010).

[107] J. Sakai, T. Taima, T. Yamanari, and K. Saito, "Annealing effect in the sexithiophene:C70 small molecule bulk heterojunction organic photovoltaic cells," *Sol. Energy Mater. Sol. Cells* **93**, 1149–1153 (2009).

[108] H. X. Wei, J. Li, Y. Cai, Z. Q. Xu, S. T. Lee, Y. Q. Li, and J. X. Tang, "Electronic structures of planar and mixed C70/CuPc heterojunctions in organic photovoltaic devices," *Org. Electron.* **12**, 1422–1428 (2011).

[109] P. Peumans, S. Uchida, and S. R. Forrest, "Efficient bulk heterojunction photovoltaic cells using small-molecular-weight organic thin films," *Nature* **425**, 158–162 (2003).

[110] S. R. Forrest, L. Y. Leu, F. F. So, and W. Y. Yoon, "Optical and electrical properties of isotype crystalline molecular organic heterojunctions," *J. Appl. Phys.* **66**, 5908–5914 (1989).

[111] M. T. Lloyd, J. E. Anthony, and G. G. Malliaras, "Photovoltaics from soluble small molecules," *Materials Today* **10**, 34–41 (2007).

[112] B. Walker, C. Kim, and T.-Q. Nguyen, "Small Molecule Solution-Processed Bulk Heterojunction Solar Cells," *Chem. Mater.* **23**, 470–482 (2011).

[113] G. Wei, S. Wang, K. Renshaw, M. E. Thompson, and S. R. Forrest, "Solution-processed squaraine bulk heterojunction photovoltaic cells," *ACS Nano* **4**, 1927–1934 (2010).

[114] S. Braun, W. R. Salaneck, and M. Fahlman, "Energy-Level Alignment at Organic/Metal and Organic/Organic Interfaces," *Adv. Mater.* **21**, 1450–1472 (2009).

[115] R. Steim, F. R. Kogler, and C. J. Brabec, "Interface materials for organic solar cells," *J. Mater. Chem.* **20**, 2499–2512 (2010).

[116] H. Ma, H.-L. Yip, F. Huang, and A. K. Y. Jen, "Interface Engineering for Organic Electronics," *Adv. Funct. Mater.* **20**, 1371–1388 (2010).

[117] F. J. Zhang, A. Vollmer, J. Zhang, Z. Xu, J. P. Rabe, and N. Koch, "Energy level alignment and morphology of interfaces between molecular and polymeric organic semiconductors," *Org. Electron.* **8**, 606–614 (2007).

[118] S. W. Cho, L. F. J. Piper, A. Demasi, A. R. H. Preston, K. E. Smith, K. V. Chauhan, P. Sullivan, R. A. Hatton, and T. S. Jones, "Electronic Structure of C60/Phthalocyanine/ITO Interfaces Studied using Soft X-ray Spectroscopies," *J. Phys. Chem. C* **114**, 1928–1933 (2010).

[119] P. Peumans and S. R. Forrest, "Very-high-efficiency double-heterostructure copper phthalocyanine/C60 photovoltaic cells," *Appl. Phys. Lett.* **79**, 126 (2001).

[120] A. Kumar, S. Sista, and Y. Yang, "Dipole induced anomalous S-shape I-V curves in polymer solar cells," *J. Appl. Phys.* **105**, 094512 (2009).

[121] D. Gupta, S. Mukhopadhyay, and K. S. Narayan, "Fill factor in organic solar cells," *Sol. Energy Mater. Sol. Cells* **94**, 1309–1313 (2010).

[122] W. Tress, K. Leo, and M. Riede, "Influence of Hole-Transport Layers and Donor Materials on Open-Circuit Voltage and Shape of I-V Curves of Organic Solar Cells," *Adv. Funct. Mater.* **21**, 2140–2149 (2011).

[123] N. R. Armstrong, C. Carter, C. Donley, A. Simmonds, P. Lee, M. Brumbach, B. Kippelen, B. Domercq, and S. Yoo, "Interface modification of ITO thin films: organic photovoltaic cells," *Thin Solid Films* **445**, 342–352 (2003).

[124] M. Andreasson, M. Tengelin-Nilsson, T. G. Andersson, L. Ilver, and J. Kanski, "Importance of ITO surface conditions for the interaction with thin CuPc layers," *Org. Electron.* **6**, 175–181 (2005).

[125] N. R. Armstrong, P. A. Veneman, E. Ratcliff, D. Placencia, and M. Brumbach, "Oxide contacts in organic photovoltaics: characterization and control of near-

surface composition in indium-tin oxide (ITO) electrodes," *Acc. Chem. Res.* **42**, 1748–1757 (2009).

[126] M. G. Mason, L. S. Hung, C. W. Tang, S. T. Lee, K. W. Wong, and M. Wang, "Characterization of treated indium–tin–oxide surfaces used in electroluminescent devices," *J. Appl. Phys.* **86**, 1688 (1999).

[127] J. S. Kim, M. Granstrom, R. H. Friend, N. Johansson, W. R. Salaneck, R. Daik, W. J. Feast, and F. Cacialli, "Indium–tin oxide treatments for single- and double-layer polymeric light-emitting diodes: The relation between the anode physical, chemical, and morphological properties and the device performance," *J. Appl. Phys.* **84**, 6859 (1998).

[128] C. C. Wu, C. I. Wu, J. C. Sturm, and A. Kahn, "Surface modification of indium tin oxide by plasma treatment: An effective method to improve the efficiency, brightness, and reliability of organic light emitting devices," *Appl. Phys. Lett.* **70**, 1348–1350 (1997).

[129] A. Sharma, G. Andersson, and D. A. Lewis, "Role of humidity on indium and tin migration in organic photovoltaic devices.," *Phys. Chem. Chem. Phys.* **13**, 4381–4387 (2011).

[130] A. Sharma, S. E. Watkins, D. A. Lewis, and G. Andersson, "Effect of indium and tin contamination on the efficiency and electronic properties of organic bulk hetero-junction solar cells," *Sol. Energy Mater. Sol. Cells* **95**, 3251–3255 (2011).

[131] M. Y. Chan, C. S. Lee, S. L. Lai, M. K. Fung, F. L. Wong, H. Y. Sun, K. M. Lau, and S. T. Lee, "Efficient organic photovoltaic devices using a combination of exciton blocking layer and anodic buffer layer," *J. Appl. Phys.* **100**, 094506 (2006).

[132] N. Li, B. E. Lassiter, R. R. Lunt, G. Wei, and S. R. Forrest, "Open circuit voltage enhancement due to reduced dark current in small molecule photovoltaic cells," *Appl. Phys. Lett.* **94**, 023307 (2009).

[133] J. Meyer, R. Khalandovsky, P. Görrn, and A. Kahn, "MoO3 films spin-coated from a nanoparticle suspension for efficient hole-injection in organic electronics," *Adv. Mater.* **23**, 70–73 (2011).

[134] K. X. Steirer, P. F. Ndione, N. E. Widjonarko, M. T. Lloyd, J. Meyer, E. L. Ratcliff, A. Kahn, N. R. Armstrong, C. J. Curtis, et al., "Enhanced Efficiency

in Plastic Solar Cells via Energy Matched Solution Processed NiOx Interlayers," *Adv. Energy Mater.* **1**, 813–820 (2011).

[135] S. Khodabakhsh, D. Poplavskyy, S. Heutz, J. Nelson, D. D. C. Bradley, H. Murata, and T. S. Jones, "Using Self-Assembling Dipole Molecules to Improve Hole Injection in Conjugated Polymers," *Adv. Funct. Mater.* **14**, 1205–1210 (2004).

[136] S. Khodabakhsh, B. M. Sanderson, J. Nelson, and T. S. Jones, "Using Self-Assembling Dipole Molecules to Improve Charge Collection in Molecular Solar Cells," *Adv. Funct. Mater.* **16**, 95–100 (2006).

[137] H. Gommans, B. Verreet, B. P. Rand, R. Muller, J. Poortmans, P. Heremans, and J. Genoe, "On the Role of Bathocuproine in Organic Photovoltaic Cells," *Adv. Funct. Mater.* **18**, 3686–3691 (2008).

[138] S. Heutz, P. Sullivan, B. . Sanderson, S. . Schultes, and T. . Jones, "Influence of molecular architecture and intermixing on the photovoltaic, morphological and spectroscopic properties of CuPc–C60 heterojunctions," *Sol. Energy Mater. Sol. Cells* **83**, 229–245 (2004).

[139] M. Y. Chan, S. L. Lai, M. K. Fung, C. S. Lee, and S. T. Lee, "Doping-induced efficiency enhancement in organic photovoltaic devices," *Appl. Phys. Lett.* **90**, 023504 (2007).

[140] N. Wang, J. Yu, Y. Zang, J. Huang, and Y. Jiang, "Effect of buffer layers on the performance of organic photovoltaic cells based on copper phthalocyanine and C60," *Sol. Energy Mater. Sol. Cells* **94**, 263–266 (2010).

[141] N. N. Wang, J. S. Yu, H. Lin, and Y. D. Jiang, "Organic Photovoltaic Cells with Improved Performance Using Bathophenanthroline as a Buffer Layer," *Chin. J. Chem. Phys.* **23**, 84–88 (2010).

[142] B. P. Rand, J. Li, J. Xue, R. J. Holmes, M. E. Thompson, and S. R. Forrest, "Organic Double-Heterostructure Photovoltaic Cells Employing Thick Tris(acetylacetonato)ruthenium(III) Exciton-Blocking Layers," *Adv. Mater.* **17**, 2714–2718 (2005).

[143] B. E. Lassiter, G. Wei, S. Wang, J. D. Zimmerman, V. V. Diev, M. E. Thompson, and S. R. Forrest, "Organic photovoltaics incorporating electron conducting exciton blocking layers," *Appl. Phys. Lett.* **98**, 243307 (2011).

[144] M. Hirade and C. Adachi, "Small molecular organic photovoltaic cells with exciton blocking layer at anode interface for improved device performance," *Appl. Phys. Lett.* **99**, 153302 (2011).

[145] J. G. Van Dijken, N. L.-Y. Wu, M. D. Fleischauer, J. M. Buriak, and M. J. Brett, "Morphology control and nanoscale patterning of small molecule organic thin films," *Proc. of SPIE* **8435**, 8435R (2012).

[146] D. Fraser and H. Cook, "Highly Conductive, Transparent Films of Sputtered InSnO," *J. Electrochem. Soc.* **119**, 1368–1374 (1972).

[147] A. Kumar and C. Zhou, "The race to replace tin-doped indium oxide: which material will win?," *ACS Nano* **4**, 11–14 (2010).

[148] F. Yang and S. R. Forrest, "Organic Solar Cells Using Transparent SnO2–F Anodes," *Adv. Mater.* **18**, 2018–2022 (2006).

[149] H. Wu, L. Hu, M. W. Rowell, D. Kong, J. J. Cha, J. R. McDonough, J. Zhu, Y. Yang, M. D. McGehee, et al., "Electrospun metal nanofiber webs as high-performance transparent electrode," *Nano Lett.* **10**, 4242–4248 (2010).

[150] J. Meiss, N. Allinger, M. K. Riede, and K. Leo, "Improved light harvesting in tin-doped indum oxide (ITO)-free inverted bulk-heterojunction organic solar cells using capping layers," *Appl. Phys. Lett.* **93**, 103311 (2008).

[151] S. Choi, W. J. Potscavage, and B. Kippelen, "ITO-free large-area organic solar cells," *Opt. Express* **18**, A458–A466 (2010).

[152] Y. Galagan, J.-E. J.M. Rubingh, R. Andriessen, C.-C. Fan, P. W.M. Blom, S. C. Veenstra, and J. M. Kroon, "ITO-free flexible organic solar cells with printed current collecting grids," *Sol. Energy Mater. Sol. Cells* **95**, 1339–1343 (2011).

[153] J. van de Lagemaat, T. M. Barnes, G. Rumbles, S. E. Shaheen, T. J. Coutts, C. Weeks, I. Levitsky, J. Peltola, and P. Glatkowski, "Organic solar cells with carbon nanotubes replacing In2O3:Sn as the transparent electrode," *Appl. Phys. Lett.* **88**, 233503 (2006).

[154] Y. H. Kim, C. Sachse, M. L. Machala, C. May, L. Müller-Meskamp, and K. Leo, "Highly Conductive PEDOT:PSS Electrode with Optimized Solvent and Thermal Post-Treatment for ITO-Free Organic Solar Cells," *Adv. Funct. Mater.* **21**, 1076–1081 (2011).

[155] T. Aernouts, P. Vanlaeke, W. Geens, J. Poortmans, P. Heremans, S. Borghs, R. Mertens, R. Andriessen, and L. Leenders, "Printable anodes for flexible organic solar cell modules," *Thin Solid Films* **451-452**, 22–25 (2004).

[156] F. C. Krebs, M. Jørgensen, K. Norrman, O. Hagemann, J. Alstrup, T. D. Nielsen, J. Fyenbo, K. Larsen, and J. Kristensen, "A complete process for production of flexible large area polymer solar cells entirely using screen printing—First public demonstration," *Sol. Energy Mater. Sol. Cells* **93**, 422–441 (2009).

[157] F. C. Krebs, "Roll-to-roll fabrication of monolithic large-area polymer solar cells free from indium-tin-oxide," *Sol. Energy Mater. Sol. Cells* **93**, 1636–1641 (2009).

[158] S. Noh, S. Kim, J. Yang, C. Lee, and J.-Y. Kim, "Investigation into the Thermal Annealing Effect on the Photovoltaic Properties of Organic Solar Cells based on CuPc/C60 Heterojunctions," *J. Korean Phys. Soc.* **53**, 1551–1555 (2008).

[159] J. G. Van Dijken, M. D. Fleischauer, and M. J. Brett, "Controlled nanostructuring of CuPc thin films via glancing angle deposition for idealized organic photovoltaic architectures," *J. Mater. Chem.* **21**, 1013–1019 (2011).

[160] J. Xue, B. P. Rand, S. Uchida, and S. R. Forrest, "Mixed donor-acceptor molecular heterojunctions for photovoltaic applications. II. Device performance," *J. Appl. Phys.* **98**, 124903 (2005).

[161] S. Uchida, J. Xue, B. P. Rand, and S. R. Forrest, "Organic small molecule solar cells with a homogeneously mixed copper phthalocyanine: C60 active layer," *Appl. Phys. Lett.* **84**, 4218 (2004).

[162] S.-W. Chiu, L.-Y. Lin, H.-W. Lin, Y.-H. Chen, Z.-Y. Huang, Y.-T. Lin, F. Lin, Y.-H. Liu, and K.-T. Wong, "A donor-acceptor-acceptor molecule for vacuum-processed organic solar cells with a power conversion efficiency of 6.4%," *Chem. Commun.* **48**, 1857–1859 (2012).

[163] W. Tress, K. Leo, and M. Riede, "Effect of concentration gradients in ZnPc:C60 bulk heterojunction organic solar cells," *Sol. Energy Mater. Sol. Cells* **95**, 2981–2986 (2011).

[164] Z. Li, G. He, X. Wan, Y. Liu, J. Zhou, G. Long, Y. Zuo, M. Zhang, and Y. Chen, "Solution Processable Rhodanine-Based Small Molecule Organic

Photovoltaic Cells with a Power Conversion Efficiency of 6.1%," *Adv. Energy Mater.* **2**, 74–77 (2012).

[165] A. Sánchez-Díaz, R. Pacios, U. Muñecas, T. Torres, and E. Palomares, "Charge transfer reactions in near IR absorbing small molecule solution processed organic bulk-heterojunction solar," *Org. Electron.* **12**, 329–335 (2011).

[166] F. Liang, F. Shi, Y. Fu, L. Wang, X. Zhang, Z. Xie, and Z. Su, "Donor–acceptor conjugates-functionalized zinc phthalocyanine: Towards broad absorption and application in organic solar cells," *Sol. Energy Mater. Sol. Cells* **94**, 1803–1808 (2010).

[167] M. Baldo, M. Deutsch, P. Burrows, H. Gossenberger, M. Gerstenberg, V. Ban, and S. Forrest, "Organic Vapor Phase Deposition," *Adv. Mater.* **10**, 1505–1514 (1998).

[168] M. Hirade, H. Nakanotani, M. Yahiro, and C. Adachi, "Formation of organic crystalline nanopillar arrays and their application to organic photovoltaic cells," *ACS Appl. Mater. Interfaces* **3**, 80–83 (2011).

[169] Y.-S. Hsiao, W.-T. Whang, S.-C. Suen, J.-Y. Shiu, and C.-P. Chen, "Morphological control of CuPc and its application in organic solar cells," *Nanotechnology* **19**, 415603 (2008).

[170] C. Schünemann, C. Elschner, A. A. Levin, M. Levichkova, K. Leo, and M. Riede, "Zinc phthalocyanine — Influence of substrate temperature, film thickness, and kind of substrate on the morphology," *Thin Solid Films* **519**, 3939–3945 (2011).

[171] D. Placencia, W. Wang, R. C. Shallcross, K. W. Nebesny, M. Brumbach, and N. R. Armstrong, "Organic Photovoltaic Cells Based On Solvent-Annealed, Textured Titanyl Phthalocyanine/C60 Heterojunctions," *Adv. Funct. Mater.* **19**, 1913–1921 (2009).

[172] S. Karak, S. K. Ray, and A. Dhar, "Improvement of efficiency in solar cells based on vertically grown copper phthalocyanine nanorods," *J. Phys. D: Appl. Phys.* **43**, 245101 (2010).

[173] H. Xi, Z. Wei, Z. Duan, W. Xu, and D. Zhu, "Facile Method for Fabrication of Nanostructured CuPc Thin Films To Enhance Photocurrent Generation," *J. Phys. Chem. C* **112**, 19934–19938 (2008).

[174] N. Obata, Y. Sato, E. Nakamura, and Y. Matsuo, "Small-Molecule-Based Organic Photovoltaic Devices Covering Visible and Near-Infrared Absorption through Phase Transition of Titanylphthalocyanine Induced by Solvent Exposure," *Jpn. J. Appl. Phys.* **50**, 121603 (2011).

[175] Y. Matsuo, Y. Sato, T. Niinomi, I. Soga, H. Tanaka, and E. Nakamura, "Columnar structure in bulk heterojunction in solution-processable three-layered p-i-n organic photovoltaic devices using tetrabenzoporphyrin precursor and silylmethyl[60]fullerene," *J. Am. Chem. Soc.* **131**, 16048–16050 (2009).

[176] J. G. Van Dijken, M. D. Fleischauer, and M. J. Brett, "Advanced Nanostructuring of Metal Phthalocyanines for Organic Photovoltaic Devices," in *Proc. 37th IEEE Photov. Spec. Conf.*, pp. 3469–3471 (2011).

[177] J. G. Van Dijken, M. D. Fleischauer, and M. J. Brett, "Solvent effects on ZnPc thin films and their role in fabrication of nanostructured organic solar cells," *Org. Electron.* **12**, 2111–2119 (2011).

[178] J. G. Van Dijken and M. J. Brett, "Dry etching of metal phthalocyanine films: effects on morphology and surface stoichiometry," *Molecules* **17**, 10119–10130 (2012).

[179] J. G. Van Dijken and M. J. Brett, "Nanopillar ITO electrodes via argon plasma etching," *J. Vac. Sci. Technol. A* **30**, 040606 (2012).

[180] K. Robbie, M. J. Brett, and A. Lakhtakia, "Chiral sculptured thin films," *Nature* **384**, 616 (1996).

[181] K. Robbie and M. J. Brett, "Sculptured thin films and glancing angle deposition: Growth mechanics and applications," *J. Vac. Sci. Technol. A* **15**, 1460–1465 (1997).

[182] J. J. Steele and M. J. Brett, "Nanostructure engineering in porous columnar thin films: recent advances," *J. Mater. Sci.-Mater. Electron.* **18**, 367–379 (2007).

[183] M. M. Hawkeye and M. J. Brett, "Glancing angle deposition: Fabrication, properties, and applications of micro- and nanostructured thin films," *J. Vac. Sci. Technol. A* **25**, 1317–1335 (2007).

[184] S. Kennedy, "Photonics Applications of Nanostructured Thin Films," PhD Thesis, Electrical and Computer Engineering, University of Alberta (2004).

[185] D. Gish, M. Summers, and M. Brett, "Morphology of periodic nanostructures for photonic crystals grown by glancing angle deposition," *Photonics Nanostruct.* **4**, 23–29 (2006).

[186] M. T. Taschuk, K. M. Krause, J. J. Steele, M. A. Summers, and M. J. Brett, "Growth scaling of metal oxide columnar thin films deposited by glancing angle depositions," *J. Vac. Sci. Technol. B* **27**, 2106–2111 (2009).

[187] M. Summers, B. Djurfors, and M. Brett, "Fabrication of silicon submicrometer ribbons by glancing angle deposition," *J. Microlith., Microfab., Microsyst.* **4**, 033012 (2005).

[188] M. O. Jensen and M. J. Brett, "Periodically structured glancing angle deposition thin films," *IEEE Trans. Nanotechnol.* **4**, 269–277 (2005).

[189] M. A. Summers and M. J. Brett, "Optimization of periodic column growth in glancing angle deposition for photonic crystal fabrication," *Nanotechnology* **19**, 415203 (2008).

[190] N. Li and S. R. Forrest, "Tilted bulk heterojunction organic photovoltaic cells grown by oblique angle deposition," *Appl. Phys. Lett.* **95**, 123309 (2009).

[191] Y. Zheng, R. Bekele, J. Ouyang, and J. Xue, "Organic photovoltaic cells with vertically aligned crystalline molecular nanorods," *Org. Electron.* **10**, 1621–1625 (2009).

[192] M. Thomas, B. J. Worfolk, D. A. Rider, M. T. Taschuk, J. M. Buriak, and M. J. Brett, "C60 fullerene nanocolumns-polythiophene heterojunctions for inverted organic photovoltaic cells," *ACS Appl. Mater. Interfaces* **3**, 1887–1894 (2011).

[193] D. A. Rider, R. T. Tucker, B. J. Worfolk, K. M. Krause, A. Lalany, M. J. Brett, J. M. Buriak, and K. D. Harris, "Indium tin oxide nanopillar electrodes in polymer/fullerene solar cells," *Nanotechnology* **22**, 085706 (2011).

[194] S. Yu, C. Klimm, P. Schäfer, J. P. Rabe, B. Rech, and N. Koch, "Organic photovoltaic cells with interdigitated structures based on pentacene nanocolumn arrays," *Org. Electron.* **12**, 2180–2184 (2011).

[195] Y. Zhou, T. Taima, T. Miyadera, T. Yamanari, M. Kitamura, K. Nakatsu, and Y. Yoshida, "Glancing Angle Deposition of Copper Iodide Nanocrystals for Efficient Organic Photovoltaics.," *Nano Lett.*, ASAP (2012).

[196] G. K. Kiema, M. J. Colgan, and M. J. Brett, "Dye sensitized solar cells incorporating obliquely deposited titanium oxide layers," *Sol. Energy Mater. Sol. Cells* **85**, 321–331 (2005).

[197] H.-Y. Yang, M.-F. Lee, C.-H. Huang, Y.-S. Lo, Y.-J. Chen, and M.-S. Wong, "Glancing angle deposited titania films for dye-sensitized solar cells," *Thin Solid Films* **518**, 1590–1594 (2009).

[198] Z. Xie, B. M. Henry, K. R. Kirov, H. E. Smith, A. Barkhouse, and C. R. M. Grovenor, "Study of the effect of changing the microstructure of titania layers on composite solar cell performance," *Thin Solid Films* **511-512**, 523–528 (2006).

[199] N. J. Gerein, M. D. Fleischauer, and M. J. Brett, "Effect of TiO2 film porosity and thermal processing on TiO2–P3HT hybrid materials and photovoltaic device performance," *Sol. Energy Mater. Sol. Cells* **94**, 2343–2350 (2010).

[200] P. C. P. Hrudey, K. L. Westra, and M. J. Brett, "Highly Ordered Organic Alq3 Chiral Luminescent Thin Films Fabricated by Glancing-Angle Deposition," *Adv. Mater.* **18**, 224–228 (2006).

[201] J. Zhang, I. Salzmann, S. Rogaschewski, J. P. Rabe, N. Koch, F. Zhang, and Z. Xu, "Arrays of crystalline C60 and pentacene nanocolumns," *Appl. Phys. Lett.* **90**, 193117 (2007).

[202] J. Zhang, I. Salzmann, P. Schäfer, M. Oehzelt, S. Duhm, J. P. Rabe, and N. Koch, "The morphology of organic nanocolumn arrays: Amorphous versus crystalline solids," *J. Mater. Res.* **24**, 1492–1497 (2009).

[203] I. Hodgkinson and Q. H. Wu, "Inorganic Chiral Optical Materials," *Adv. Mater.* **13**, 889–897 (2001).

[204] A. C. van Popta, J. C. Sit, and M. J. Brett, "Optical properties of porous helical thin films," *Appl. Optics* **43**, 3632–3639 (2004).

[205] J. B. Sorge, A. C. van Popta, J. C. Sit, and M. J. Brett, "Circular birefringence dependence on chiral film porosity," *Opt. Express* **14**, 10550–10557 (2006).

[206] K. M. Krause and M. J. Brett, "Spatially Graded Nanostructured Chiral Films as Tunable Circular Polarizers," *Adv. Funct. Mater.* **18**, 3111–3118 (2008).

[207] R. Tait, T. Smy, and M. Brett, "Modelling and characterization of columnar growth in evaporated films," *Thin Solid Films* **226**, 196–201 (1993).

[208] M. Robinson and G. Klein, "Unit Cell Constants of α-Copper Phthalocyanine," *J. Am. Chem. Soc.* **74**, 6294–6295 (1952).

[209] R. Prabakaran, R. Kesavamoorthy, G. L. N. Reddy, and F. P. Xavier, "Structural Investigation of Copper Phthalocyanine Thin Films Using X-Ray Diffraction, Raman Scattering and Optical Absorption Measurements," *Phys. Status Solidi B* **229**, 1175–1186 (2002).

[210] M. T. Taschuk, J. Chai, J. M. Buriak, and M. J. Brett, "Optical characterization of pseudo-ordered nanostructured thin films," *Phys. Status Solidi C* **6**, S127–S130 (2009).

[211] J. Chai, M. T. Taschuk, M. J. Brett, and J. M. Buriak, "Large area assembled periodic nanoarrays by block copolymer templating and glancing angle deposition," *Proceedings of SPIE* **7041**, 704111 (2008).

[212] M. Aizawa and J. M. Buriak, "Block copolymer-templated chemistry on Si, Ge, InP, and GaAs surfaces," *J. Am. Chem. Soc.* **127**, 8932–8933 (2005).

[213] M. Aizawa and J. M. Buriak, "Nanoscale patterning of two metals on silicon surfaces using an ABC triblock copolymer template," *J. Am. Chem. Soc.* **128**, 5877–5886 (2006).

[214] M. Aizawa and J. M. Buriak, "Block copolymer templated chemistry for the formation of metallic nanoparticle arrays on semiconductor surfaces," *Chem. Mater.* **19**, 5090–5101 (2007).

[215] J. Chai, D. Wang, X. Fan, and J. M. Buriak, "Assembly of aligned linear metallic patterns on silicon," *Nat. Nanotechnol.* **2**, 500–506 (2007).

[216] J. Chai and J. M. Buriak, "Using Cylindrical Domains of Block Copolymers To Self-Assemble and Align Metallic Nanowires," *ACS Nano* **2**, 489–501 (2008).

[217] X. Zhang, K. Harris, N. Wu, J. Murphy, and J. M. Buriak, "Fast Assembly of Ordered Block Copolymer Nanostructures through Microwave Annealing," *ACS Nano* **4**, 7021–7029 (2010).

[218] X. Zhang, J. N. Murphy, N. L. Y. Wu, K. D. Harris, and J. M. Buriak, "Rapid Assembly of Nanolines with Precisely Controlled Spacing from Binary Blends of Block Copolymers," *Macromolecules* **44**, 9752–9757 (2011).

[219] N. L. Y. Wu, X. Zhang, J. N. Murphy, J. Chai, K. D. Harris, and J. M. Buriak, "Density doubling of block copolymer templated features," *Nano Lett.* **12**, 264–268 (2012).

[220] J. Liu, Y. Shi, and Y. Yang, "Solvation-Induced Morphology Effects on the Performance of Polymer-Based Photovoltaic Devices," *Adv. Funct. Mater.* **11**, 420–424 (2001).

[221] H. Hoppe, M. Niggemann, C. Winder, J. Kraut, R. Hiesgen, A. Hinsch, D. Meissner, and N. S. Sariciftci, "Nanoscale morphology of conjugated polymer/fullerene-based bulk-heterojunction solar cells," *Adv. Funct. Mater.* **14**, 1005–1011 (2004).

[222] Y. Liang and L. Yu, "A new class of semiconducting polymers for bulk heterojunction solar cells with exceptionally high performance," *Acc. Chem. Res.* **43**, 1227–1236 (2010).

[223] S. M. T. Nunes, F. S. Sguilla, and A. C. Tedesco, "Photophysical studies of zinc phthalocyanine and chloroaluminum phthalocyanine incorporated into liposomes in the presence of additives," *Braz. J. Med. Biol. Res.* **37**, 273–284 (2004).

[224] Z. Guo, B. Chen, M. Zhang, J. Mu, C. Shao, and Y. Liu, "Zinc phthalocyanine hierarchical nanostructure with hollow interior space: solvent-thermal synthesis and high visible photocatalytic property," *J. Colloid Interface Sci.* **348**, 37–42 (2010).

[225] S. Schumann, R. A. Hatton, and T. S. Jones, "Organic photovoltaic devices based on water-soluble copper phthalocyanine," *J. Phys. Chem. C* **115**, 4916–4921 (2011).

[226] A. Slodek, D. Wöhrle, J. J. Doyle, and W. Blau, "Metal Complexes of Phthalocyanines in Polymers as Suitable Materials for Optical Limiting," *Macromol. Symp.* **235**, 9–18 (2006).

[227] S. M. Schultes, P. Sullivan, S. Heutz, B. M. Sanderson, and T. S. Jones, "The role of molecular architecture and layer composition on the properties and performance of CuPc-C60 photovoltaic devices," *Mat. Sci. Eng. C* **25**, 858–865 (2005).

[228] C. C. Leznoff and A. B. P. Lever, Eds., *Phthalocyanines: Properties and Applications*, in *Phthalocyanines Properties and Applications*, VCH Publishers, New York (1989).

[229] M. Whalley, "Conjugated Macrocycles. Part XXXII. Absorption Spectra of Tetrazaporphins and Phthalocyanines. Formation of Pyridine Salts.," *J. Chem. Soc.*, 866–869 (1961).

[230] M. P. de Jong, L. J. van IJzendoorn, and M. J. A. de Voigt, "Stability of the interface between indium-tin-oxide and poly(3,4-ethylenedioxythiophene)/poly(styrenesulfonate) in polymer light-emitting diodes," *Appl. Phys. Lett.* **77**, 2255–2257 (2000).

[231] Y. Kim, S. Lee, J. Noh, and S. Han, "Performance and stability of electroluminescent device with self-assembled layers of poly(3,4-ethylenedioxythiophene)–poly(styrenesulfonate) and polyelectrolytes," *Thin Solid Films* **510**, 305–310 (2006).

[232] J. Peet, M. L. Senatore, A. J. Heeger, and G. C. Bazan, "The Role of Processing in the Fabrication and Optimization of Plastic Solar Cells," *Adv. Mater.* **21**, 1521–1527 (2009).

[233] K. R. Graham, J. Mei, R. Stalder, J. W. Shim, H. Cheun, F. Steffy, F. So, B. Kippelen, and J. R. Reynolds, "Polydimethylsiloxane as a macromolecular additive for enhanced performance of molecular bulk heterojunction organic solar cells.," *ACS Appl. Mater. Interfaces* **3**, 1210–1215 (2011).

[234] V. Shrotriya, G. Li, Y. Yao, T. Moriarty, K. Emery, and Y. Yang, "Accurate Measurement and Characterization of Organic Solar Cells," *Adv. Funct. Mater.* **16**, 2016–2023 (2006).

[235] T. Taima, S. Toyoshima, K. Hara, K. Saito, and K. Yase, "Control of Measurement Environments for High-Efficiency Organic Photovoltaic Cells," *Jpn. J. Appl. Phys.* **45**, L217–L219 (2006).

[236] K. Kudo, T. Sumimoto, K. Hiraga, S. Kuniyoshi, and K. Tanaka, "Evaluation of electrical properties of evaporated thin films of metal-free, copper and lead phthalocyanines by in-situ field effect measurements," *Jpn. J. Appl. Phys.* **36**, 6994–6998 (1997).

[237] K. O. Sylvester-Hvid, "Two-dimensional simulations of CuPc-PCTDA solar cells: the importance of mobility and molecular pi stacking," *J. Phys. Chem. B* **110**, 2618–2627 (2006).

[238] L. Grządziel, M. Krzywiecki, H. Peisert, T. Chassé, and J. Szuber, "Influence of ambient air exposure on surface chemistry and electronic properties of thin

copper phthalocyanine sensing layers," *Thin Solid Films* **519**, 2187–2192 (2011).

[239] S. J. Duclos, R. C. Haddon, S. H. Glarum, A. F. Hebard, and K. B. Lyons, "The Influence of Oxygen on the Raman Spectrum of C60 Films," *Solid State Commun.* **80**, 481–484 (1991).

[240] A. Tapponnier, I. Biaggio, and P. Günter, "Ultrapure C60 field-effect transistors and the effects of oxygen exposure," *Appl. Phys. Lett.* **86**, 112114 (2005).

[241] I. Kim and G. E. Jabbour, "Effect of annealing on bulk heterojunction organic solar cells based on copper phthalocyanine and perylene derivative," *Synthetic Met.* **162**, 102–106 (2012).

[242] H. X. Wei, J. Li, Z. Q. Xu, Y. Cai, J. X. Tang, and Y. Q. Li, "Thermal annealing-induced vertical phase separation of copper phthalocyanine: Fullerene bulk heterojunction in organic photovoltaic cells," *Appl. Phys. Lett.* **97**, 083302 (2010).

[243] C. Hordequin, D. Tromson, A. Brambilla, P. Bergonzo, and F. Foulon, "Strong impact of x-ray radiation associated with electron beam metallization of diamond devices," *J. Appl. Phys.* **90**, 2533 (2001).

[244] B. Yu, L. Huang, H. Wang, and D. Yan, "Efficient organic solar cells using a high-quality crystalline thin film as a donor layer," *Adv. Mater.* **22**, 1017–1020 (2010).

[245] M. J. Nobes, J. S. Colligon, and G. Carter, "The equilibrium topography of sputtered amorphous solids," *J. Mater. Sci.* **4**, 730–733 (1969).

[246] O. Auciello and R. Kelly, Eds., *Ion Bombardment Modification of Surfaces*, Elsevier Publishing Co., Amsterdam (1984).

[247] B. V. King and I. S. T. Tsong, "The depth resolution of sputter profiling," *Ultramicroscopy* **14**, 75–78 (1984).

[248] M. Tanemura and F. Okuyama, "Topographical features of N2+-Sputtered Metal Sandwiches: Their Correlation With Auger Depth Resolution," *Thin Solid Films* **165**, 193–209 (1988).

[249] E.-H. Cirlin, J. J. Vajo, R. E. Doty, and T. C. Hasenberg, "Ion-induced topography, depth resolution, and ion yield during secondary ion mass

spectrometry depth profiling of a GaAs/AlGaAs superlattice: Effects of sample rotation," *J. Vac. Sci. Technol. A* **9**, 1395–1401 (1991).

[250] S. Hofmann, "Approaching the limits of high resolution depth profiling," *Appl. Surf. Sci.* **70-71**, 9–19 (1993).

[251] G. Carter, "The effects of ion bombardment sputtering and atomic transport related roughening and smoothing on depth profiling resolution," *Vacuum* **47**, 409–420 (1996).

[252] G. Carter, "The physics and applications of ion beam erosion," *J. Phys. D: Appl. Phys.* **34**, R1–R22 (2001).

[253] P. Karmakar, S. A. Mollick, D. Ghose, and A. Chakrabarti, "Role of initial surface roughness on ion induced surface morphology," *Appl. Phys. Lett.* **93**, 103102 (2008).

[254] I. Sulania, A. Tripathi, D. Kabiraj, M. Lequeux, and D. Avasthi, "Surface patterning on indium phosphide with low energy Ar atoms bombardment: an evolution from nanodots to nanoripples," *Adv. Mat. Lett.* **1**, 118–122 (2010).

[255] K. Zhang, M. Brötzmann, and H. Hofsäss, "Surfactant-driven self-organized surface patterns by ion beam erosion," *New J. Phys.* **13**, 013033 (2011).

[256] W. Pamler, K. Wangemann, S. Kampermann, and W. Hosler, "Depth Resolution in Auger Depth Profile Analysis of Aluminum Metallization in Microelectronics: The Effect of Crystalline Texture," *Nucl. Instrum. Methods* **51**, 34–40 (1990).

[257] M. Tanemura, S. Fujimoto, and F. Okuyama, "Dependence of Auger Depth Resolution and Surface Texturing on Primary Ion Species," *Surf. Sci.* **230**, 283–289 (1990).

[258] H.-G. Cramer, T. Grehl, F. Kollmer, R. Moellers, E. Niehuis, and D. Rading, "Depth profiling of organic materials using improved ion beam conditions," *Appl. Surf. Sci.* **255**, 966–969 (2008).

[259] S. Ninomiya, K. Ichiki, H. Yamada, Y. Nakata, T. Seki, T. Aoki, and J. Matsuo, "Molecular depth profiling of multilayer structures of organic semiconductor materials by secondary ion mass spectrometry with large argon cluster ion beams," *Rapid Commun. Mass Spectrom.* **23**, 3264–3268 (2009).

[260] D. E. Weibel, N. Lockyer, and J. C. Vickerman, "C60 cluster ion bombardment of organic surfaces," *Appl. Surf. Sci.* **231-232**, 146–152 (2004).

[261] E. A. Jones, J. S. Fletcher, C. E. Thompson, D. A. Jackson, N. P. Lockyer, and J. C. Vickerman, "ToF-SIMS analysis of bio-systems: Are polyatomic primary ions the solution?," *Appl. Surf. Sci.* **252**, 6844–6854 (2006).

[262] N. Winograd, Z. Postawa, J. Cheng, C. Szakal, J. Kozole, and B. J. Garrison, "Improvements in SIMS continue - is the end in sight?," *Appl. Surf. Sci.* **252**, 6836–6843 (2006).

[263] H. K. Shon, T. G. Lee, D. H. Kim, H. J. Kang, B. H. Lee, M. M. Sung, and D. W. Moon, "The effect of C60 cluster ion beam bombardment in sputter depth profiling of organic–inorganic hybrid multiple thin films," *Appl. Surf. Sci.* **255**, 1055–1057 (2008).

[264] T. Miyayama, N. Sanada, S.-I. Iida, J. S. Hammond, and M. Suzuki, "The effect of angle of incidence to low damage sputtering of organic polymers using a C60 ion beam," *Appl. Surf. Sci.* **255**, 951–953 (2008).

[265] J. B. Sorge and M. J. Brett, "Film morphology modification in ion-assisted glancing angle deposition," *Thin Solid Films* **519**, 1356–1360 (2010).

[266] M. T. Taschuk, J. B. Sorge, J. J. Steele, and M. J. Brett, "Ion-Beam Assisted Glancing Angle Deposition for Relative Humidity Sensors," *IEEE Sens. J.* **8**, 1521–1522 (2008).

[267] M. R. Kupsta, M. T. Taschuk, M. J. Brett, and J. C. Sit, "Reactive Ion Etching of Columnar Nanostructured TiO2 Thin Films for Modified Relative Humidity Sensor Response Time," *IEEE Sens. J.* **9**, 1979–1986 (2009).

[268] J. K. Kwan and J. C. Sit, "The use of ion-milling to control clustering of nanostructured, columnar thin films," *Nanotechnology* **21**, 295301 (2010).

[269] S. R. Jim, A. J. Oko, M. T. Taschuk, and M. J. Brett, "Morphological modification of nanostructured ultrathin-layer chromatography stationary phases," *J. Chromatogr. A* **1218**, 7203–7210 (2011).

[270] M. Naddaf, S. Chakane, S. Jain, S. V. Bhoraskar, and A. B. Mandale, "Modification of sensing properties of metallophthalocyanine by an ECR plasma," *Nucl. Instrum. Meth. B* **194**, 54–60 (2002).

[271] G. L. Pakhomov, M. N. Drozdov, and N. V. Vostokov, "Plasma irradiation effects in phthalocyanine films," *Appl. Surf. Sci.* **230**, 241–248 (2004).

[272] M. L. Kaplan, S. R. Forrest, P. H. Schmidt, and T. Venkatesan, "Optical and electrical properties of ion-beam-irradiated films of organic molecular solids and polymers," *J. Appl. Phys.* **55**, 732 (1984).

[273] A. Nath, M. J. Prushan, and J. G. Gilbert, "Can super-excited molecules survive fragmentation?," *J. Radioanal. Nucl. Chem.* **247**, 589–591 (2001).

[274] A. Vomiero, S. Bianchi, E. Comini, G. Faglia, M. Ferroni, and G. Sberveglieri, "Controlled Growth and Sensing Properties of In2O3 Nanowires," *Cryst. Growth Des.* **7**, 2500–2504 (2007).

[275] X. Y. Xue, Y. J. Chen, Y. G. Liu, S. L. Shi, Y. G. Wang, and T. H. Wang, "Synthesis and ethanol sensing properties of indium-doped tin oxide nanowires," *Appl. Phys. Lett.* **88**, 201907 (2006).

[276] V. S. Vaishnav, P. D. Patel, and N. G. Patel, "Indium Tin Oxide thin film gas sensors for detection of ethanol vapours," *Thin Solid Films* **490**, 94–100 (2005).

[277] T. Meziani, P. Colpo, V. Lambertini, G. Ceccone, and F. Rossi, "Dry etching of ITO by magnetic pole enhanced inductively coupled plasma for display and biosensing devices," *Appl. Surf. Sci.* **252**, 3861–3870 (2006).

[278] M. Sawada, M. Higuchi, and S. Kondo, "Characteristics of indium-tin-oxide/silver/indium-tin-oxide sandwich films and their application to simple-matrix liquid-crystal displays," *Jpn. J. Appl. Phys.* **40**, 3332–3336 (2001).

[279] R. G. Gordon, "Criteria for Choosing Transparent Conductors," *MRS Bulletin* **25**, 52–57 (2000).

[280] K. J. Byeon, H. Park, J. Y. Cho, K. Y. Yang, J. H. Baek, G. Y. Jung, and H. Lee, "Fabrication of photonic crystal structure on indium tin oxide electrode of GaN-based light-emitting diodes," *Phys. Status Solidi A* **208**, 480–483 (2011).

[281] Y.-C. Chen, P.-C. Kao, and S.-Y. Chu, "UV-ozone-treated ultra-thin NaF film as anode buffer layer on organic light emitting devices," *Opt. Express* **18**, A167 (2010).

[282] H.-G. Hong, S. S. Kim, D. Y. Kim, T. Lee, K.-K. Kim, J.-O. Song, J. H. Cho, and T.-Y. Seong, "Recovery of dry etch-induced damage of nano-patterned

GaN-based light-emitting diodes by rapid-thermal-annealing," *Phys. Status Solidi A* **204**, 881–886 (2007).

[283] H. Kim, A. Piqué, J. S. Horwitz, H. Mattoussi, H. Murata, Z. H. Kafafi, and D. B. Chrisey, "Indium tin oxide thin films for organic light-emitting devices," *Appl. Phys. Lett.* **74**, 3444–3446 (1999).

[284] E. Joanni, R. Savu, M. de Sousa Góes, P. R. Bueno, J. N. de Freitas, A. F. Nogueira, E. Longo, and J. A. Varela, "Dye-sensitized solar cell architecture based on indium–tin oxide nanowires coated with titanium dioxide," *Scr. Mater.* **57**, 277–280 (2007).

[285] G. Dennler, M. C. Scharber, and C. J. Brabec, "Polymer-Fullerene Bulk-Heterojunction Solar Cells," *Adv. Mater.* **21**, 1323–1338 (2009).

[286] P. Boland, K. Lee, and G. Namkoong, "Device optimization in PCPDTBT:PCBM plastic solar cells," *Sol. Energy Mater. Sol. Cells* **94**, 915–920 (2010).

[287] A. J. Moulé, J. B. Bonekamp, and K. Meerholz, "The effect of active layer thickness and composition on the performance of bulk-heterojunction solar cells," *J. Appl. Phys.* **100**, 094503 (2006).

[288] G. Li, V. Shrotriya, Y. Yao, and Y. Yang, "Investigation of annealing effects and film thickness dependence of polymer solar cells based on poly(3-hexylthiophene)," *J. Appl. Phys.* **98**, 043704 (2005).

[289] T. M. Clarke, D. B. Rodovsky, A. A. Herzing, J. Peet, G. Dennler, D. DeLongchamp, C. Lungenschmied, and A. J. Mozer, "Significantly Reduced Bimolecular Recombination in a Novel Silole-Based Polymer: Fullerene Blend," *Adv. Energy Mater.* **1**, 1062–1067 (2011).

[290] J. Peet, L. Wen, P. Byrne, S. Rodman, K. Forberich, Y. Shao, N. Drolet, R. Gaudiana, G. Dennler, et al., "Bulk heterojunction solar cells with thick active layers and high fill factors enabled by a bithiophene-co-thiazolothiazole push-pull copolymer," *Appl. Phys. Lett.* **98**, 043301 (2011).

[291] C. N. Hoth, P. Schilinsky, S. A. Choulis, and C. J. Brabec, "Printing highly efficient organic solar cells," *Nano Lett.* **8**, 2806–2813 (2008).

[292] H. K. Yu, W. J. Dong, G. H. Jung, and J.-L. Lee, "Three-dimensional nanobranched indium-tin-oxide anode for organic solar cells," *ACS Nano* **5**, 8026–8032 (2011).

[293] J. E. Allen and C. T. Black, "Improved power conversion efficiency in bulk heterojunction organic solar cells with radial electron contacts.," *ACS Nano* **5**, 7986–7991 (2011).

[294] M. K. Fung, Y. C. Sun, A. Ng, A. M. C. Ng, A. B. Djurišić, H. T. Chan, and W. K. Chan, "Indium tin oxide nanorod electrodes for polymer photovoltaics.," *ACS Appl. Mater. Interfaces* **3**, 522–527 (2011).

[295] P. Yu, C.-H. Chang, M.-S. Su, M.-H. Hsu, and K.-H. Wei, "Embedded indium-tin-oxide nanoelectrodes for efficiency and lifetime enhancement of polymer-based solar cells," *Appl. Phys. Lett.* **96**, 153307 (2010).

[296] A. L. Beaudry, R. T. Tucker, J. M. Laforge, M. T. Taschuk, and M. J. Brett, "Indium tin oxide nanowhisker morphology control by vapour-liquid-solid glancing angle deposition," *Nanotechnology* **23**, 105608 (2012).

[297] S. Rajaputra, G. Sagi, and V. P. Singh, "Schottky diode solar cells on electrodeposited copper phthalocyanine films," *Sol. Energy Mater. Sol. Cells* **93**, 60–64 (2009).

[298] G. Chintakula, S. Rajaputra, and V. P. Singh, "Schottky diodes on nanowires of copper phthalocyanine," *Sol. Energy Mater. Sol. Cells* **94**, 34–39 (2010).

[299] H. Benten, N. Kudo, H. Ohkita, and S. Ito, "Layer-by-layer deposition films of copper phthalocyanine derivative; their photoelectrochemical properties and application to solution-processed thin-film organic solar cells," *Thin Solid Films* **517**, 2016–2022 (2009).

[300] J. H. Park, H. K. Park, J. Jeong, W. Kim, B. K. Min, and Y. R. Do, "Wafer-Scale Growth of ITO Nanorods by Radio Frequency Magnetron Sputtering Deposition," *J. Electrochem. Soc.* **158**, K131–K135 (2011).

[301] S. H. Lee and N. Y. Ha, "Nanostructured indium-tin-oxide films fabricated by all-solution processing for functional transparent electrodes," *Opt. Express* **19**, 21803–21808 (2011).

[302] F. M. Toma, A. Sartorel, M. Iurlo, M. Carraro, P. Parisse, C. Maccato, S. Rapino, B. R. Gonzalez, H. Amenitsch, et al., "Efficient water oxidation at carbon nanotube-polyoxometalate electrocatalytic interfaces," *Nat. Chem.* **2**, 826–831 (2010).

[303] A. Purwanto, H. Widiyandari, D. Hidayat, F. Iskandar, and K. Okuyama, "Facile Method for the Fabrication of Vertically Aligned ITO Nanopillars with Excellent Properties," *Chem. Mater.* **21**, 4087–4089 (2009).

[304] S. Kundu and P. Biswas, "Synthesis of nanostructured sol–gel ITO films at different temperatures and study of their absorption and photoluminescence properties," *Opt. Mater.* **31**, 429–433 (2008).

[305] M. Takabatake, Y. Wakui, and N. Konishi, "Indium Tin Oxide Dry Etching Using HBr Gas for Thin Film Transistor Liquid Crystal Displays," *J. Electrochem. Soc.* **142**, 2470–2473 (1995).

[306] J. A. Floro, S. M. Rossnagel, and R. S. Robinson, "Ion-bombardment-induced whisker formation on graphite," *J. Vac. Sci. Technol. A* **1**, 1398–1402 (1983).

[307] H. Kobayashi, T. Ishida, K. Nakamura, Y. Nakato, and H. Tsubomura, "Properties of indium tin oxide films prepared by the electron beam evaporation method in relation to characteristics of indium tin oxide/silicon oxide/silicon junction solar cells," *J. Appl. Phys.* **72**, 5288–5293 (1992).

[308] L.-J. Meng, A. Macarico, and R. Martins, "Study of annealed indium tin oxide films prepared by rf reactive magnetron sputtering," *Vacuum* **46**, 673–680 (1995).

[309] T. Ishida, H. Kobayashi, and Y. Nakato, "Structures and properties of electron-beam-evaporated indium tin oxide films as studied by x-ray photoelectron spectroscopy and work-function measurements," *J. Appl. Phys.* **73**, 4344–4350 (1993).

[310] Y. Park, V. Choong, Y. Gao, B. R. Hsieh, and C. W. Tang, "Work function of indium tin oxide transparent conductor measured by photoelectron spectroscopy," *Appl. Phys. Lett.* **68**, 2699–2701 (1996).

[311] I. D. Parker, "Carrier tunneling and device characteristics in polymer light-emitting diodes," *J. Appl. Phys.* **75**, 1656–1666 (1994).

[312] N. Balasubramanian and A. Subrahmanyam, "Studies on Evaporated Indium Tin Oxide (ITO)/Silicon Junctions and an Estimation of ITO Work Function," *J. Electrochem. Soc.* **138**, 322–324 (1991).

[313] O. Auciello, "Ion interaction with solids: Surface texturing, some bulk effects, and their possible applications," *J. Vac. Sci. Technol.* **19**, 841–867 (1981).

[314] J. J. Cuomo, S. M. Rossnagel, and H. R. Kaufman, Eds., *Handbook of Ion Beam Processing Technology - Principles, Deposition, Film Modification and Synthesis*, Noyes Publications, Park Ridge, New Jersey (1989).

APPENDIX A

Effect of number of substrates present in etch chamber on bias voltage

As noted in Chapter 7, the etch rate and ITO nanopillar morphology appeared to depend somewhat on the amount of substrate area present in the etching chamber. Specifically, the etch rate decreased when etching more samples at once. The RF power of the system used here is defined and maintained according to user input. The voltage used by the system to accomplish this power is therefore dependent on the impedance of the plasma. Changes in the voltage were recorded as additional substrates were introduced in the etch chamber. As shown in Table A.1, the voltage rises in response to the presence of extra substrates. To ensure consistent power, a voltage rise corresponds with a decreased current, which could partly explain the lower etch rates observed when extra substrates were added. Evidently, the total substrate area has a noticeable effect on the impedance of the plasma and thus the etch performance; attention must be paid to this detail for etching at a larger scale.

The Ar flow during all of these measurements was 110 sccm, and the exhaust line valve was not adjusted between any of measurements 1 - 6. For measurements 7 - 13 the exhaust line valve was adjusted slightly each time to ensure a consistent 190 mTorr reading. The chamber was vented between each measurement, including measurements 5 and 6 where it was vented solely to check the consistency between pump-downs, without changing the number of substrates or their orientation.

Table A.1 Pressure, power, and voltage data for the plasma etch reactor with different numbers of samples present.

Measurement	Substrates in etch chamber	Pressure (mTorr)	RF Power (W)	Voltage (V)
1	0	190 ± 2	220 ± 1	35.0 ± 0.5
2	2	187 ± 2	220 ± 1	36.0 ± 0.5
3	4	185 ± 2	220 ± 1	36.0 ± 0.5
4	9	187 ± 2	220 ± 1	37.0 ± 0.5
5	16	187 ± 2	220 ± 1	38.0 ± 0.5
6	16	187 ± 2	220 ± 1	38.0 ± 0.5
7	16	190 ± 2	220 ± 1	38.0 ± 0.5
8	9	190 ± 2	220 ± 1	37.0 ± 0.5
9	6	190 ± 2	220 ± 1	36.0 ± 0.5
10	4	190 ± 2	220 ± 1	36.0 ± 0.5
11	3	190 ± 2	220 ± 1	36.0 ± 0.5
12	2	190 ± 2	220 ± 1	36.0 ± 0.5
13	0	190 ± 2	220 ± 1	35.0 ± 0.5

APPENDIX B

Effects of annealing on morphology

As noted in Chapter 7, the nanopillar ITO morphology was unaffected by annealing. Some examples are shown below.

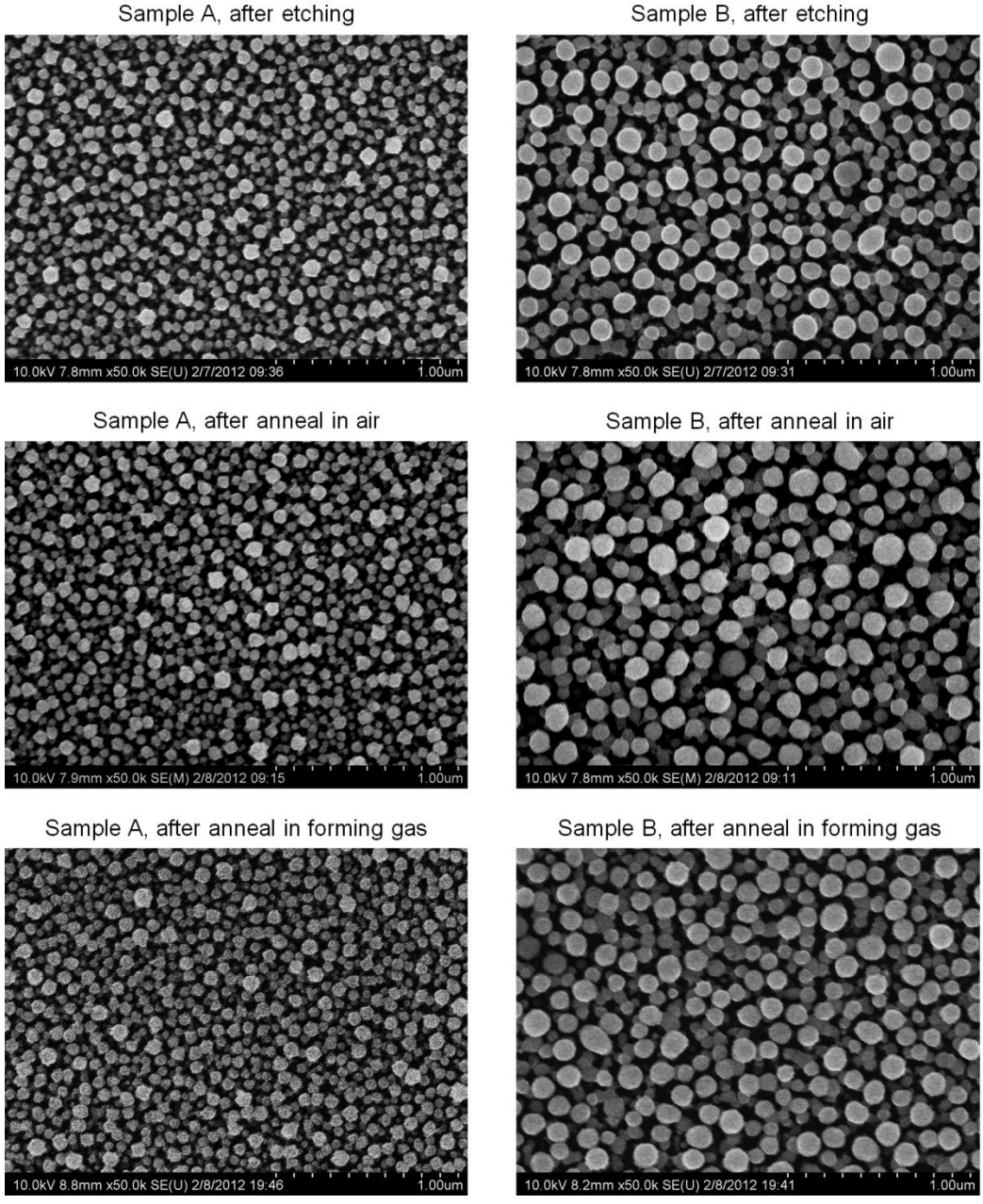

Figure B.1 Annealing does not appear to affect nanopillar ITO morphology.